Dissertation
submitted to the
Combined Faculty of
Natural Sciences and Mathematics
of the
Ruperto-Carola-University of Heidelberg,
Germany
for the degree of
Doctor of Natural Sciences

Put forward by

Master Phys. Paola Pinilla
born in: Bogotá, Colombia

Oral examination: July 5, 2013

Testing models of dust evolution in protoplanetary disks with millimeter observations

Referees:

Prof. Dr. Cornelis P. Dullemond

Prof. Dr. Thomas Henning

A mis padres, con infinito amor e inmensa gratitud

Zusammenfassung

Für die ersten Schritte der Planetenentstehung geht man davon aus, dass interstellar-artige Staubpartikel zu Planetesimalen heran wachsen. In der Entwicklung von Staub und dessen Fähigkeiten zu koagulieren und zu fragmentieren spielen verschiedene physikalischen Prozesse, wie z.B. radialer Drift, Sedimentation und turbulenter Transport, eine wichtige Rolle. Beobachtungen haben gezeigt, dass millimetergrosse Partikel in den äueren Regionen einer protoplanetaren Scheibe überleben können, obwohl dort theoretisch fragmentierende Kollisionen und rapide, nach innen gerichtete Migration von Staubkörpern erwartet werden. Das Hauptziel meiner Arbeit ist der Vergleich von modernsten Evolutionsmodellen für Gas und Staub mit aktuellen Beobachtungen im Millimeterbereich und die Suche nach den günstigsten Szenarien um eine gute Übereinstimmung beider zu erzielen. Es wurden verschiedene Fälle erforscht: typische Scheiben um sonnenartige Sterne, massearme Scheiben wie solche um Braune Zwerge und Scheiben mit Lücken und Löchern, welche als Scheiben in der Übergangsphase bezeichnet werden. Diese Arbeit bietet daher neue theoretische Einschränkungen auf dem Gebiet der Entstehung von Planetesimalen in jungen protoplanetaren Scheiben, welche in direktem Bezug zu den vorhandenen Beobachtungen stehen.

Abstract

The first steps of planet formation imply that dust grows from interstellar-like particles to planetesimals. Different physical processes play an important role in the dust evolution and its ability to coagulate and fragment, such as: radial drift, settling to the midplane and turbulent mixing. Observational evidences have shown that millimeter sized particles survive in the outer regions of protoplanetary disks in spite of the fragmentation destructive collisions and rapid inward migration of dust bodies, which are theoretically expected. The main goal of my thesis is to compare the state-of-the-art of gas and dust evolution models with current millimeter observations and look for the most favorable scenarios to have a good agreement between the two. Different cases have been explored: typical disks around Sun-like stars, low-mass disks as the ones around Brown Dwarfs and disk with inner gaps or holes known as transition disks. This work therefore brings new theoretical constraints to the planetesimal formation in young circumstellar disks, in direct link with the available observations.

Contents

Chapter 1

Introduction

The field of planetary formation is as old as the first time humans asked how our own planet was created. Observations of our own solar system can provide us a lot of information, however this is only one single object, and it is 4.5 billion years old. It is only since 1995 that planets around other solar type stars were discovered. And while the disks out of which these planets are born can nowadays be observed, their tiny size on the sky (< 1 arcsec) make it still today a non-trivial task to study them in detail. From the theoretical side, the situation is equally challenging, since it includes different processes such as radiative transfer, hydrodynamics, coagulation physics and N-body dynamics. Many of these processes are governed by complex and no-linear equations, which implies the need of powerful computers and the development of new numerical methods. This field has had an increasing research since the last two decades, with detailed multidimensional models, but the full problem is not yet numerically tractable.

In the XVIII century for the first time, Emanuel Swedenborg proposed the *nebula hypothesis* to explain the origin of our Solar System. Twenty years later Immanuel Kant refined this idea. They proposed that stars as the Sun are the result of the collapse of a primordial nebula or a giant molecular cloud and as a consequence of this star formation process, a gaseous and dusty *protoplanetary disk* remains around the young star. They also hypothesized that these protoplanetary disks are the birthplaces of planets as the ones in our Solar System. However, it is only late in the XX century, that this conjecture could be confirmed by optical and millimeter images of high angular resolution that demonstrated the existence of these disks around young stars. To understand how planets are formed from these circumstellar disks is certainly a very challenging subject nowadays in Astrophysics, specially with the recent discovery of a wide diversity of planetary systems

that has been detected with the Kepler mission (Batalha et al. 2013). Many questions remain unresolved as for instance: What are the main physical processes that govern the first steps of planet formation? Do we have observational evidences of the growth of dust aggregates to larger objects? Which conditions in disks are needed to form a habitable planet like Earth? Can the variety of exoplanets systems be explained by the diversity of the properties in circumstellar disks? These questions are the main topics of this thesis, in which we investigate the feasibility of dust growth under different physical conditions, and directly linking these models with current observations. The following sections are introduction into various topics of this thesis.

1.1 Formation of a star-planet system

Protoplanetary disks are a direct consequence of the star formation process. Observations of molecular cloud tracers as for example CO, give information about their kinematics and reveal that processes such as rotation, infall and outflow happen in these clouds. The angular momentum of the cores within the molecular clouds results to be much larger than for instance the angular momentum of the Sun, this difference is known as the *angular momentum problem* of star formation.

Dense cores in turbulent molecular clouds collapse to stellar densities as a result of their excess of angular momentum (Shu et al. 1987). Since the resulting stars have much lower angular momentum than the original clouds, the original angular momentum of the molecular cloud can be redistributed, or at least some part of it, to a small amount of gas but allocated at a large distance. This for example occurs in our Solar System, where the Sun contains 99.96% of the mass, but only 0.6% of the total angular momentum of the system is from the Sun. A disk around the recent formed star, with a size between 100 to 1000 AU could partially explain the loss of angular momentum in the star formation process (Terebey et al. 1984). Hence the disk formation around a protostar is a natural consequence of the star collapse process and by the middle of the XX century, implicit observational signs of the presence of circumstellar material were already suggested with e.g. optical emissions line spectra (Herbig 1950).

1.1.1 Evolution of a protostar

The young star objects (YSO) can be classified based on the slope $\alpha_{\rm IR}$ of their infrared spectral energy distribution (SED) (Lada 1987), which can be measured through wide band photometry. Depending on the amount of the

circumstellar material, $\alpha_{\rm IR}$ changes since this material absorbs the light emitted by the central protostar and re-emits it again at longer wavelengths. The current classification represents the evolutionary sequence from the formation of protostars to more evolved pre-Main Sequence (PMS) stars. In the last stage, these stars are surrounded by planetary systems or *debris* disks, which are gas-poor disks mainly made of asteroids which collisions lead to a constant refilling of new-generations of small particles. As is shown in Fig. 1.1, the classification is:

- Class 0: Corresponds to a protostar in the earliest stage of its formation, embedded in its surrounding optically thick envelope, without emission at wavelengths shorter than 10-20 μm. The peak of the SED is therefore in the far-infrared or millimeter wavelengths.
- Class I: When the surrounding envelope of the protostar partially dissipates, the central star and its disk start to be detectable at mid-infrared wavelengths. Hence, the SED shows a rising spectrum in the near-infrared and the peak is in the mid or far-infrared.
- Class II: The envelope of the star has totally dissipated. The star is visible at optical wavelengths. In the infrared, the circumstellar disk is optically thick while at the (sub-)millimeter wavelengths it is optically thin. The SED is therefore the result of the stellar radiation in the optical and the circumstellar emission in the infrared and millimeter wavelengths.
- Class III: In the latest stage, the gaseous disk has been accreted onto the star and the pre-main-sequence star remains with no or very little infrared excess. The star is surrounded by a debris, tenuous and optically thin disk or a planetary system.

1.1.2 Planet formation theories

There are two main theories for planet formation in a disk: the *core accretion scenario* (Safronov & Zvjagina 1969; Goldreich & Ward 1973; Pollack et al. 1996) and the *gravitational instability scenario* (Kuiper 1951; Cameron 1978).

According to the core accretion scenario, terrestrial planets as well as the core of giant planets, are formed by the accretion of planetesimals. When the core grows, its ability to accrete gas from the surrounding disk increases. How planetesimals form from interstellar dust particles is the main topic of Sect. 1.4, which is still an open question behind this theory. Based on this

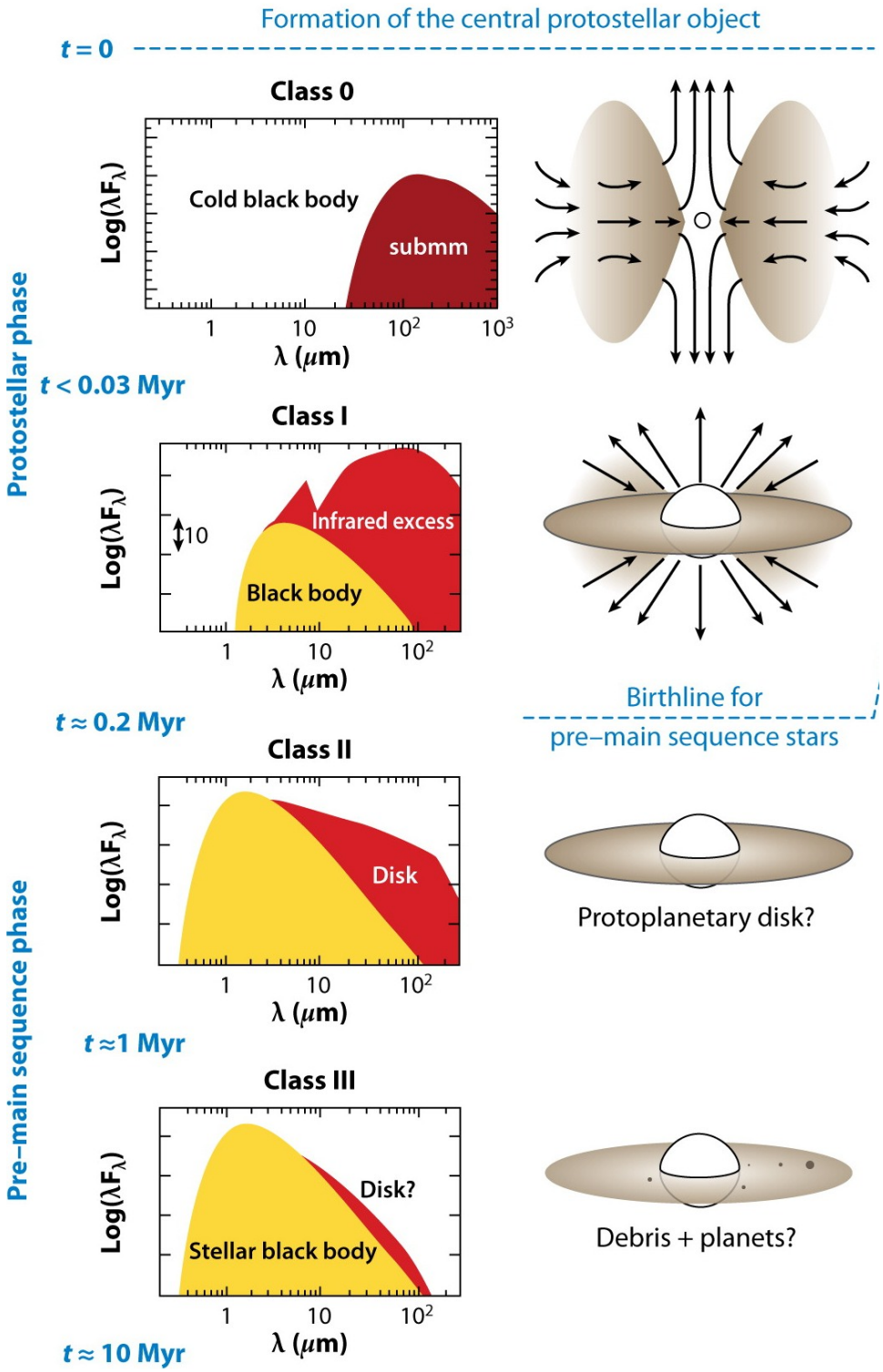

Figure 1.1: Classification of young stellar objects based on the SED shape. Figure adapted from André (2002).

scenario, the whole process (from micron-sized particles to planets) covers more than forty orders of magnitude in mass and the timescales for the gas giant formation are as long as the upper limit of the gas dissipation of the disks (i.e. 1-10 Myr, Haisch et al. 2001). This implies that the gas can be depleted before any planet is formed. In addition, the gravitational torques exerted by the gas disk, when the cores reach a mass of $\sim$ 1 $M_{\oplus}$, lead to radial migration of the core or planet. However, different efforts have focused on planet trapping to avoid this migration (see e.g. Sándor et al. 2011). The mass of the resulting planets from the core accretion scenario can not exceed 6 $M_{\rm Jup}$ (Matsuo et al. 2007). This theory seems to be the most accepted for the formation of our Solar System, since the explanation of the presence of heavy elements in the envelopes of e.g. Jupiter and Saturn can be described by the accretion of planetesimals in the disk (e.g. Young 2003).

On the other hand, the disk can be gravitational unstable when it is massive or/and cold enough. In this case, the disk fragments into a dense protoplanetary clump. These clumps can contract to form giant protoplanets in timescales than are much shorter (several hundred of years) than the dissipation timescales of the disks. The resulting mass of the planets is higher than $\sim$ 2 $M_{\rm Jup}$ (Matsuo et al. 2007; Boley 2009). Gravitational instability is more likely to happen in the outer part of the disk, where the disk is cold enough. If disk fragmentation occurs, the disk should cool quickly enough, however the disk is continuously heated by e.g. turbulence or external radiation. Hence, during the collapse, the internal heating due to gravitational instabilities should happen in longer timescales than the disk cooling. Besides the rapid cooling, this theory requires that the disk must be $\sim$ 15 times more massive than the minimum mass solar nebula or around $\sim$ 10% the mass of the central star, which is higher than it was been observed for most of the protoplanetary disks (Sect. 1.2). Moreover, gas giants formed by gravitational instability are assumed to have a solar abundance ratio, which is inconsistent with observations of giant planets in our own Solar System (Armitage 2011).

Both theories for planet formation face different problems: the timescale difficulties for the core accretion mechanism and the requirement of massive disks for the gravitational instability theory. Observations of high angular resolution of protoplanetary disk that help to determine the dust and gas densities profiles, are an important step for understanding which processes can lead to planet formation.

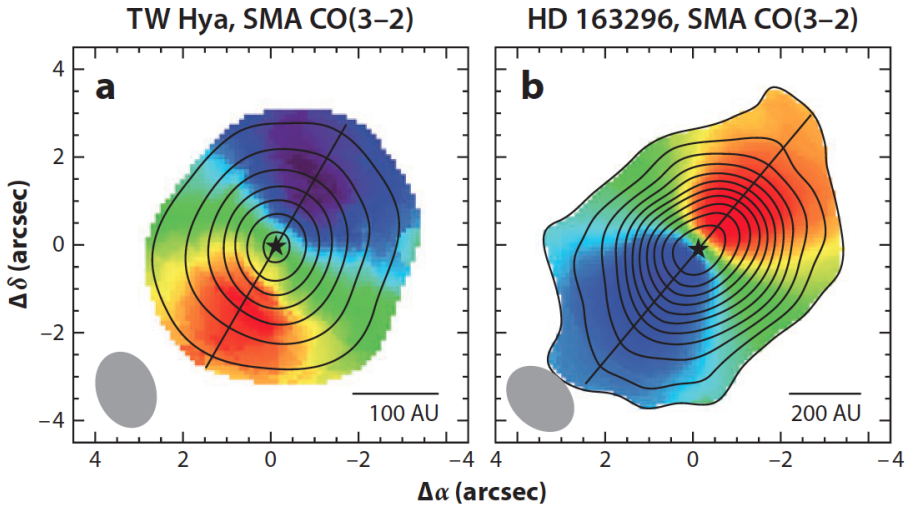

Figure 1.2: CO(3-2) emission from TW Hydra and HD163296 protoplanetary disks, observed by Hughes et al. (2011) with the Submillimeter Array (SMA). The colors show the intensity-weighted velocity or first moment. The contours start at 3σ and increasing every 2σ, with $\sigma = 0.6$ Jy beam^{-1}, and they represent the velocity-integrated intensity or the zeroth moment. Image taken from Williams & Cieza (2011).

1.2 Observations of protoplanetary disks

The opacity, which is the absorption cross section per unit mass of solid material, is dominated by the existing dust in the disk. As a consequence, different dust properties such as its composition, distribution and evolution can be constrained by observations (more details of the extrapolation of dust properties from observations are in Sect. 1.4.2). On the other hand, observing gas lines provide kinematical information of disks with for example high-resolution spectroscopy. Figure 1.2 shows the CO(3-2) emission from TW Hydra and HD163296 protoplanetary disks, observed by Hughes et al. (2011) with the Submillimeter Array (SMA). The contour lines and colors represent the zeroth moment (velocity-integrated intensity) and the first moment (intensity-weighted velocity) respectively, showing the Keplerian rotation of the disk around the central star.

Multi-wavelength observations have also been used to study different properties of the young circumstellar disks. Figure 1.3 reflects the components of a SED that probe different regions of a cicumstellar disk. Optical observations with high angular resolution can probe the geometrical structure of the surface layers, since small particles ($\lesssim$ 10 μm) in these regions

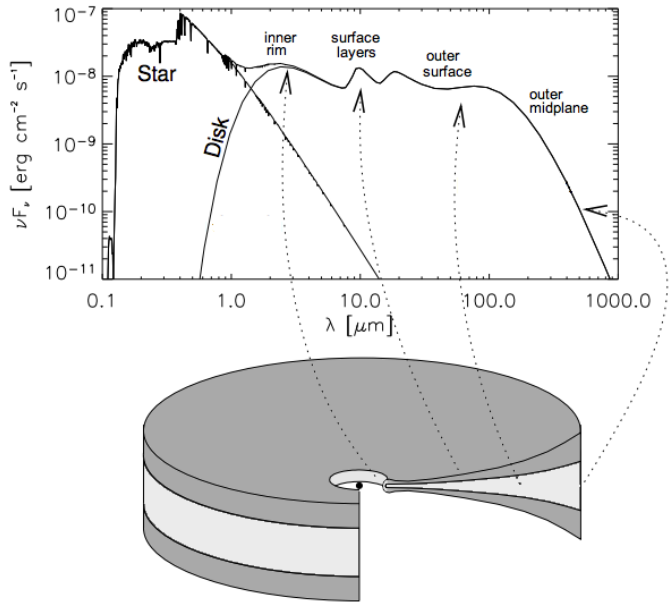

Figure 1.3: Typical SED components of a protoplanetary disk: short wavelength emission comes from inner regions while long wavelength emission probes the outer regions of the disk. Figure adapted from Dullemond et al. (2007).

scatter efficiently the radiation from the star. Such observations recently reveal interesting futures of protoplanetary disks, as for instance in the case of the disk HD135344B. Figure 1.4 shows the observations of the scattered light of this disk in the H-band (1.6 μm) done with the Subaru Telescope (Muto et al. 2012), revealing the existence of a pair of spiral features in the outer disk and suggesting the presence of one or more planets in this disk.

In the infrared, disks are optically thick and the emission at these wavelengths reflects the emitting temperature. Regions below $\lesssim$ 1.0 AU are hot enough to be detectable in the near-infrared. With advanced infrared telescopes such as *Spitzer* and *Herschel*, properties at scales of $\sim$ $0.5 - 20$ AU could be investigated, in particular the surface layers where the temperatures are higher due to the direct exposure to stellar radiation.

In the (sub-)millimeter range, the emission of the disk is optically thin and it essentially comes from the dense regions in the midplane of the outer disk. Most of the disk mass is expected to be in these outer regions. For this reason, high angular resolution observations at these wavelengths can provide information about the radial mass distribution of the disks, which is essential to know for disk evolution models. Nevertheless, the mass of the

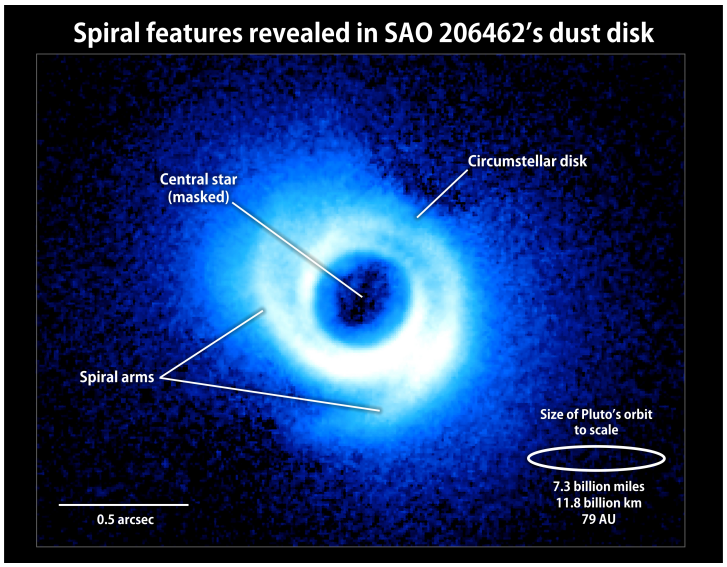

Figure 1.4: Observations of HD135344B with the Subaru Telescope and its HiCIAO instrument on the H-band (1.6 μm). Image credit: http://www.nasa.gov/topics/universe/features/possible-planets.html

disk is somewhat uncertain since it depends on the assumed dust-to-gas ratio and dust size distribution. Observational surveys at millimeter wavelengths (see e.g. Andrews & Williams 2005) show that the median ratio of disk to stellar mass is $\sim 1\%$.

1.2.1 Transition disks

For typical protoplanetary disks the observational interest is mostly focused on YSO of Class II. Early studies of star forming regions, with the Infrared Astronomical Satellite (IRAS), have shown that 60-80% of the SEDs of young stars (lifetime of $\lesssim 1$ Myr) possesses an infrared excess (e.g. Strom et al. 1989), implying that these stars have a surrounding disk. Observations of this infrared excess also give information about the disk evolution. Using *Spitzer* observations of stars in the young Orionis cluster, Hernández et al. (2007) showed the infrared disk emission as a function of their age (Fig. 1.5), revealing that after ~ 10 Myr almost no stars have a infrared excess i.e. the circumstellar disk has dissipated. The typical lifetime of a disk is therefore $\sim 1 - 10$ Myr.

Observations done with IRAS in 1989 by Strom et al. (1989) revealed for the first time a new kind of disks, with little or no excess emission at $\lambda < 10\ \mu m$, but with a significant excess at $\lambda \geq 10\ \mu m$. This feature has

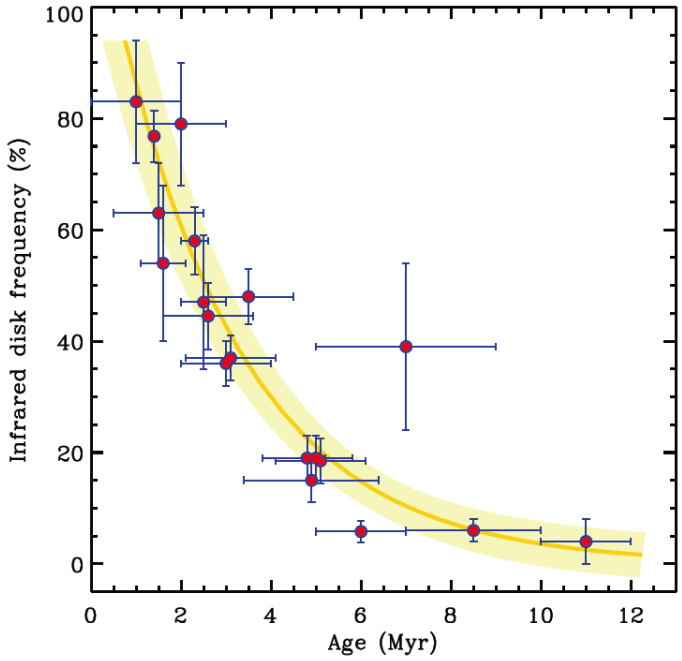

Figure 1.5: Infrared excess of different stars vs. their age. Figure adapted from Hernández et al. (2007).

been interpreted as a optically thick disk with a inner hole, where the dust has been depleted or it has become optically thin. These disks were called *transition disks*, because they may indicate a transition between a gas- and dust-rich disk to a debris disk (gas-poor disk) i.e. from a disk around a YSO of Class II to one around Class III.

Since first described, much emphasis has been placed on understanding the significant clearing in the inner regions of these disks. For instance, the SED modeling of different transition disk shows that the inner holes have different radial extensions ($\sim$ 4-80 AU) (see e.g. Calvet et al. 2005) and the existence of these inner holes has been confirmed by direct imaging at mm-wavelengths (see e.g. Hughes et al. 2009; Brown et al. 2009; Andrews et al. 2011a). Figure 1.6 shows an example of a dust continuum map and the SED fitting of a transition disk, in this case a disk knows as LkHα 330. The dotted blue line in the SED of the right panel of Fig. 1.6 is the equivalent model without considering the existence of the inner hole (Brown et al. 2009).

Some of these disks have an active accretion (e.g Espaillat et al. 2007), which indicates that substantial amounts of gas is still sheltered within the dust holes. The variety of the physical properties of transition disk has suggested that different mechanisms may explain their observed features,

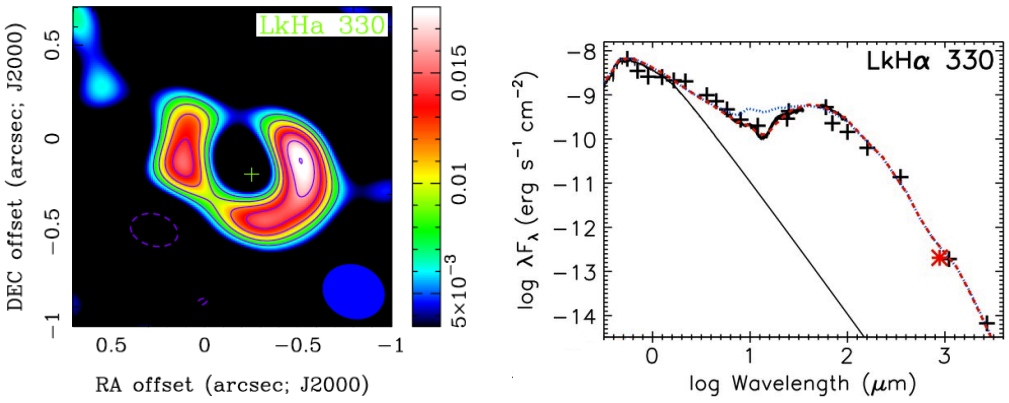

Figure 1.6: *Left:* Dust continuum image of the transition disk LkHα 330 obtained with SMA at a frequency of 345 GHz. *Right:* The corresponding SED fitting of LkHα 330, the dotted blue line is the equivalent model without hole. Images taken from Brown et al. (2009)

such as: photoevaporation (e.g. Owen et al. 2011), planet formation (e.g. Papaloizou & Lin 1984), grain growth (e.g. Tanaka et al. 2005) or a mix between some of these phenomena, as for instance photoevaporation and planet formation (Rosotti et al. 2013). In any case, these disks are excellent candidates to study and test planet formation theories.

1.3 Basic properties of protoplanetary disks

To understand how planets can form from protoplanetary disks, it is important to study different properties of these objects as for example: geometry, temperature, gas accretion, etc. In this section, the basic physical properties of disks are summarized.

1.3.1 Vertical structure

Assuming that the gravitational potential is dominated by the star, i.e. $M_{\rm disk} \ll M_\star$, the vertical gas structure depends on the force balance:

$$g_z = g \sin\theta = \frac{GM_\star}{r^2+z^2}\frac{z}{(r^2+z^2)^{\frac{1}{2}}} = -\frac{1}{\rho}\frac{dP}{dz} \tag{1.1}$$

where r is the cylindrical distance from the star, z the corresponding vertical position, θ the angle formed between r and z, and P the gas pressure. Assuming that the gas is vertically isothermal, with the pressure defined as

$P \equiv \rho\, c_s^2$, with ρ being the total gas surface density and c_s the sound speed defined as $c_s^2 \equiv k_B\, T/\mu\, m_p$ (with k_B being the Boltzmann constant, m_p the proton mass, μ the mean molecular mass and T the gas temperature) and considering that $z \ll r$ i.e. a thin disk, the solution of Eq. 1.1 is a gaussian function,

$$\rho = \rho_0 \exp\left[\frac{-z^2}{2h^2}\right], \tag{1.2}$$

where ρ_0 is the midplane density and h the vertical disk scale-height, defined as $h \equiv c_s/\Omega$, with Ω as the Keplerian frequency ($\Omega \equiv (GM_\star/r^3)^{1/2}$). This indicates that $\sim$ 68% of the mass of the disk lies within $\pm h$ of the midplane. If the radial variation of the sound speed is parameterized by $c_s \propto r^{-\beta/2}$, the aspect radio varies as $h/r = r^{-(\beta+1)/2}$. This implies that the geometry of the disk basically depends on the temperature profile of the disk. A *flared disk* means that h/r increases with radius. SED fitting (as it is sketched in Fig. 1.3) at infrared wavelengths have suggested that disks around Sun-like stars have a flaring geometry (see e.g. D'Alessio et al. 2001). Additionally, direct imaging with e.g. the Hubble Space Telescope reveals that disks are flared as it is the case of the disk HH 30 (Burrows et al. 1996).

It was already 25 years ago, that infrared (IR) observations of Class II objects revealed that the IR-emission is underestimated if the geometry of the disk is considered to be flat (see Kenyon & Hartmann 1987). Contrary, if disks are assumed to be flared, at large radii the disk thickness increases and it can therefore absorb and re-emit a larger amount of the stellar radiation, leading to a larger IR excess.

1.3.2 Temperature profile

Assuming a vertically isothermal disk, the central star as a point source of radiation i.e. $R_\star \ll r$, $\alpha_{\rm inc}$ as the angle between the incident radiation and the local disk surface and that all the stellar surface is visible from the surface of the disk, Kenyon & Hartmann (1987) approximated the radial temperature profile for a flared disk by:

$$T(r) = T_\star \left(\frac{R_\star}{r}\right)^{1/2} \alpha_{\rm inc}^{1/4}, \tag{1.3}$$

implying that $h/r \propto r^{5/4}$. Considering a finite size for the stellar radius, the angle of the incident radiation and the disk is defined as $\alpha_{\rm inc} \equiv 0.4\, R_\star/r + rd/dr(h/r)$ (Chiang & Goldreich 1997). This calculation can vary if the

effect of dust sublimation, accretion heating, realistic opacities and vertical structure are considered at each point of the disk (Dullemond et al. 2001).

1.3.3 Orbital velocity of the gas

Assuming that the star dominates the gravitational potential, the orbital velocity of the disk gas can be obtained by the radial component of the equation of motion,

$$\frac{v_{\phi,\mathrm{gas}}^2}{r} = \frac{GM_\star}{r^2} + \frac{1}{\rho}\frac{dP}{dr} \tag{1.4}$$

or,

$$v_{\phi,\mathrm{gas}} = v_k\left(1-\eta\right), \tag{1.5}$$

where v_k is the Keplerian speed and

$$\eta = -\frac{1}{2\rho r\Omega^2}\frac{dP(r)}{dr}. \tag{1.6}$$

This implies that the gas orbital velocity is typically sub-Keplerian (Eq. 1.5 and 1.6), if for instance the disk is assumed to be vertically isothermal with gas density and temperature profiles monotonically decreasing with the radial distance. However, the difference between the gas and Keplerian velocities are quite small, and the pressure can be neglected when studying the gas radial structure. Nevertheless, this sub-Keplerian velocity of the gas has a significant role for the dust motion as is discussed in Sect. 1.4.

1.3.4 Disk evolution

Protoplanetary disks are dynamical objects in which it was thought that internal friction was responsible of the angular momentum transportation throughout the disk and therefore of the continued accretion onto the star. In a geometrically thin disk $h(r) \ll r$, the continuity equation for the surface density, $\Sigma(r,t) = \int_{-\infty}^{\infty}\rho(r,z,t)dz$, is given by,

$$r\frac{\partial\Sigma}{\partial t} + \frac{\partial}{\partial r}(r\Sigma v_r) = 0. \tag{1.7}$$

Considering a viscous torque $G(r)$, the angular momentum conservation is written as

$$r\frac{\partial}{\partial t}(r^2\Omega\Sigma) + \frac{\partial}{\partial r}(r^2\Omega r\Sigma v_r) = \frac{1}{2\pi}\frac{\partial G}{\partial r}. \tag{1.8}$$

where Ω is the Keplerian frequency. The viscous torque is calculated as the product of the circumference, the radial distance and the viscous force per unit length (Pringle 1981), or

$$G(r) = 2\pi r \cdot r \cdot \nu\Sigma r \frac{d\Omega}{dr}. \tag{1.9}$$

Using Eqs. 1.7, 1.8 and 1.9, the evolution equation for the gas surface density is given by

$$\frac{\partial\Sigma}{\partial t} = \frac{3}{r}\frac{\partial}{\partial r}\left[r^{1/2}\frac{\partial}{\partial r}(\nu\Sigma r^{1/2})\right] \tag{1.10}$$

where ν is the kinematic viscosity. The gas radial velocity can be written as

$$v_r = -\frac{3}{\Sigma\sqrt{r}}\frac{\partial}{\partial r}(\Sigma\nu\sqrt{r}). \tag{1.11}$$

Equation 1.10 can be recognized as a diffusion equation, with diffusion timescales given by $\tau_\nu = r^2/\nu$. If internal molecular forces are the only responsible of viscosity inside the disk, the viscous timescale at $\sim$ AU distances would be longer than the age of the Universe (see e.g. Armitage 2011). Nowadays, it is believed that disks transport angular momentum by turbulence, but the source of this turbulence is still debated. Shakura & Sunyaev (1973) proposed a turbulent viscosity provided by eddies with a maximum size of a one scale height h with a velocity as high as the sound speed c_s. Their parametrization is given by,

$$\nu = \alpha h c_s, \tag{1.12}$$

where α is a dimensionless constant that can be estimated by the observed disk lifetimes, which are between 1-10 Myr (Fig. 1.5), leading to α-values between 10^{-4} to 10^{-2}. Theoretical models that assume that magnetorotational instability (MRI) as the main source of turbulence predict values for α of 10^{-3} to 10^{-2} (Johansen & Klahr 2005; Dzyurkevich et al. 2010).

1.4 The stages of planet formation

The question of how planets are formed from interstellar dust in protoplanetary disk is still a debated topic with many unresolved problems. Base on the core accretion scenario, this process can be divided in three different stages:

1. **Agglomeration of dust particles:** The typical initial value of the dust-to gas ratio in protoplanetary disk is assumed to be as the canonical value for the interstellar medium (ISM), i.e. $\sim$ 1%, and therefore

dust contributes only a small fraction of the total mass of the disk. However, from the agglomeration of this interstellar dust, planetesimals are expected to form. Since gas is the dominant ingredient of protoplanetary disks, the dust dynamics is controlled by its interaction with the gas and dust grains are strongly influenced by the aerodynamical drag that they feel within the disk. This section focuses on this growth process from (sub)-micron sized particles to planetesimals, which basically happens due to pairwise collisions, neglecting the possibility of accumulations of dust in a specific region that can lead to a dust-to-gas ratio close to unity, in which case feedback from the dust to the gas must be considered.

2. **Planetesimals:** When particles form kilometer-sized objects or planetesimals, they are large enough to gravitationally interact with each other and gravity dominates the dynamics. The growth from planetesimals to larger objects is possible due to the fact that when they collide the gravity of the initial objects is enough to agglomerate again the fragments into a single object.

3. **Terrestrial planets and core of giant planets:** When planetesimals are large enough, they start to interact gravitationally with the gas of the disk. As a consequence, two different phenomena can happen: these new cores capture material from the disk via *gas accretion* or angular momentum exchange can occur leading to *migration*.

1.4.1 From dust aggregates to planetesimals

The grain growth, from ISM-like dust to planetesimals, initially happens because of the sticking collisions due to molecular interactions or van der Waals forces between particles. The relative velocities between dust grains are mainly due to *Brownian motion* and *settling* to the midplane, and growth is extremely efficient in these first stages of dust evolution. However, when dust grows to certain sizes *radial drift* and *turbulent* motion may increase to the point where the relative velocities lead to fragmentation collisions. Figure 1.7 illustrates the sources of relative velocities between dust particles.

As it was explained, these first stages of planetesimal formation are governed by the drag with the gas. This aerodynamical drag depends on the cross-sectional area of the solid grain. For small particles, the *Epstein regime* is considered, i.e. the size of the particles a is assumed to be lower than the mean free path of gas molecules inside the disk, i.e. $a \lesssim \lambda_{\rm mfp}$. In general, the drag force for a particle of mass m, which opposites the dust movement, can be written as,

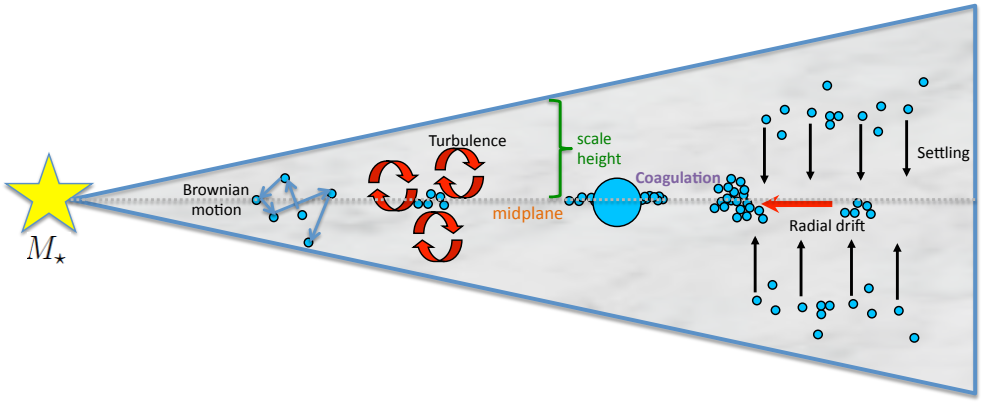

Figure 1.7: Pictographic representation of the possible relative velocities between dust particles and their coagulation within a protoplanetary disk.

$$\vec{F}_{\rm drag} = -\frac{m}{\tau_s}\vec{v}, \tag{1.13}$$

where τ_s is the stopping time of the particle within the gaseous disk. In the Epstein regime, τ_s is given by

$$\tau_s = \frac{\rho_s}{\rho}\frac{a}{v_{\rm TH}}, \tag{1.14}$$

with ρ_s as the material density and $v_{\rm TH}$ the mean thermal velocity of the gas molecules defined as $v_{\rm TH} \equiv \sqrt{8/\pi}c_s$. Therefore the drag force is

$$\vec{F}_{\rm drag} = -\frac{4\pi}{3}\rho a^2 v_{\rm TH}\vec{v}. \tag{1.15}$$

Brownian motion The (sub)-micron dust particles, which are well coupled to the gas, have random velocities due to the thermal gas motion. The Brownian relative velocity between two particles of mass m_1 and m_2 is given by

$$\Delta v = \sqrt{\frac{8\ k_B\ T\ (m_1 + m_2)}{\pi\ m_1\ m_2}}. \tag{1.16}$$

Considering Brownian motion, particles are expected to grow from ISM-like dust to millimeter or centimeter sizes in timescales $\lesssim 10^4$yr.

Settling Neglecting the effects of turbulence, the settling velocity can be calculated assuming the forces that vertically act on the particles, which are the vertical component of gravity $F_{\rm grav} = -m\,\Omega^2\,z$ and the gas drag $F_{\rm drag}$ (Eq 1.15). In this case the settling speed is

$$v_{\rm settle} = \frac{\rho_s}{\rho}\frac{a}{v_{\rm TH}}\Omega^2 z. \tag{1.17}$$

At few AU, the typical timescales for micron-sized particles to settle to the midplane are $\sim 10^5$ yr. Larger particles (mm or cm-sized) settle faster with timescales of around 100 yr. Studies of dust settling including turbulence have been proposed (see e.g. Dullemond & Dominik 2004), concluding that turbulence opposes the sedimentation of micron-sized dust particles which would remain suspended in the layers of the disk, while millimeter and centimeter-sized particles are large enough to be anyway settled to the midplane, even when the disk is highly turbulent.

Radial drift The effect of gas drag strongly affects the radial and azimuthal motions of the particles. Mainly, three forces act on a dust grain,

$$\sum \vec{F} = \vec{F}_{\rm grav} + \vec{F}_{\rm centrifugal} + \vec{F}_{\rm drag}$$

where the drag force opposes the motion of dust grains and the stopping time τ_s is defined as Eq. 1.14. The equations of motion in the radial and azimuthal direction are respectively,

$$\frac{\partial v_{r,\rm dust}}{\partial t} = \frac{v^2_{\phi,\rm dust}}{r} - \Omega r - \frac{1}{\tau_s}(v_{r,\rm dust} - v_{r,\rm gas}) \tag{1.18}$$

$$\frac{\partial (r v_{\phi,\rm dust})}{\partial t} = \frac{r}{\tau_s}(v_{\phi,\rm dust} - v_{\phi,\rm gas}). \tag{1.19}$$

Solving the last two equations simultaneously and taking into account azimuthal gas velocity (Eq. 1.5), in terms of a dimensionless stopping time, which is known as the *Stokes number* and is defined as $\mathrm{St} = \Omega\tau_s$, the total radial dust velocity is

$$v_{\rm r,dust} = \frac{v_{\rm r,gas}}{1+\mathrm{St}^2} + \frac{1}{\mathrm{St}^{-1}+\mathrm{St}}\frac{1}{\rho\Omega}\frac{\partial P}{\partial r}. \tag{1.20}$$

The dependence of the dust radial velocity with the Stokes number, at 1 AU distance from the central star, is shown in Fig. 1.8. For particles with $\mathrm{St} \ll 1$ the first term of Eq. 1.20 dominates, which corresponds to small

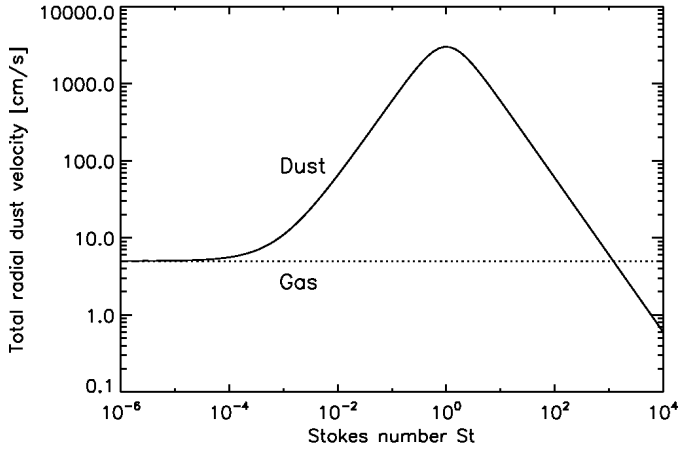

Figure 1.8: The total radial dust velocity of dust at 1 AU distance from the central star vs the Stokes number. Figure taken from Brauer et al. (2008).

particles that are well coupled to the gas, as a consequence they move along with it and their velocities are equal to the radial gas velocities. When the Stokes number increases, the second term of Eq. 1.20 becomes relevant and for St=1, the dust radial velocity reaches its maximum value of $\sim$ 3000 cm/s. Hence, it is expected that high-velocity collisions between particles with different drift velocities cause fragmentation. In addition, with these high radial velocities, dust with St $\approx$ 1 would drift towards the star in timescales of $\sim$ 100 yr, and as a result the dust would be lost in timescales that are much shorter than the times that dust needs to grow to planetesimal sizes. Objects with St=1 at 1 AU distance corresponds to sizes of $\sim$ 1 m and this is the reason why the problem of excessive inward drift and potential destructive collisions is known as *the meter-size barrier* introduced for the first time by Weidenschilling (1977).

Turbulent motion The presence of turbulent eddies in the disk may induce also a random motion of the dust particles. Different authors, as for example Voelk et al. (1980); Mizuno et al. (1988); Markiewicz et al. (1991) have numerically studied the turbulent motion of particles in protoplanetary disks. In particular Ormel & Cuzzi (2007) studied the relative velocities due to turbulences for different size particle regimes. In the Epstein regime, the maximum turbulent relative velocity given by Ormel & Cuzzi (2007) is

$$\Delta v^2_{\rm turb,max} \simeq \frac{3\ \alpha}{\rm St + St^{-1}} c_s^2, \tag{1.21}$$

where α is the viscosity parameter by Shakura & Sunyaev (1973) (Eq 1.12).

For St $\sim$ 1 and high viscosity e.g. $\alpha \sim 10^{-2}$, these turbulent velocities can reach values as high as the radial drift velocities, leading to destructive collisions between dust grains.

1.4.2 Observational evidence of dust growth in protoplanetary disks

Since the infrared emission of a protoplanetary disk comes from the optically thick region, this is sensitive to the temperature and it can be determined by the infrared SED fitting as it was explained in Sect. 1.3.2. At longer (sub-millimeter) wavelengths, the total flux at a given frequency F_ν from the optically thin region is sensitive to the dust mass in the continuum and it is given by

$$F_\nu = \frac{M_{\rm dust}}{d^2}\kappa_\nu B_\nu(T(r)) \tag{1.22}$$

where d is the distance to the source, κ_ν is the dust opacity at a given frequency and $B_\nu(T)$ is the Planck function for a given temperature radial profile $T(r)$,

$$B_\nu(T) = \frac{2h\nu^3}{c^2}\frac{1}{\exp\left(\frac{h\nu}{k_B T}\right) - 1}, \tag{1.23}$$

using the Rayleigh-Jeans approximation for long wavelengths, B_ν is

$$B_\nu(T(r)) = \frac{2\nu^2 k_B T(r)}{c^2}. \tag{1.24}$$

On the other hand, if the dust opacity is approximated as a power law function of the frequency ν, i.e. $\kappa_\nu \propto \nu^\beta$, then $F_\nu \propto \nu^{\beta+2} = \nu^{\alpha_{\rm mm}}$, where $\alpha_{\rm mm}$ is known as the spectral index ($\alpha_{\rm mm} \approx \beta+2$). The dust opacity is calculated by convolving the absorption cross section coefficient of a single grain of size a (with a volume density of ρ_s) at a given frequency ν ($C_{\rm abs}(a,\nu)$) with the grain size distribution $n(a)$, i.e.

$$\kappa(\nu) = \frac{\int (dn/da) C_{\rm abs}(a,\nu) da}{\int (dn/da)(\frac{4\pi}{3}\rho_s a^3) da}. \tag{1.25}$$

The first large survey of millimeter observations of protoplanetary disks revealed that $\beta \approx 1$ for Taurus-Auriga (Beckwith & Sargent 1991) and Ophiuchus (André & Montmerle 1994) regions, while interstellar clouds have higher values $\beta \approx 1.7$ (e.g. Finkbeiner et al. 1999). The low β values for protoplanetary disks was interpreted as dust growth within the disk (Draine

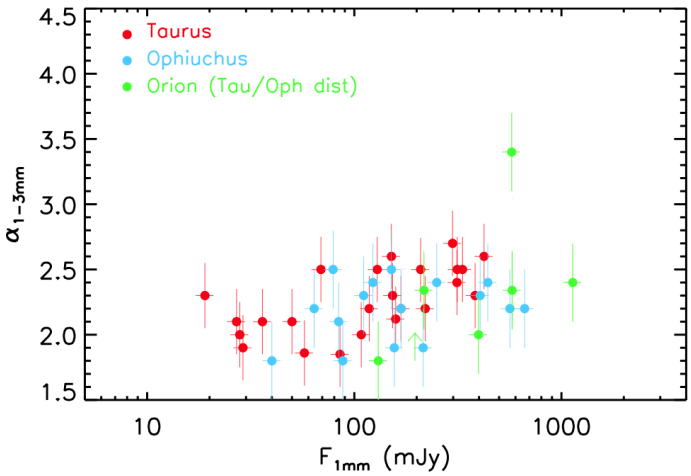

Figure 1.9: Observed fluxes and the spectral indices at millimeter wavelengths of three star forming regions: Taurus, Ophiuchus and Orion Nebula Cluster. Figure adapted from Ricci et al. (2011).

2006). Nevertheless, very small optical thick disks can also lead to low values of the spectral index and for this reason high-angular resolution observations which determine the actual sizes of the disks are needed to correctly interpret the SED at millimeter wavelengths (Testi et al. 2001). Other phenomena that can affect the value of the opacity index is for instance the chemical composition of the dust and its geometry (Draine 2006).

Recent millimeter observations done e.g by Ricci et al. (2010a,b, 2011) for Taurus, Ophiuchus and Orion star forming regions and by Ubach et al. (2012) for Chamaeleon and Lupus regions, have confirmed the low values of the spectral index. Figure 1.9 shows the observed fluxes and the spectral indices (calculated between 1-3mm) of three forming regions. The spectral index $\alpha_{1-3\mathrm{mm}}$ has is average values $\alpha_{1-3\mathrm{mm}} \lesssim 3$, indicating that dust grains have reached millimeter sizes in the colder regions of disks.

1.5 Outline of this thesis

One of the most critical stages in the first steps of planet formations is the *meter-size barrier* explained in Sect. 1.4. In the outer regions of protoplanetary disks, millimeter-sized grains experience the effect of rapid inward drift and destructive collisions that an object of $\sim$ 1 m size typically feels at $\sim$ 1 AU distance from the central star. However, it was shown in Sect. 1.4.2

that pebbles [1] are detectable with millimeter observations. The paradigm of overcoming the meter-size barrier and explaining observations has been an unresolved question for the last decades. The main goal of this thesis is to link the theoretical models of dust evolution in different cases (wherein the physical processes differ) with current millimeter observations. This is thesis is organized as:

Chapter 2 investigates the presence of mm-grains in the outer regions of T-Tauri (TTS) disks, in spite of the high inward migration and fragmentation. To reduce the radial migration, pressure bumps in the gas disk are proposed, which can result from magneto-rotational instability (MRI). It is demonstrated that the amplitude of pressure bumps of global MRI simulations is sufficient to retain millimeter-sized grains, thereby being a possible explanation to the observed spectral index of TTS disks (Fig. 1.9). We present simulated images using different antenna configurations of ALMA at different frequencies, to show that the ring structures will be detectable at the distances of either the Taurus Auriga or Ophiucus star-forming regions.

Chapter 3 focuses on explaining recent observations by CARMA and ALMA, which detected millimeter grains in the cold regions of disks around Brown Dwarfs. Due to the different stellar properties, some phenomena as settling and radial drift occur differently for particles in disks around such low-mass objects compared to TTS disks. We use coagulation, fragmentation and disk-structure models to simulate the evolution of dust, with zero and non-zero radial drift. In the latter, we consider strong inhomogeneities in the gas surface density profile that mimic long-lived pressure bumps in the disk. It is shown that the presence of these millimeter-grains can be explained considering extreme conditions in the disk such as strong pressure inhomogeneities.

Chapter 4 explores the exciting scenario of disks with inner gaps or holes, which are known as transition disks. In this case, a massive planet is considered to open a gap in the disk and therefore a reduction in the gas surface density leads to a huge pressure trap. It is shown that millimeter-sized grains form and accumulate at the pressure maximum and produce the observed ring shaped at sub-millimeter emission of some transition disks. Additionally, when the planet is very massive, it is expected a large spatial separation between the inner gas edge of the outer disk and the peak of the millimeter

[1] The word *pebble* refers to millimeter or centimeter grain size based on the Krumbein Phi Scale of United States, which is often used in different areas as mineralogy and geology.

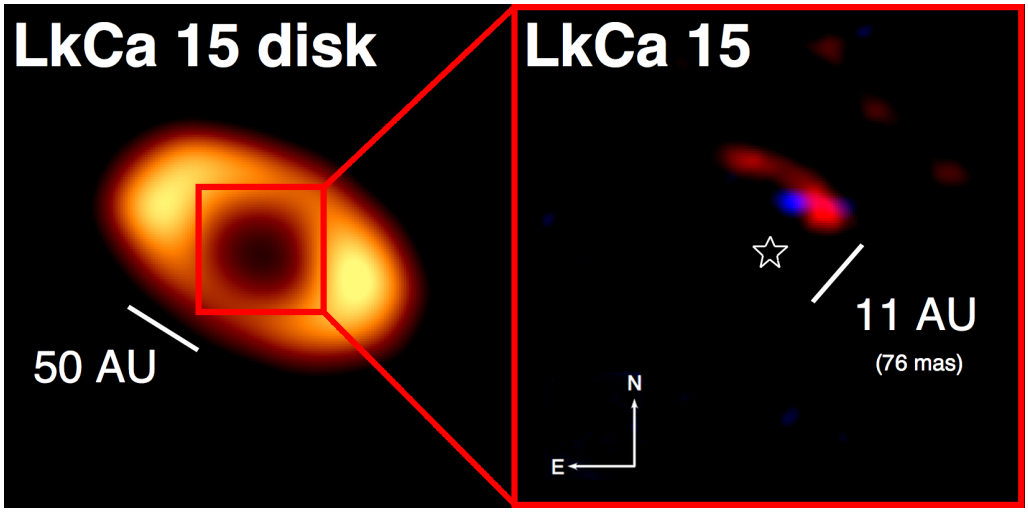

Figure 1.10: *Left panel:* Millimeter observations of the transition disk LkCa 15 at 850 μm made by Andrews et al. (2011a) and *right panel* the reconstructed image from Keck aperture masking observations at different bands: blue - *band K* - or $\lambda = 2.1$ μm, interpreted by the emission of a massive companion or planet and red - *band L* - or $\lambda = 3.7$ μm, for the corresponding circumplanetary disk. Image taken from Kraus & Ireland (2011).

emission, in contrast to previous assumptions. Smaller grains get closer to the gap and we predict how the surface brightness varies at different wavelengths. We apply these fundings to the transition disk LkCa 15, for which recent observations claim the detection of massive companion inside a gap (see Fig. 1.10 from Kraus & Ireland 2011). Computing the dust distribution for a disk interacting with a massive planet, we obtain similar features as the ones that have been observed for LkCa 15.

Chapter 5 studies the efficiency of dust growth in azimuthal traps. Recent observations of transition disks reveal that the millimeter emission can clearly have non-axisymmetric structures as is recently shown by e.g. Casassus et al. (2013) (Fig. 1.11, for the most recent ALMA observations of the transition disk HD142527). In this chapter, the azimuthal structure was calculated analytically for a steady-state between mixing and azimuthal drift. It is proved that smooth and long-lived azimuthal density gradients can lead to strong dust accumulations. With the current ALMA capabilities, it is possible to detect such azimuthal traps by measuring azimuthal variations of the spectral index.

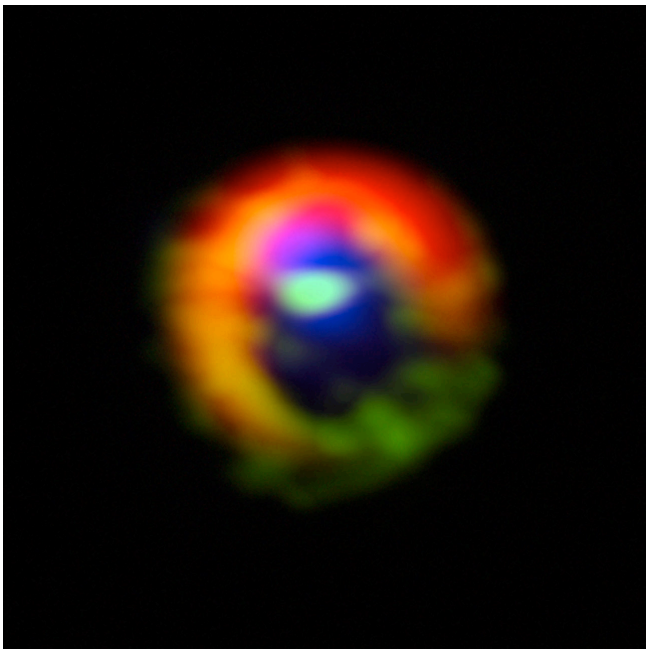

Figure 1.11: ALMA observations of the transition disk HD142527 from Casassus et al. (2013). The red color shows the continuum emission at 870 μm. The green color shows the HCO^+ (4-3) line, revealing streams flowing across the gap. The blue color is CO (3-2) emission, which corresponds to the diffuse gas in the gap. Image credit: http://www.eso.org/public/images/eso1301b/.

Chapter 6 describes two different kinds of asymmetries that result from the interaction of a disk with a massive planet: an eccentric disk and a giant vortex. In this chapter, it is demonstrated that in both cases the azimuthal dust distributions are completely different because in contrast with to eccentric disks, vortices are indeed pressure traps which leads to strong concentrations of dust particles in the azimuthal direction.

Chapter 7 reports the first 3-millimeter photometry observations of four transition disks: LkHα 330, UX Tau A, LRLL 31, LRLL 67 carried with Plateau de Bure Interferometer. Considering previous observations, we do SED modeling to constrain different disk parameters. In addition, we use the millimeter observations of these four disks at 345GHz with the Submillimeter Array, to calculate the spectral indexes for these disks. We show that for three of the mentioned sources, the spectral index reveals that millimeter-grains may exist in those disks, indicating that a mechanism such as a planet

interacting and carving a gap in the disk may allow particles to be retained and grow to pebbles despite the excessive inward radial drift that is expected.

Chapter 8 summarizes and concludes the work of this thesis. In addition, future prospects are discussed.

Appendix A is a synopsis of additional contributions done in the planet formation field.

Chapter 2

Trapping dust particles in the outer regions of protoplanetary disks

Based on the paper by ***Pinilla P.****, Birnstiel, T., Ricci, L., Dullemond, C. P., Uribe, A. L., Testi, L., Natta, A., A&A, 538, A114*

The study of planet formation is an important field in astronomy with a large amount of research having been completed since the middle of the twentieth century, although countless unanswered questions remain. One of these questions is what is the cause of the observed grain growth to mm sized particles in the outer disk regions (Beckwith & Sargent (1991); Wilner et al. (2000, 2005); Testi et al. (2001, 2003); Andrews & Williams (2005); Rodmann et al. (2006); Natta et al. (2007); Isella et al. (2009); Lommen et al. (2009); Ricci et al. (2010a, 2011); Guilloteau et al. (2011)), which suggests that there is a mechanism operating to prevent the rapid inward drift (Klahr & Henning (1997), Brauer et al. (2007), Johansen et al. (2007)). Different efforts aim to explain theoretically the growth from small dust particles to planetesimals, which have led to the development of different numerical models, e.g. Nakagawa et al. (1981), Dullemond & Dominik (2005), Brauer et al. (2008), Zsom & Dullemond (2008), Okuzumi (2009), Birnstiel et al. (2010a). Since circumstellar disks exhibit a wide range of temperatures, they radiate from micron wavelengths to millimeter wavelengths, which is why they can be observed with infrared and radio telescopes. With the construction of different kinds of these telescopes, e.g. Spitzer, Herschel, SMA, EVLA, or ALMA, astronomers can observe in more detail the material inside accretion disks around young stars. The parallel development of theory and obser-

vations have allowed astrophysicists to study the different stages of planet formation, making this topic one of the most active fields in astronomy today.

In the first stage of planet formation, the growth from sub-micron sized particles to larger objects is a complex process that contains many physical challenges. In the case of a smooth disk with a radial gas pressure profile that monotonically decreases with radius, the dust particles drift inwards because the gas moves with a sub-Keplerian velocity due to the gas pressure gradient. Before a large object can be formed, the radial drift causes dust pebbles to move towards the star. Moreover, the large relative velocities produced by turbulence and radial drift cause the solid particles to reach velocities that lead to fragmentation collisions that prevent dust particles from forming larger bodies (Weidenschilling 1977; Brauer et al. 2008; Birnstiel et al. 2010b). The combination of these two problems is called a "meter-size barrier" because on timescales as short as 100 years, a one-meter-sized object at 1 AU moves towards the star owing to the radial drift, preventing any larger object from forming.

The observations in the inner regions of the disk, where planets such as Earth should form, are very difficult because these regions are so small on the sky that few telescopes can spatially resolve them. In addition, these regions are optically thick. However, a meter-size barrier in the inner few AU is equivalent to a "millimeter-size barrier" in the outer regions of the disk. These outer regions ($\gtrsim$ 50 AU) are much easier to spatially resolve and are optically thin. Moreover, one can use millimeter observations, which probe precisely the grain size range of the millimeter-size. Therefore, the study of dust growth in the outer disk regions may teach us something about the formation of planets in the inner disk regions.

Observations of protoplanetary disks at sub-millimeter and mm wavelengths show that the disks remain dust-rich over several million years with large particles in the outer regions (Natta et al. 2007; Ricci et al. 2010a). However, it remains unclear how to prevent the inward drift and how to explain theoretically that mm-sized particles are observed in the outer regions of the disk. Different mechanisms of planetesimal formation have been proposed to resist the rapid inward drift, such as: gravitational instabilities (Youdin & Shu 2002), the presence of zonal flows(Johansen et al. 2009, 2011; Uribe et al. 2011), or dead zones of viscously accumulated gas that form vortices (Varnière & Tagger 2006). With the model presented here, we wish to simulate mechanisms that allow long-lived pressure inhomogeneities to develop in protoplanetary disks, by artificially adding pressure bumps to a smooth density profile.

To confront the millimeter-size barrier, it is necessary to stop the radial drift by considering a radial gas pressure profile that does not monotonically

decrease with radius. We instead take a pressure profile with local maxima adding a sinusoidal perturbation of the density profile. These perturbations directly influence the pressure, following a simple equation of state for the pressure in the disk. Depending on the size of the particle, the dust grains are perfectly trapped in the pressure peaks because a positive pressure gradient can cause the dust particles to move outwards. On the other hand, turbulence can mix part of the dust particles out of the bumps, so that overall there may still be some net radial inward drift. More importantly, dust fragmentation may convert part of the large particles into micron-size dust particles, which are less easily trapped and thus drift more readily inward.

Birnstiel et al. (2010b) compared the observed fluxes and mm spectral indices of the Taurus (Ricci et al. 2010a) and Ophiucus (Ricci et al. 2010b) star-forming regions with predicted fluxes and spectral indices at mm wavelengths. They neglected the radial drift,assuming that the dust particles to remained within the outer disk regions. They attempted to keep the spectral index at low values, which implied that the dust particles had millimeter sizes (Beckwith & Sargent 1991). However, they over predicted the fluxes. As an extension of their work, we model here the combination of three processes: the radial drift, the radial turbulent mixing, and the dust coagulation / fragmentation cycle in a bumpy surface density profile. Our principal aim is to find out how the presence of pressure bumps can help us to explain the retainment of dust pebbles in the outer regions of protoplanetary disks, while still allowing for moderate drift and achieving a closer match with the observed fluxes and mm spectral indices. In addition, we show simulated images using different antenna configurations of the complete range of operations of ALMA, to study whether it is possible to detect these inhomogeneities with future ALMA observations.

This chapter is ordered as follows Sect. 2.1 describes the coagulation/ fragmentation model and the sinusoidal perturbation that we apply to the initial conditions of the gas surface density. Section 2.2 describes the results of these simulations, the comparison between existing mm observations of young and forming disks, and the results of our model. We discuss whether the type of structures generated by our model will be detectable with future ALMA observations. In Sect. 2.3, we explore the relation of our model to the predictions of current simulations of the magnetorotational instability (MRI) (Balbus & Hawley 1991). Finally, Sect. 2.4 summarizes our results and the conclusions of this work.

2.1 Dust evolution model

We used the model presented in Birnstiel et al. (2010a) to calculate the evolution of the dust surface density in a gaseous disk, the radial drift, and the amount of turbulent mixing. The dust size distribution evolves owing to the grain growth, cratering, and fragmentation. We accounted for the relative velocities caused by Brownian motion, turbulence, and both radial and azimuthal drift, as well as vertical settling are taken into account.

In this work, we do not consider the viscous evolution of the gas disk because the aim is to investigate how dust evolution is influenced by the stationary perturbations of an otherwise smooth gas surface density. The effects of a time-dependent perturbation and the evolution of the gas disk will be the subject of future work. For a comprehensive description of the numerical code, we refer to Birnstiel et al. (2010a).

To simulate the radial pressure maxima that allow the trapping of particles, we consider a perturbation of the gas surface density that is assumed for simplicity to be a sinusoidal perturbation such that

$$\Sigma'(r) = \Sigma(r)\left(1 + A\cos\left[2\pi\frac{r}{L(r)}\right]\right), \tag{2.1}$$

where the unperturbed gas surface density $\Sigma(r)$ is given by the self similar solution of Lynden-Bell & Pringle (1974)

$$\Sigma(r) = \Sigma_0\left(\frac{r}{r_c}\right)^{-\gamma}\exp\left[-\left(\frac{r}{r_c}\right)^{2-\gamma}\right], \tag{2.2}$$

where r_c is the characteristic radius, taken to be 60AU, and γ is the viscosity power index equal to 1, which are the median values found from high angular resolution imaging in the sub-mm of disks in the Ophiucus star-forming regions (Andrews et al. 2010). The wavelength $L(r)$ of the sinusoidal perturbation depends on the vertical disk scale-height $H(r)$ by a factor f as

$$L(r) = fH(r), \tag{2.3}$$

with $H(r) = c_s\Omega^{-1}$, where the isothermal sound speed c_s is defined as

$$c_s^2 = \frac{k_B T}{\mu m_p}, \tag{2.4}$$

and the Keplerian angular velocity Ω is

$$\Omega = \sqrt{\frac{GM_\star}{r^3}}, \tag{2.5}$$

where k_B is the Boltzmann constant, m_p is the mass of the proton, and μ is the mean molecular mass, which in proton mass units is taken as $\mu = 2.3$. For an ideal gas, the pressure is defined as

$$P(r, z) = c_s^2 \rho(r, z), \tag{2.6}$$

where $\rho(r, z)$ is the gas density, such that $\Sigma'(r) = \int_{-\infty}^{\infty} \rho(r, z) dz$. With the surface density described by Eq. 2.1, we can have pressure bumps such that the wavelength increases with radius. These bumps are static, which may not be entirely realistic. However, these can be a good approximation of long-lived, azimuthally extended pressure bumps,which might for instance be the result of MHD effects (see Johansen et al. 2009; Dzyurkevich et al. 2010). The influence of time-dependent pressure perturbations (e.g. Laughlin et al. 2004; Ogihara et al. 2007) on the dust growth process will be the topic of future work. The left plot of Fig. 2.1 (dashed lines) shows the behavior of the perturbed surface density for two values of the amplitude and fixed value of the width. The right plot of Fig. 2.1 shows the corresponding pressure gradient.

The very fine dust particles move with the gas because they are strongly coupled to the gas because the stopping time is very short. In the presence of a drag force, the stopping time is defined as the time that a particle, with a certain momentum, needs to become aligned to the gas velocity. However, when the particles are large enough and they do not move with the gas, they experience a head wind, because of the sub-Keplerian velocity of the gas, hence lose angular momentum and move inwards. In this case, the resulting drift velocity of the particles is given by Weidenschilling (1977)

$$u_{\text{drift}} = \frac{1}{\text{St}^{-1} + \text{St}} \frac{\partial_r P}{\rho \Omega}. \tag{2.7}$$

Comparing Eq. 2.7 with the expression for the drift velocity given by Birnstiel et al. (2010a) (Eq. 19), we find that the drag term for the radial movement of the gas is not taken here since we assume a stationary gas surface density. The Stokes number, denoted by St, describes the coupling of the particles to the gas. The Stokes number is defined as the ratio of the eddy turn-over time ($1/\Omega$) to the stopping time. For larger bodies, the Stokes number is much greater than one, which implies that the particles are unaffected by the gas drag and consequently move on Keplerian orbits. When the particles are very small, $\text{St} \ll 1$, they are strongly coupled to the gas. Since the gas orbits at sub-Keplerian velocity because of its pressure support, there is a relative velocity between the dust particles and the gas. The Stokes number is equal to unity when the particles are still influenced by

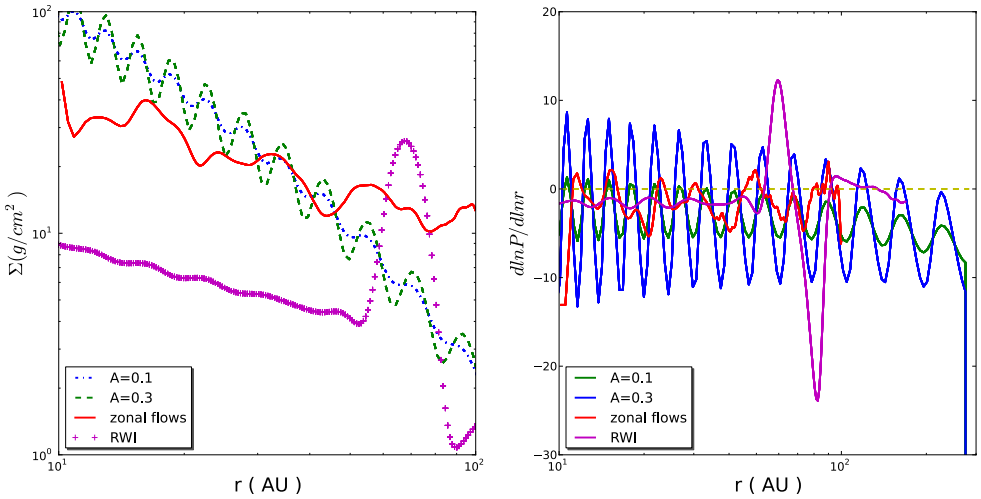

Figure 2.1: Comparison between the gas surface density (left plot) taken in this work (Eq. 2.1) for two different values of the amplitude and constant width (dashed and dot-dashed lines). The Rossby wave instability (Regály et al. 2012), and the presence of zonal flows caused by MHD instabilities (Uribe et al. 2011). Right plot shows the pressure gradient for each of the gas surface density profiles.

the gas drag but not completely coupled to the gas, instead being marginally coupled and moving at speeds between the Keplerian and the sub-Keplerian gas velocity.

The retainment of dust particles owing to pressure bumps depends on the size of the particles. Since very small particles, with St $\ll 1$, are tightly coupled to the gas, they do not drift inwards. However, radial drift becomes significant when the size of the particles increases and reaches its strongest value when St=1 (see Eq. 2.7). In the Epstein regime, where the ratio of the mean free path of the gas molecules $\lambda_{\rm mfp}$ to the particle size, denoted by a, satisfies $\lambda_{\rm mfp}/a \geq 4/9$, the Stokes number is given by

$$\mathrm{St} = \frac{a\rho_s}{\Sigma_g}\frac{\pi}{2}, \tag{2.8}$$

where ρ_s is the solid density of the dust grains, which is assumed to be constant (see Table 2.1). In this case, particles are small enough to be in this regime. Parameterizing the radial variation in the sound speed via

$$c_s \propto r^{-q/2}, \tag{2.9}$$

where for a typical disk, the temperature is assumed to be a power law such

Table 2.1: Parameters of the model

Parameter	Values
A	$\{0.1; 0.3; 0.5; 0.7\}$
f	$\{0.3; 0.7; 1.0; 3.0\}$
α	10^{-3}
$R_\star[R_\odot]$	2.5
$T_\star[K]$	4300
$M_{disk}[M_\odot]$	0.05
$\rho_s[g/cm^3]$	1.2
$v_f[m/s]$	10

that $T \propto r^{-q}$, which is an approximation to the temperature profile taken for this model. Therefore, the wavelength of the perturbation $L(r)$ scales as:

$$L(r) = fH(r) \propto fr^{(-q+3)/2}. \tag{2.10}$$

The pressure bumps have the same amplitude A and wavelength $L(r)$ as the density, because the over-pressure is induced by adding inhomogeneities to the gas surface density and parameterizing the temperature on the mid-plane by a power law (Nakamoto & Nakagawa 1994). The model taken here can artificially imitate e.g. the case of zonal flows in protoplanetary disks, where over-densities create pressure bumps. Zonal flows are formed by MRI, which depend on the degree of ionization in the disk, i.e. on the temperature of the disk and other factors such as the exposure to cosmic and stellar rays. The MRI appears to be the most probable source of turbulence, and if the turbulence is not uniform, there can be excitation of long-lived pressure fluctuations in the radial direction. For instance, Johansen et al. (2009) performed shearing box simulations of a MRI turbulent disk that exhibit large scale radial variations in Maxwell stresses of 10%. Dzyurkevich et al. (2010) presented three-dimensional (3D) global non-ideal MHD simulations including a dead zone that induces pressure maxima of $20 - 25\%$. Uribe et al. (2011) presented 3D global MHD simulations, leading to pressure bumps of around 25%. However, when the viscosity drops, the gas surface density changes causing a local inversion of the pressure gradient and an accumulation of dust particles. This matter accumulation causes Rossby wave instabilities (Lovelace et al. 1999) that lead to non-axisymmetric distributions in the disk, which we cannot exactly model at this moment since our dust evolution models are axisymmetric.

To constrain the values of the amplitude and wavelength of the perturbation, we take into account three different factors. First, it is important to

analyze the necessary conditions to have a local outward movement of the dust particles. Second, we compare our assumptions with current studies of zonal flows (Johansen et al. 2009; Uribe et al. 2011). And thirdly, we only work with small-enough amplitude disturbances such that the disk has an angular momentum per unit mass that increases outwards, meaning that it is Rayleigh stable .

The Rayleigh criterion establishes that for a rotating fluid system, in the absence of viscosity, the arrangement of angular momentum per unit mass is stable if and only if it increases monotonically outward (Chandrasekhar 1961), implying that

$$\frac{\partial}{\partial r}(rv_\phi) > 0. \tag{2.11}$$

Since turbulence is necessary to ensure angular momentum transport, instabilities may occur if a magnetic field is present, and in those cases the angular velocity decreases with radius (MRI). For a typical $\alpha-$turbulent disk, the MRI scale time is much longer than the time needed by the disk to recover the Rayleigh stability, which implies that the disk should remain quasi-stable at all times (Yang & Menou 2010). Any perturbation in the gas surface density that is Rayleigh unstable will almost instantly diminish sufficiently to ensure that the gas becomes Rayleigh stable again, thereby lowering its amplitude. This happens on a scale time that is much shorter than what MRI could ever counteract. The angular velocity of Eq. 2.11 is given by

$$v_\phi^2 = v_k^2 + \frac{r}{\rho}\frac{\partial P}{\partial r} = v_k^2(1-2\eta) \tag{2.12}$$

where

$$\eta = -\frac{1}{2r\Omega^2\rho}\frac{\partial P}{\partial r}. \tag{2.13}$$

The Rayleigh stability of the disk depends on the amplitude and the width of the bumps. In this case, we wish to study the influence of the amplitude of the perturbation, such that for this analysis we constrain the value of the wavelength of the perturbation, where f equals to unity, such that it remains consistent with the values expected from predictions of zonal flows models by Uribe et al. (2011) (see Fig. 2.1).

Taking the perturbed gas density of Eq. 2.1 and $f = 1.0$, it is possible to find the upper limit of the amplitude to satisfy Eq. 2.11, i.e. the condition to remain Rayleigh stable at all times. This calculation allows the maximum value of the amplitude A to be at most $\sim 35\%$ of the unperturbed density.

Various investigations have focused on the possibility of Rayleigh instabilities when disks have sharp peaks in their radial density profiles (see e.g. Papaloizou & Lin (1984), Li et al. (2001), and Yang & Menou (2010)). These profiles can exist when the temperature in the midplane is insufficient to ionize the gas (Gammie 1996) and as a result the turbulence parameter α decreases. These regions are known as "dead zones" and these are possible locations for the formation of planet embryos. In the boundaries of these regions, Varnière & Tagger (2006) showed that it is possible to have a huge vortex with a local bump in the gas surface density. Lovelace et al. (1999) demonstrated that these perturbations create an accumulation of gas that leads to the disk being unstable to Rossby wave instability (RWI). As a comparison of the amplitudes generated by RWI vortices and the amplitudes of our perturbations, the left plot of Fig. 2.1 also shows the azimuthally average gas surface density of a large-scale anticyclonic vortex modeled by Regály et al. (2012). In these cases, the equilibrium of the disk is affected in such a way that the disk becomes Rayleigh unstable. Since we focus on perturbations that allow the disks to remain Rayleigh stable at all evolutionary times, we do not consider our perturbed density to be similar to this kind of amplitudes.

Since the drift velocity is given by Eq. 2.7, to prevent an inward drift, the value of η from Eq. 2.13 must be negative, implying that the pressure gradient has to be positive in some regions of the disk. Doing this calculation for the condition that $\eta < 0$, we get that the values of the amplitude A have to be at least about 10%. In right plot of Fig. 2.1, we see that with an amplitude of 10% the pressure gradient barely reaches positive values in the inner regions of the disk ($\lesssim 50$ AU). Summarizing the upper and lower values of the amplitude, we should find that $0.10 \lesssim A \lesssim 0.35$, when the width of the perturbation is taken to be $f = 1$.

Taking into account the growth-fragmentation cycle and the existence of pressure bumps, the radial drift efficiency can be lower if the bumps have appropriate values of the amplitude and the length scale. When the particles grow by coagulation, they reach a certain size with velocities high enough to cause fragmentation (fragmentation barrier). The two main contributors to the of relative velocities are the radial drift and the turbulence. In the bumps, the radial drift can be zero if the pressure gradient and the azimuthal relative velocities are high enough; however there are still non-zero relative velocities owing to the turbulence. Therefore, it is necessary to have this condition, to ensure that the particles do not reach the threshold where they fragment. The maximum turbulent relative velocity between particles, with $\mathrm{St} \sim 1$, is given by Ormel & Cuzzi (2007)

$$\Delta u_{max}^2 \simeq \frac{3}{2}\alpha \mathrm{St} c_s^2, \tag{2.14}$$

where Eq. 2.14 is off by a factor of 2 for St $\lesssim$ 0.1. Therefore, to break through the mm size barrier, we must ensure that $\Delta u_{\max}$ is smaller than the fragmentation velocities of the particles v_f. Collision experiments using silicates (Güttler et al. 2010) and numerical simulations (Zsom et al. 2010) show that there is an intermediate regime between fragmentation and sticking, where particles should bounce. In this present study, we did not take into account this regime because there are still many open questions in this field. For example, Wada et al. (2011) suggest that there is no bouncing regime for ice particles that may be present in the outer regions of the disks (see Schegerer & Wolf 2010). Laboratory experiments and theoretical work suggest that typical fragmentation velocities are on the order of few m s^{-1} for silicate dust (see e. g. Blum & Wurm 2008). Outside the snow-line, the presence of ices affects the material properties, making the fragmentation velocities increase (Schäfer et al. 2007; Wada et al. 2009). Since in this work we consider a radial range from 1AU to 300AU, the fragmentation threshold velocity is assumed to be v_f = 10m s^{-1}. All the parameters used for this model are summarized in Table 2.1.

For particles with St $\lesssim$ 1, taking the size at which the turbulent relative velocities $\Delta u_{\max}$ are as high as the fragmentation velocity v_f, we can find the maximum value of the grain size, which is

$$a_{\max} \simeq \frac{4\Sigma_g}{3\pi\alpha\rho_s}\frac{v_f^2}{c_s^2} \tag{2.15}$$

where $a_{\max}$ is valid only for St $\lesssim$ 1 because for larger bodies the turbulent relative velocities are smaller than the given in Eq. 2.14 (for a detailed discussion of the turbulent relative velocities see Ormel & Cuzzi (2007)).

The dust grain distribution $n(r, z, a)$ is the number of particles per cubic centimeter per gram interval in particle mass, which depends on the grain mass, the distance to the star r, and theheight above the mid-plane z, such that

$$\rho(r, z) = \int_0^\infty n(r, z, a) \cdot m dm \tag{2.16}$$

is the total dust volume density. The quantity $n(r, z, a)$ can change because of the grain growth and distribution of masses via fragmentation. The vertically integrated dust surface density distribution per logarithmic bin is defined to be

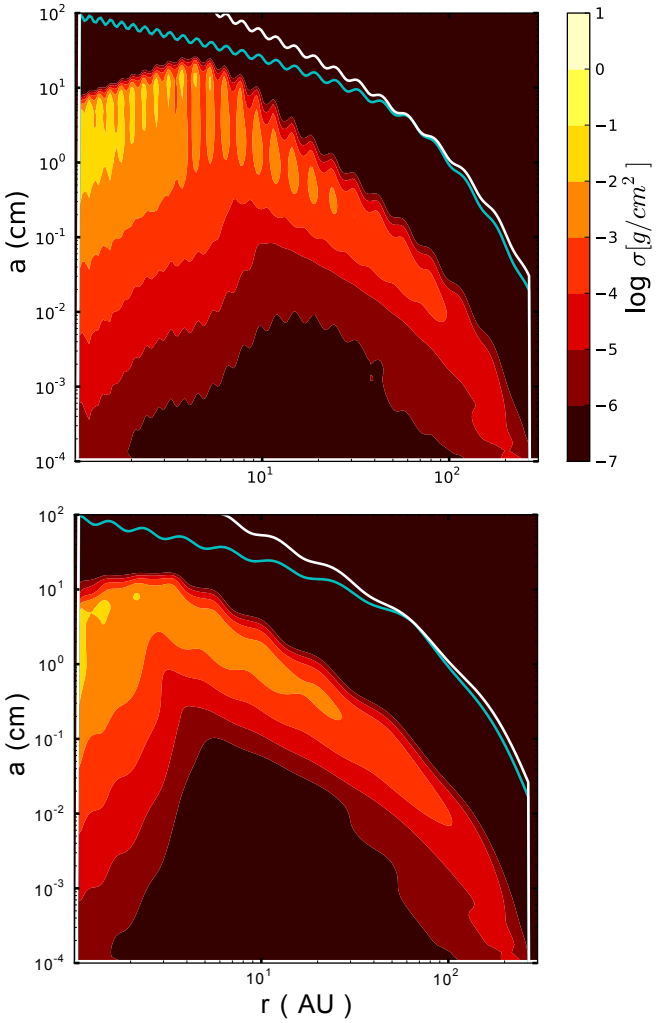

Figure 2.2: Vertically integrated dust density distribution at 1 Myr for $A = 0.1$ and $f = 1$ (top) and $A = 0.1$ and $f = 3$ (bottom). The white line shows the particle size corresponding to a Stokes number of unity, which shows the same shape as the gas surface density Σ' of Eq. 2.1 (see Eq. 2.8). The blue line represents the maximum size of the particles before they reach fragmentation velocities (fragmentation barrier according to Eq. 2.15).

$$\sigma(r,a) = \int_{-\infty}^{\infty} n(r,z,a) \cdot m \cdot a dz \tag{2.17}$$

and the total dust surface density is then

$$\Sigma_d(r) = \int_0^{\infty} \sigma(r,a) d\ln a. \tag{2.18}$$

2.2 Results

In this section we describe our results of dust evolution, the comparison to current mm observations of young disks and the observational signatures of our model that we will detect using ALMA.

2.2.1 Density distribution of dust particles

The simulations were performed for a disk of mass $0.05 M_\odot$, with a surface density described by Eq. 2.1 from 1.0 AU to 300 AU, around a star with one solar mass. The turbulence parameter α is taken to be 10^{-3}, unless another value is specified. Figure 2.2 shows the vertically integrated dust density distribution, taking into account coagulation, radial mixing, radial drift, and fragmentation, after 1 Myr of the evolution of the protoplanetary disk. The solid white line shows the particle size corresponding to a Stokes number of unity. From Eq. 2.8, we can see that when St=1, the particle size a is proportional to the gas surface density Σ', and the solid line then reflects the shape of the surface density. The blue line of Fig. 2.2 represents the fragmentation barrier, which illustrates the maximum size of the particles before they reach velocities larger than the fragmentation velocity (see Eq. 2.15). Hence, particles above the fragmentation barrier should fragment to smaller particles, which again contribute to the growth process.

Both plots of Fig. 2.2 have the same amplitude of the sinusoidal perturbation $A = 0.1$. The factor f, which describes the width of the perturbation, is taken to be $f = 1$ in the top plot, and $f = 3$ in the bottom plot of Fig. 2.2.

This result shows the following. First, the amplitude $A = 0.1$ of the perturbation is not high enough to have a positive pressure gradient in those regions (see right plot of Fig. 2.1) such that particles can be retained in the outer regions of the disk after some Myr. Instead the dust particles are still affected by radial drift and turbulence such that the particles do not grow to larger than mm size in the outer regions.

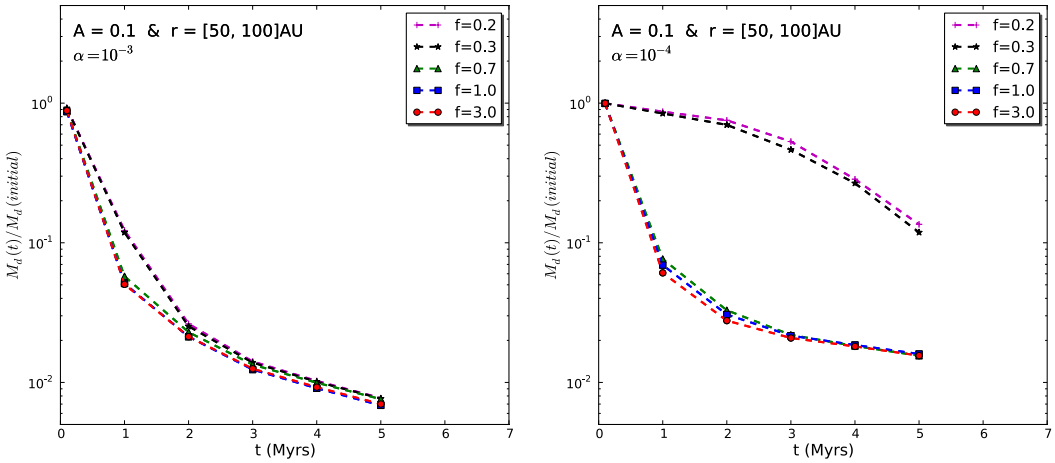

Figure 2.3: Ratio between final and the initial dust mass between 50 AU and 100AU, at different times of evolution. Taking a constant value of the amplitude $A = 0.1$ and different values of the width of the perturbed density (Eq. 2.1). For $\alpha = 10^{-3}$, we present our results in the left plot and for $\alpha = 10^{-4}$ in the right plot.

Second, taking a greater value of the factor f, at the same amplitude, implies that the retention of particles is even weaker. This is because with a wider perturbation is it harder to have positive pressure gradient. For a smaller value of f, the pressure gradient is expected to be higher because the surface profile should be steeper, hence any dust trapping much more efficient. However, the diffusion timescale τ_ν depends quadratically on the length scale ℓ. Therefore, when the wiggles of the perturbation are assumed to have a shorter wavelength, the diffusion times become much shorter, implying that the turbulence mixing ejects the dust particles from the bumps more rapidly, even when the surface density is steeper for narrow wiggles. More precisely, $\tau_\nu \propto \ell^2 \nu^{-1}$ where the viscosity is defined as $\nu = \alpha c_s h$. For this reason, we note in Fig. 2.3-left plot that the trapping is more effective taking values of the width less than one, but only by a very small margin. As a result, the ratio of the final to the initial mass of the dust for $r \in [50, 100]$AU remains almost constant when the width is taken to be larger than 0.3. We conclude that for an amplitude of A=0.1, the trapping after several million years does not become more effective when the wavelength of the perturbation is assumed to be shorter.

Only when the diffusion timescales become larger or equal to the drift timescales for a given pressure profile, turbulence parameter and Stokes number, can the dust particles be retained inside the bumps and therefore grow.

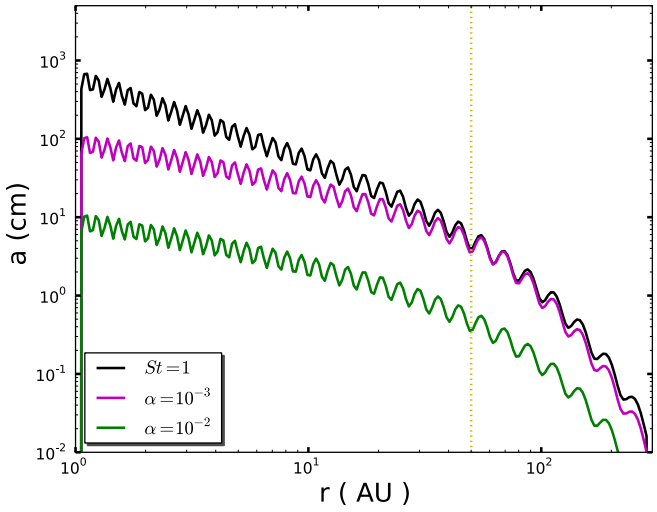

Figure 2.4: Particle size corresponding to a Stokes number of unity for $A = 0.3$ and $f = 1.0$ and location of the fragmentation barrier for two different values of the turbulent parameter α. The dashed line corresponds to $r = 50$AU to distinguish the maximum size particle in the outer regions of the disk for each case.

From Eq. 2.7, we can deduce that the drift timescales can be given by $\tau_{\rm drift} \propto \ell(\partial_\ell P)^{-1}$, where within the bumps ℓ is the width of the perturbations (which depends directly on f). As a consequence, after an equilibrium state is reached, both the drift and diffusion timescales are proportional to the square of the width. Accordingly, for a given value of f, the effects of turbulent mixing and radial drift cancel.

We note in Fig. 2.3 that for f=$\{0.3, 0.2\}$ there is a small effect on the retention of particles for $\alpha = 10^{-3}$ (left plot) and a significant effect for $\alpha = 10^{-4}$ (right plot). This implies that for these values of f and A, the pressure gradient becomes positive enough in the outer regions ($r \in [50, 100]$AU) to trap the particles. Since A and f are the same in both cases, the pressure gradient is exactly the same. However, for $\alpha = 10^{-3}$, the low efficiency that becomes evident when f is reduced, vanishes after two Myr, because turbulent mixing and radial drift cancel each other.

Nevertheless, when α is lowered by one order of magnitude (right panel of Fig. 2.3), the diffusion timescales become longer. In this case, the drift timescales become shorter than the diffusion timescales, hence the ratio of the final to the initial dust mass increases on average for each f. When f is small enough for there to be positive pressure gradient (f=$\{0.3, 0.2\}$), outward drift wins over turbulent mixing, and as a result the trapping of

particles is a visibly effective. However, there is almost no difference between f=0.3 and f=0.2. On contrast, this counterbalance effect between radial drift and turbulence when f varies does not happen when the amplitude of the perturbation changes.

We fixed the value of the width of the perturbation to unity, because this value is consistent with current model predictions of zonal flows. The comparison between our assumption of the density inhomogeneities and the work of Uribe et al. (2011) is discussed in Sect. 2.3. In addition, for larger values of the width, we should have higher values of the amplitudes to maintain a positive pressure gradient. In this case, however the disk easily becomes Rayleigh unstable when the amplitude increases. These are the reasons why we fix the value of the width to unity and no higher.

Simulations of MRI-active disks suggest that the typical values of the turbulence parameter α are in the range of $10^{-3} - 10^{-2}$ (Johansen & Klahr 2005; Dzyurkevich et al. 2010). In this work, we focus on the results for $\alpha = 10^{-3}$, because for greater turbulence the viscous timescales become shorter than the growth timescales of the dust, causing the particles to escape from the bumps and then drift radially inwards before any mm-sizes are reached. In addition, if α is taken to be one order of magnitude higher, the fragmentation barrier is lower by about one order of magnitude in grain size, implying that particles do not grow to grater than mm-sizes in the outer regions of the disk (see Eq. 2.14). Fig. 2.4 shows the location of the fragmentation barrier for the case of $A = 0.3$ and $f = 1.0$ and two different values of α. We note that the maximum value of the grain size for the case of $\alpha = 10^{-2}$ is on the order of a few mm in the outer regions of the disk $r > 50$AU, while for $\alpha = 10^{-3}$ the grains even reach cm-sizes.

Figure 2.5 compares the surface density distribution for two different values of the amplitude of the perturbation $A = 0.1$ and $A = 0.3$, at different evolution times. Taking $A = 0.3$, we note that in the pressure bumps there is a high density of dust particles, even after 5 Myr of evolution for a maximum radius around 80 AU. For $A = 0.3$ and $r \gtrsim 100$AU, there is a small amount of particles above the fragmentation barrier for the different times of evolution. We note that the line of the fragmentation barrier given by Eq. (2.15) was calculated by taking into account only turbulent relative velocities, since radial and azimuthal turbulence relative velocities were assumed to be zero at the peaks of the bumps. Particles with St> 1 were no longer strongly coupled to the gas, hence they are not affected by gas turbulence, and the relative velocities produced by turbulence were smaller, implying that they had been able to grow over the fragmentation barrier. Moreover, we can see in the right plot of Fig. 2.1 that the pressure gradient for $A = 0.3$ and $r \gtrsim 100$AU is always negative, hence for those regions the pressure bumps may not re-

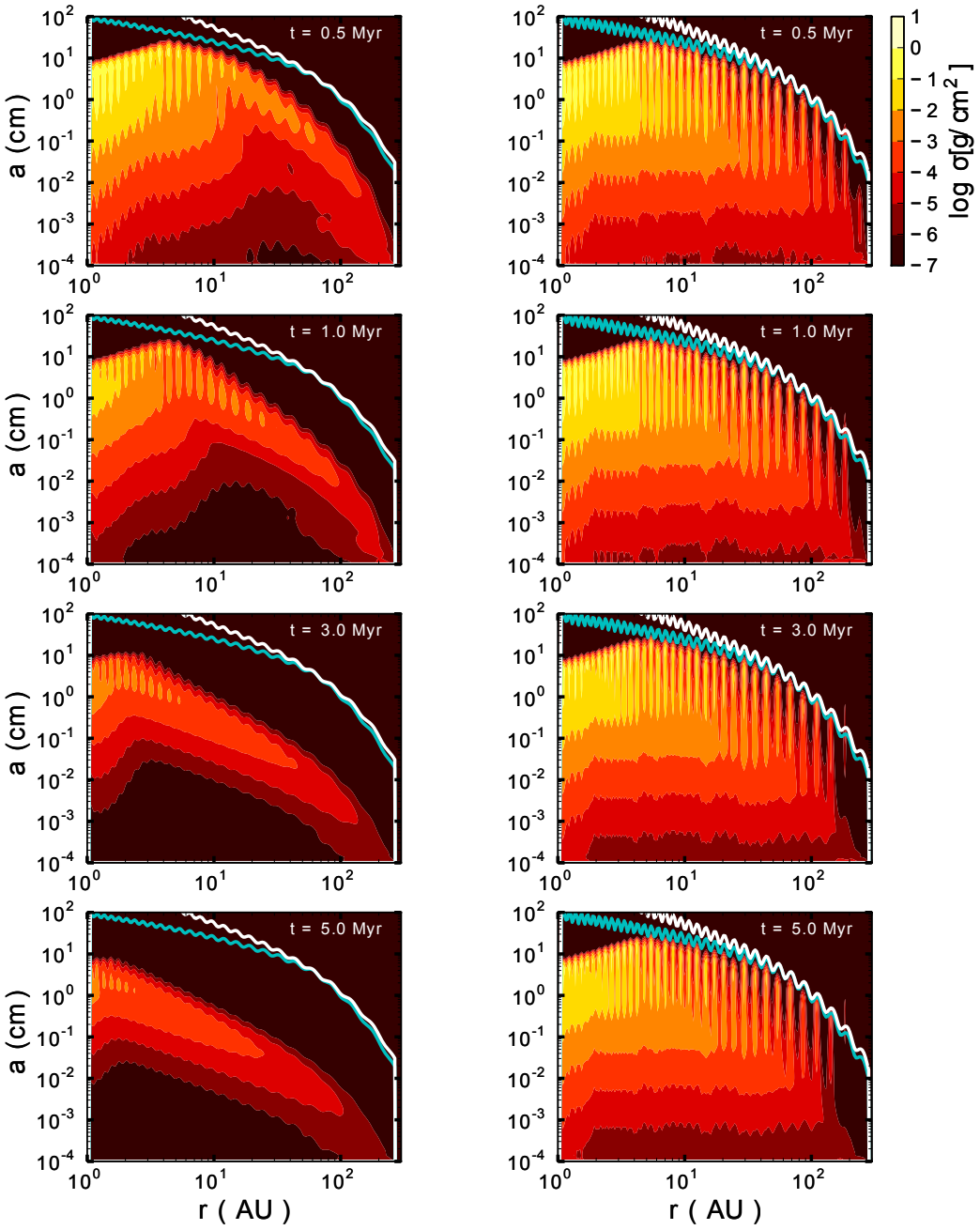

Figure 2.5: Vertically integrated dust density distribution with a fixed value of length scale of $f = 1$, for $A = 0.1$ (left column) and $A = 0.3$ (right column) at different times 0.5 Myr, 1.0 Myr, 3.0 Myr, and 5.0 Myr from top to bottom, respectively. The solid white line shows the particle size corresponding to a Stokes number of unity. The blue line represents the fragmentation barrier according to Eq. 2.15.

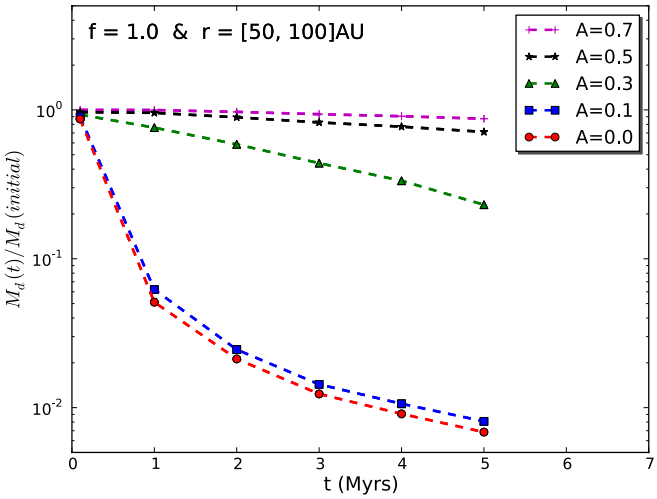

Figure 2.6: Ratio of the final to the initial dust mass between 50 AU and 100 AU, at different times of evolution. We assumed a constant value of the width $f = 1.0$ and different values of the amplitude of the perturbed density (Eq. 2.1).

duce the efficacy of radial drift. Therefore, the total relative velocities for $r \gtrsim 100$AU can decrease, leading some particles (with St> 1) to grow beyond the fragmentation barrier. Only the particles with St< 1 and that exceed the fragmentation barrier should eventually fragment to smaller particles. For regions $r \lesssim 100$AU, dust particles continuously grow to mm-size particles by coagulation because the collision velocities produced by turbulence are smaller that the assumed fragmentation velocity v_f.

As we have mentioned before, the efficiency of the dust trapping depends on the amplitude of the pressure bumps. It is expected that for higher amplitudes there is a greater trapping of particles because the pressure gradient is also more positive (see right plot of Fig. 2.1). Taking the perturbed density of Eq. 2.1, we can see in Fig. 2.6 that between 50 AU and 100 AU from the star, the amount of dust grows significantly from $A = 0.1$ to $A = 0.3$. From $A = 0.3$ to $A = 0.5$, there is still a considerable growth, but the rate of growth is slower. From $A = 0.5$ to $A = 0.7$, the rate remains almost constant, reaching a threshold. When the amplitude is increased, the amount of dust particles retained in the bumps increases to a limit when the dust growth stops because the particles reach the maximum possible value where they start to fragment owing to the high relative velocities.

As we explained in Sect. 2.1, taking a fixed value of $f = 1.0$, the disk remains Rayleigh stable for $0.10 \lesssim A \lesssim 0.35$, which means that for those

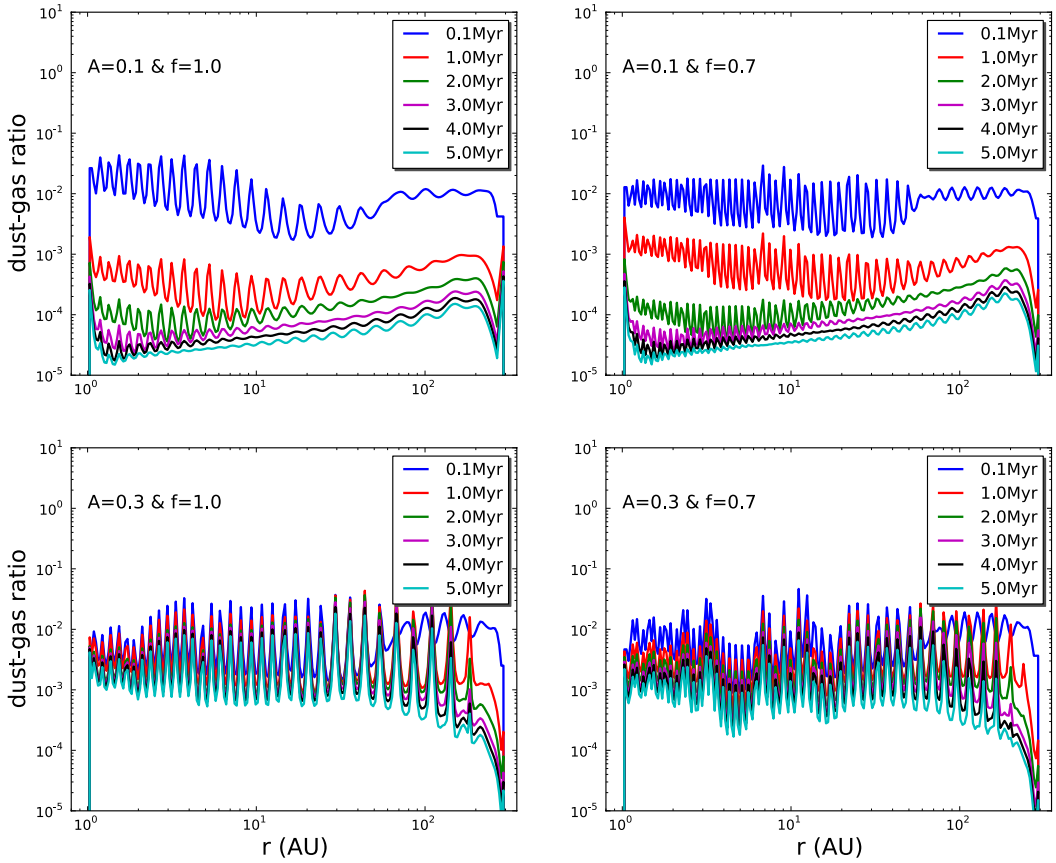

Figure 2.7: Dust-to-gas mass ratio in the disk for different times in the disk evolution and the parameters summarized in Table 2.1: $A = 0.1$ and $f = 1$ (top-left); $A = 0.3$ and $f = 1$ (bottom-left); $A = 0.1$ and $f = 0.7$ (top-right) and $A = 0.3$ and $f = 0.7$ (bottom-right).

values of the amplitude, these types of perturbations can be explained via MRI without any need to suggest that Rayleigh instability is present at any evolution time. The amplitude of $A = 0.3$ is the most consistent with current MHD simulations of zonal flows Uribe et al. (2011), where pressure reaches radial fluctuations of 25% (see left plot of Fig. 2.1). The amplitude of $A = 0.1$ is more consisted with the case of the pressure fluctuation of zonal flows of the order of 10% by Johansen et al. (2009).

Figure 2.7 shows the radial dependence of the dust-to-gas ratio for different times of the simulation, for two values of the perturbation amplitude and wavelength without the gas inward motion. For $A = 0.1$ and $f = 1.0$ (top-left plot of Fig. 2.7), we can see that the dust-to-gas ratio decreased significantly with time across the whole disk. This implies that the dust particles do not grow considerably with time, which is what we expected because with this amplitude the trapping of the particles into the pressure bumps is ineffective. Consequently, owing to turbulence the dust particles collide, fragment, and become even smaller, such that they mix and the retention of these small particles, with St$<$ 1, becomes more difficult. Thus, the radial drift is not reduced, the particles with St$\lesssim$ 1 drift inward. The particles that survive are those that have very small St$\ll$ 1, and are strongly coupled to the gas. Hence, the dust-to-gas ratio initially decreases quickly and then becomes almost constant with time, which implies that after several Myr only the very small dust particles remain. The top-right plot of Fig. 2.7 shows that taking the same amplitude but a shorter wavelength, the dust-to-gas ratio has the same behavior. This confirms that when α turbulence is constant, a decrease in the wavelength leads to shorter diffusion timescales. Therefore, the trapping is not more effective even if the surface density is steeper for narrow bumps.

In contrast, owing to the strong over-pressures at $A = 0.3$ (bottom plots of Fig. 2.7), the dust-to-gas ratio remains almost constant with time for $r < 100$AU, oscillating radially between $\sim 10^{-3}$ to $\sim 10^{-1}$. This oscillating behavior, even after 5 Myr of dust evolution, is possible because the particles are retained in the bumps and grow sufficient to increase the dust-to-gas ratio inside the bumps. Only around ~ 100AU from the star does the dust-to-gas ratio decrease slowly with time. This implies that for $r < 100$AU, the drift is counteracted by the positive local pressure gradient when the timescales for the growth are comparable to the disk evolution times, i. e. the viscous timescales. Changing the width of the perturbation to $f = 1.0$ for the left-bottom plot and $f = 0.7$ for the right-bottom plot of Fig. 2.7, has only a minor effect on the dust-to-gas ratio as explained before.

2.2.2 Comparison to current data of young disks in the millimeter range

We compared the models predictions of the disk fluxes at millimeter wavelengths with observational data obtained for young disks in Class II Young Stellar Objects (YSOs).

To do this, we calculated the time-dependent flux for the disk models described in Sect. 2.1. For the dust emissivity, we adopted the same dust model as Ricci et al. (2010a,b, 2011) and Birnstiel et al. (2010b), i.e. spherical composite porous grains made of silicates, carbonaceous materials, and water ice, with relative abundances from Semenov et al. (2003). At each stellocentric radius in the disk, the wavelength-dependent dust emissivity was calculated by considering the grain size number density $n(r, z, a)$ derived from the dust evolution models at that radius, as described in Sect. 2.1.

In the millimeter wavelength regime, the opacity can be approximated by a power law (Miyake & Nakagawa 1993), which means that the flux can be approximated to $F_\nu \propto \nu^{\alpha_{\rm mm}}$, where $\alpha_{\rm mm}$ is known as the spectral index. The spectral index gives us information about the size distribution of the dust in the disk. Figure 2.8 shows the time-dependent predicted fluxes at $\sim$ 1mm ($F_{\rm 1mm}$) and the spectral index between $\sim$ 1 and 3mm ($\alpha_{\rm 1-3mm}$) for a disk model with $f = 1$ and $A = 0.1$ (top panel) or $A = 0.3$ (bottom panel). In the same plot, we present mm-data for young disks in Taurus (Ricci et al. (2010a) and Ricci (priv comm)), Ophiucus (Ricci et al. 2010b), and Orion Nubula Cluster (Ricci et al. 2011) are also shown.

As detailed in Birnstiel et al. (2010b), the $F_{\rm 1mm}$ versus $\alpha_{\rm 1-3mm}$ plot reflects some of the main properties of the dust population in the disk outer regions, which dominate the integrated flux at these long wavelengths. In particular, the 1mm-flux density is proportional to the total dust mass contained in the outer disk. The mm-spectral index is instead related to the sizes of grains: values lower than about three are caused by emission from grains larger than about $\sim$ 1mm, whereas values around 3.5 are due to smaller grains (Natta et al. 2007).

In the case of the disk model with $f = 1$ and $A = 0.1$, the time evolution of the predicted mm-fluxes clearly reflects the main features of the dust evolution depicted in the top plot of Fig. 2.8. Grains as large as a few millimeters quickly form in the disk outer regions ($R \gtrsim 50$ AU), and most of them are initially retained in those regions ($\lesssim$ 0.5Myr). As a consequence, the mm-spectral index of the disk is slightly lower than 3 at these early stages. However, the radial drift of mm-sized pebbles becomes soon significant and, as already described in Sect. 2.2, perturbations with a length-scale of $f = 1$ and amplitude of $A = 0.1$ are inefficient in retaining mm-sized particles in

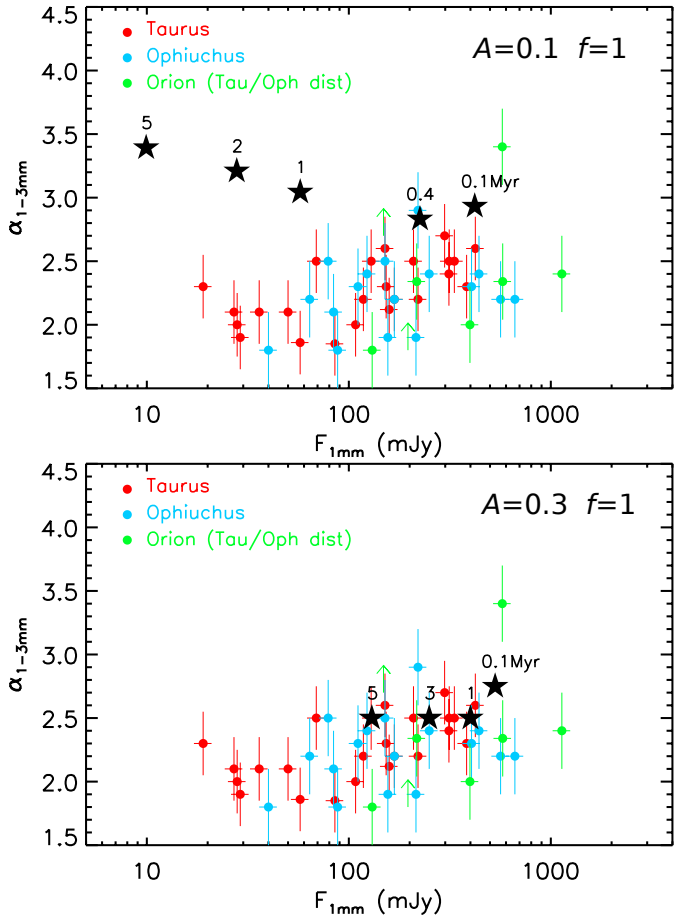

Figure 2.8: Comparison of the observed fluxes at mm-wavelengths of young disks in Taurus (red dots; from Ricci et al. (2010a) and Ricci (priv comm)), Ophiucus (blue dots; from Ricci et al. (2010b)), and Orion Nebula Cluster (green dots; from Ricci et al. (2011)) star-forming regions with the predictions of the disk models at different times in the disk evolution (star symbols). Disk ages are indicated by numbers, in Myr, above the star symbols. The predicted $\sim$ 1 mm-fluxes (x-axis) and spectral indices between $\sim$1mm and 3mm (y-axis) are for the disk models presented in Sect. 2.1 with perturbations characterized by $f = 1$ and either $A = 0.1$ (top panel) or $A = 0.3$ (bottom panel). The $\sim$ 1mm-flux densities for the Orion disks have been scaled by a factor of $(420\text{pc}/140\text{pc})^2$ to account for the different distances estimated for the Orion Nebula Cluster ($\sim$ 420pc, Menten et al. (2007)) and Taurus and Ophiucus star-forming regions ($\sim$ 140pc, Bertout et al. (1999), Wilking et al. (2008))

the outer disk. The 1 mm-flux density significantly decreases because of the loss of dust from the outer regions, especially the mm-sized grains, which are efficient emitters at these wavelengths. Given that the spectral index is a proxy for the grain size, which is also affected by radial drift, its value increases with time because of the gradual loss of mm-sized pebbles in the outer disk. In this case, the under-predicted fluxes are inconsistent with observational data for disk ages $\gtrsim$ 1Myr, i.e. with the mean estimated ages of PMS stars in the Taurus, Ophiucus, and Orion regions.

Interestingly, a disk with perturbations in the gas surface density with a larger amplitude of $A = 0.3$ shows different results. In this case, the trapping of particles in the pressure bumps is efficient enough to retain most of the large pebbles formed in the outer disk (see bottom plot of Fig. 2.8). Since radial drift is much less efficient in this case, the predicted 1mm-flux density is less affected than in the $A = 0.1$ case and, more importantly, the spectral index levels off at a value of $\sim$2.5. This model provides a good match to the bulk of the mm-data for disk ages of a few Myr, as seen in the bottom panel of Fig. 2.8.

We also note that the match between the model presented here for $A = 0.3$ is closer than that obtained by Birnstiel et al. (2010b). In contrast to the present work, these authors completely ignored radial drift, thus restricted particles to remain artificially in the disk outer regions. Specifically, for a disk with the same unperturbed disk structure presented here, they found a higher 1mm-flux density than we obtained in the $A = 0.3$ perturbation case at a few Myr. This indicates that to interpret the measured mm-fluxes of young disks we need to incorporate in our models both radial drift and a physical mechanism acting in the disk to trap, although not completely, mm-sized particles in the outer disk.

2.2.3 Future observations with ALMA

The Atacama Large Millimeter/sub-millimeter Array (ALMA) will provide an increase in sensitivity and resolution to observe in more detail the structure and evolution of protoplanetary disks. With a minimum beam diameter of $\sim$ 5 mas at 900GHz, ALMA will offer a resolution down to 2 AU for disks observed in Orion and sub-AU for disk in Taurus-Auriga (Cossins et al. 2010). Using the Common Astronomy Software Applications (CASA) ALMA simulator (version 3.2.0), we run simulations to produce realistic ALMA observations of our model using an ALMA array of 50 antennas 12m-each.

The selection of observing mode to obtain the images was chosen to have simultaneously the most favorable values for the resolution and sensitivity that should be available with ALMA. The spatial resolution depends on the

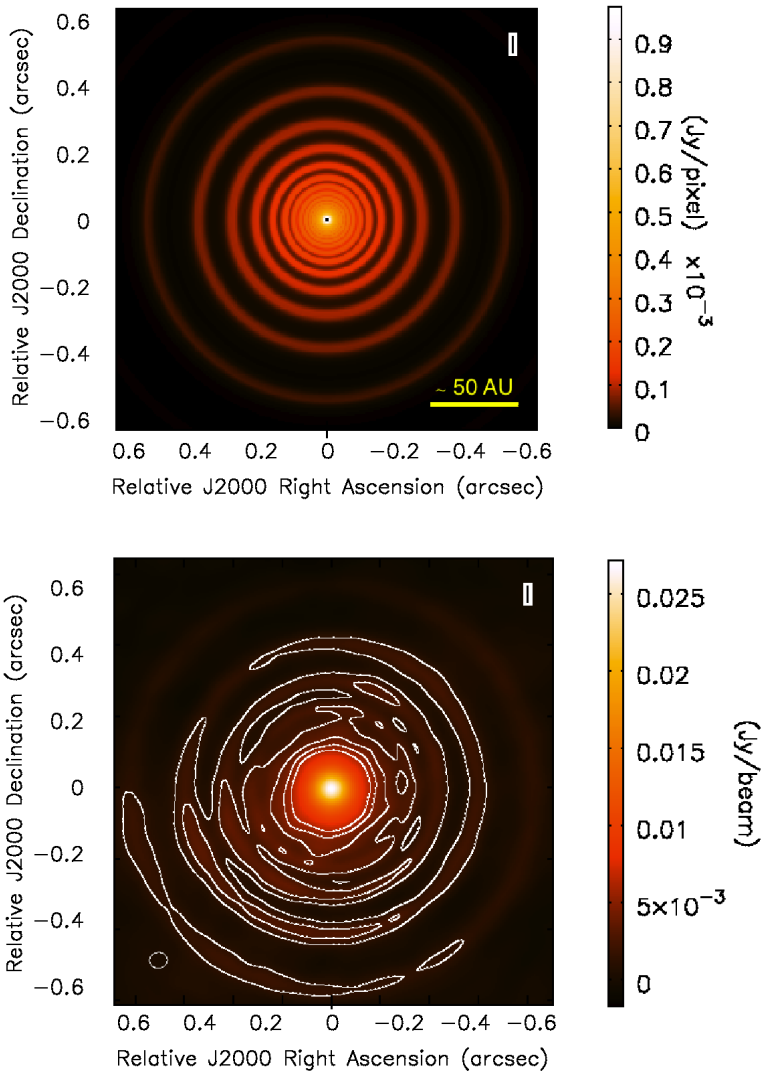

Figure 2.9: Disk image at 2 Myr and observing wavelength of 0.45 mm, the amplitude of the perturbation is $A = 0.3$ and the factor $f = 1$ for: disk model with parameters of Table 2.1 (top) and a simulated image using full configuration of ALMA (bottom) with a maximum value of baseline of around 3km and an observing time of 4 hours. The contour plots are at $\{2, 4, 6, 8\}$ for the corresponding rms value (see Table 2.2).

Table 2.2: Atmospheric conditions, total flux and rms for the simulated observations at 140pc and at different observing wavelengths. The pwv value takes into account the expected conditions for ALMA. The simulated images use the full ALMA configuration, but the antenna configuration is chosen to ensure the best agreement between resolution and sensitivity.

Amplitude	Wavelength	Atmospheric conditions		Total Flux	rms
	(mm)	pwv (mm)	τ_0	(Jy)	(Jy)
A=0.3	0.45	0.5	0.60	6.9×10^{-1}	7.5×10^{-4}
	0.66	1.0	0.40	7.6×10^{-1}	3.8×10^{-4}
	1.00	1.5	0.20	2.2×10^{-1}	1.4×10^{-4}
	3.00	2.3	0.03	4.0×10^{-1}	2.0×10^{-5}
A=0.1	1.00	1.5	0.20	1.6×10^{-2}	1.3×10^{-5}

observing frequency and the maximum baseline of the array. We did not consider the largest array because for very large baselines, the sensitivity could be not enough for the regions that we need to observe. Therefore, we used different antenna arrays depending on the observing frequency to achieve the highest possible resolution with enough sensitivity. The sensitivity depends on the number of antennas, the bandwidth (which is taken as $\Delta\nu = 8$GHz for continuum observations), and the total observing time that was fixed to four hours for each simulation. The sensitivity also depends on the atmospheric conditions. ALMA is located in Llano de Chajnantor Observatory, where the precipitable water vapor (pwv) varies between 0.5 mm and 2.0 mm depending on the observable frequency. For the simulations, we assumed that the value of the pwv varies with frequency (see Table 2.2). The synthetic images are fully consistent with the opacity dust distribution discussed in Sec. 2.2.2.

Figure 2.9 shows a comparison between the model image and a simulated ALMA image using the full configuration of ALMA with a maximum baseline of around 3 km and an observation total time of four hours. This image is for an observing wavelength of 0.45mm (band 9 of ALMA $620 - 750$ GHz). We note that the simulated images take into account the atmospheric conditions and the expected receiver noise based on technical information of the antennas, but the residual noise after data calibrations and its uncertainties are not considered. We note (see Fig. 2.9 - bottom plot) that with one of the full configurations (max. baseline ~ 3 km), it is possible to distinguish some ring structures because the dust has drifted considerably into the rings relative to the gas.

In Fig. 2.10, we note again the importance of having a high value of the amplitude. If the gas surface density of the disk is $A = 0.3$, then the

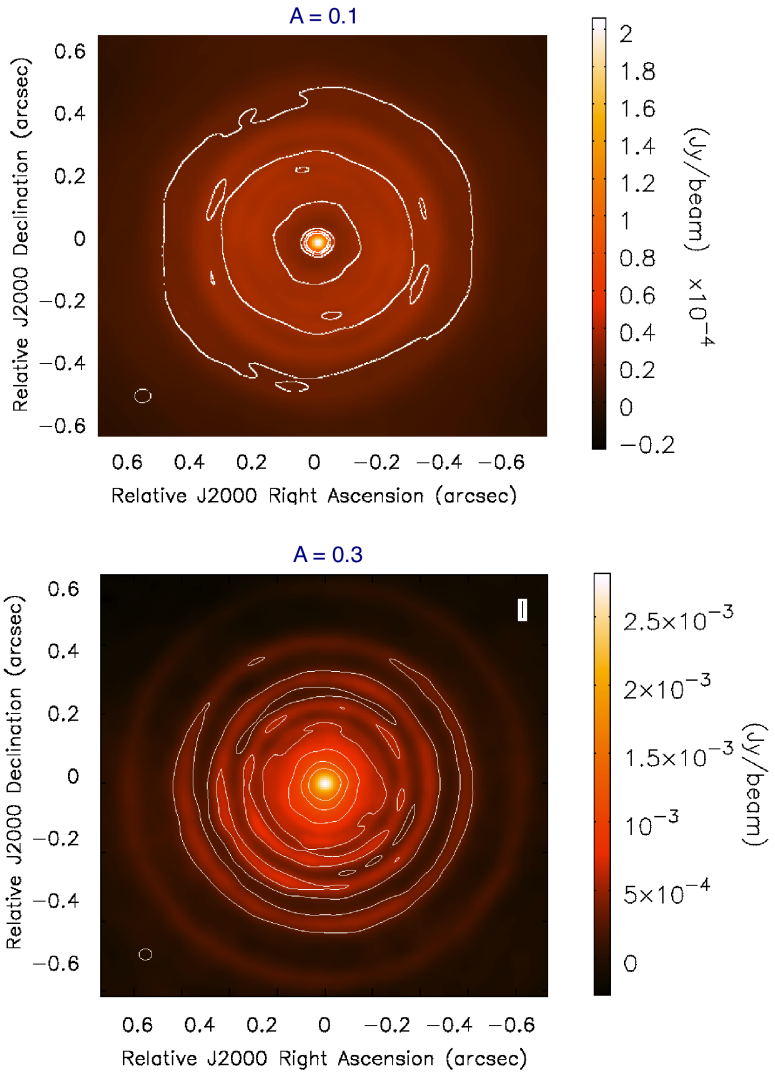

Figure 2.10: Comparison between the simulated images for an observing wavelength of 1 mm and 2 Myr of evolution, using the full antenna configuration of ALMA for two different values of the amplitude of the perturbation: $A = 0.1$ (top) and $A = 0.3$ (bottom). The contour plots are at $\{2, 4, 6, 8\}$, of the corresponding rms value (Table 2.2).

effects will be observable with ALMA. Both images of the figure have been computed with the complete antenna configuration of ALMA for an observing wavelength of 1 mm and 2 Myr of the disk evolution. We can see that for $A = 0.1$ it is impossible to detect any structures around the star even considering a perfect data calibration. We note that owing to the trapping of dust particles at the peaks of the pressure bumps, the contrasts between rings in the simulated images is very clear, around $\sim 20 - 25\%$, while the contrast for the gas is almost unrecognized.

Figure 2.11 compares the simulated images at different observing wavelengths using different antenna configurations of ALMA. The antenna configuration is chosen by CASA depending on the expected resolution. The highest quality image was obtained at 100 GHz and a maximum baseline of 16 km (most extended ALMA configuration), where it is possible to clearly detect the most external ring structure and some internal ring structures. Nevertheless, with more compact configurations at different frequencies it is still possible to detect some structures from the presence of the pressure bumps, which allow the formation of mm-sized particles. However, it is important to take into account that the simulated images of Figs. 2.9, 2.10, 2.11, and 2.12 assume a perfect data calibration after observations, and that for long baselines and high frequencies the calibration effects become more important.

Taking the ratio of the images at two different wavelengths, we evaluated the values of the spectral index α_{1-3mm}, which indicates the location of mm-sized grains. For the full configuration of ALMA and a maximum value of the baseline of 12 km for both observing frequencies, some regions with large particles are distinguished that are regions of low spectral index $\alpha_{1-3\mathrm{mm}} \lesssim 3$, as explained in Sec. 2.2.2. In Fig. 2.12, we present is the spectral index of the model data (top plot) and the spectral index for two simulated images at 0.45mm and 3.0mm, and a total observing time of four hours.

2.3 Approach to zonal flows predictions

We have so far assumed ad-hoc models of pressure bumps. We have not, however, considered the processes that may cause such long-lived bumps in protoplanetary disks? We now examine whether zonal flows are the origin of long-lived pressure bumps.

One possible origin of pressure bumps is MRI turbulence. Hawley et al. (1995) and Brandenburg et al. (1995) presented the first attempts to simulate the nonlinear evolution of MRI in accretions disk, taking a box as a representation of a small part of the disk. More recent simulations have

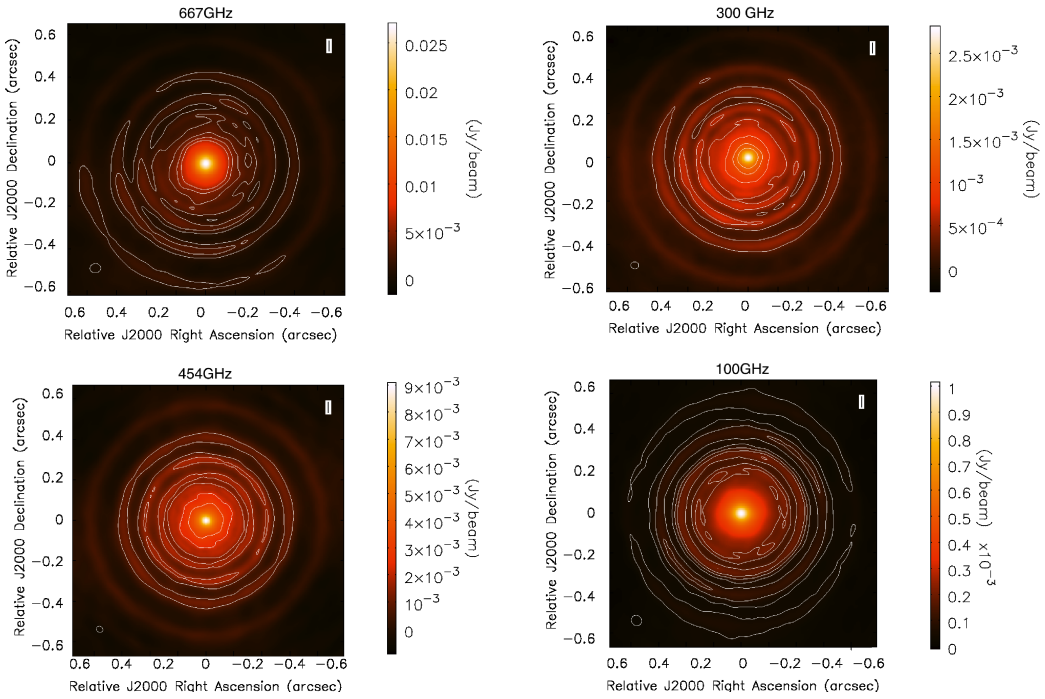

Figure 2.11: Disk simulated images with parameters of Table 2.1, $A = 0.3$ and $f = 1$ at 2 Myr of the disk evolution and for observing frequency of: 667 GHz with a maximum baseline of around 3 km (top left), 454 GHz (bottom left) with a maximum baseline of around 4 km, 300 GHz (top left) with a maximum baseline of around 7 km, and 100 GHz with a maximum baseline of 16 km (bottom right). The contour plots are at $\{2, 4, 6, 8\}$ the corresponding rms value (see Table 2.2)

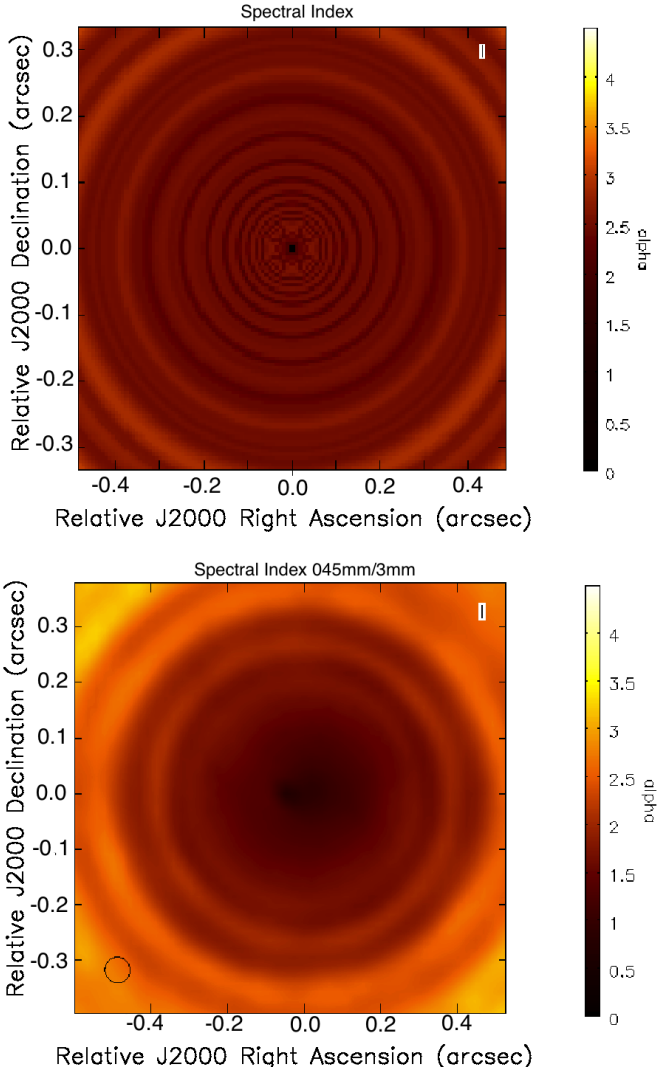

Figure 2.12: Spectral index $\alpha_{1-3\mathrm{mm}}$ of the model data (top plot) and the spectral index taking two simulated images at 0.45mm and 3.0mm, with a time observation of four hours and using the full configuration (maximum baseline of 12 km)

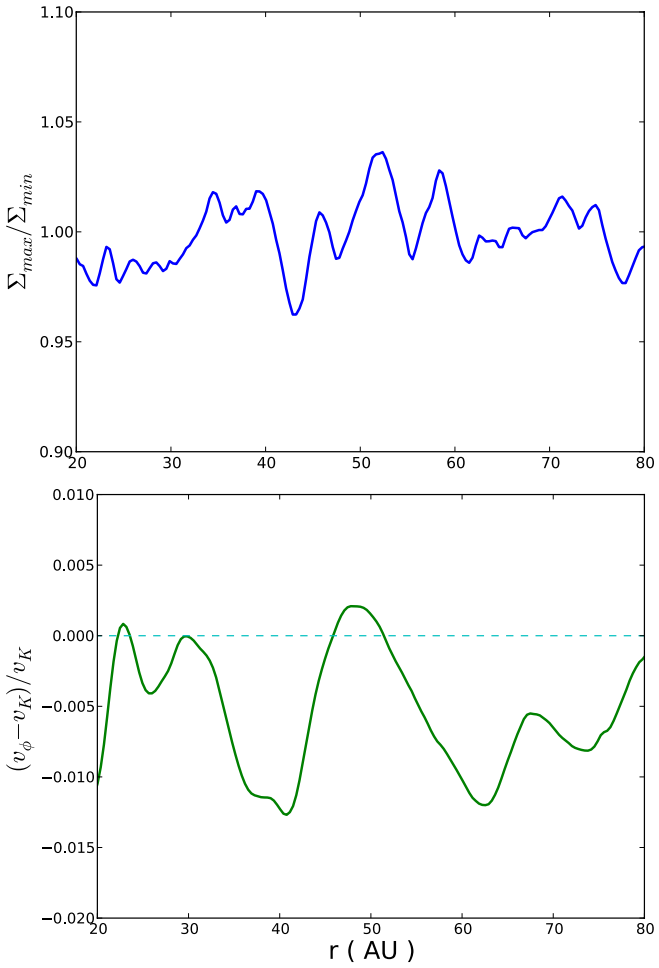

Figure 2.13: Top plot: Ratio of the surface density at two different azimuthal angles of of the disk from zonal flows simulation of Uribe et al. (2011). The azimuthal angles are chosen such that for a specific radius, the amplitude of the pressure bump has a maximum $\Sigma_{\max}$, and a minimum $\Sigma_{\min}$. Bottom plot: Azimuthal velocity with respect to the Keplerian velocity for the azimuthal and time-averaged surface density of the midplane.

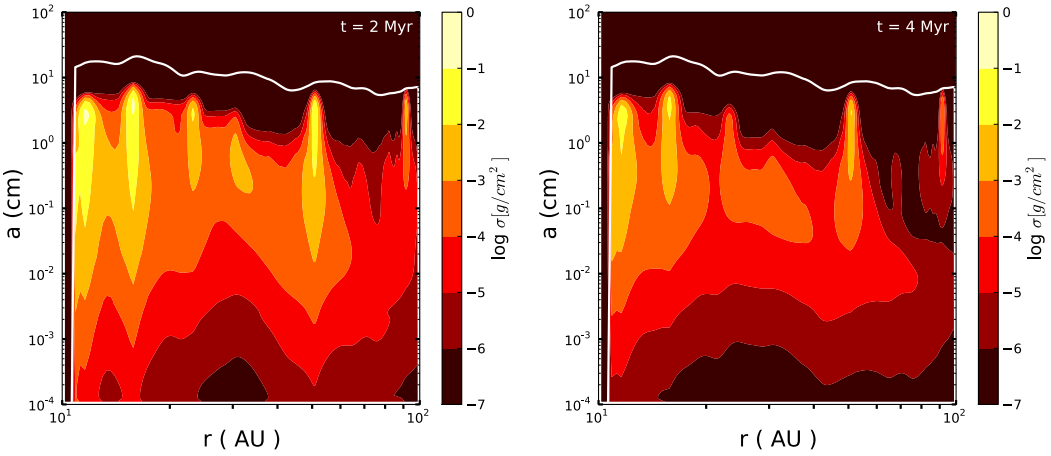

Figure 2.14: Vertically integrated dust density distribution after 2 Myr and 4 Myr of dust evolution; taking the azimuthal and time-average profile of the gas surface density in the midplane from the MHD simulations (see Uribe et al. 2011, figure 3) without a planet. The solid white line shows the particle size corresponding to a Stokes number of unity, which has the same shape as the density profile.

been performed for a higher resolution (see e.g. Johansen et al. 2009) and a more global setup (Flock et al. 2011).

In magnetorotational instability, "zonal flows" are excited as a result of the energy transportation from the MRI unstable medium scales, to the largest scales causing an inverse cascade of magnetic energy, and creating a large-scale variation in the Maxwell stress (Johansen et al. 2009).

Different 3D MHD simulations have shown that in the presence of zonal flows, pressure bumps can appear when there are drops in magnetic pressure throughout the disk (Johansen et al. 2009; Dzyurkevich et al. 2010; Uribe et al. 2011). Nevertheless, in the simulations of yet higher resolution performed by Flock et al. (2011), pressure bumps are not formed. There is no conclusion about how and whether these pressure bumps can be created via zonal flows.

An alternative for the origin of the pressure bumps produced by MRI is the change in the degree of ionization. The disk becomes MRI active when the degree of ionization is sufficiently high for the magnetic field to be strongly coupled to the gas. Variable degrees of ionization in the disk could cause local changes in the magnetic stress, which could induce structures in the density and pressure.

The question we now wish to answer is are the pressure bumps generated by zonal flows of MRI-turbulence, strong enough to trap the dust in a similar

way to the models of Sect. 2.2? To find this out, we consider the 3D MHD simulations of MRI-turbulent protoplanetary disks by Uribe et al. (2011). These models have a resolution of $(N_r, N_\theta, N_\phi) = (256, 128, 256)$. We note that the MRI dynamical timescale is around one orbital period (at one AU), while the dust growth timescale is longer than 100 orbital periods. It is currently infeasible to study the dust growth process self-consistently in the full time-dependent 3D model. This would require the development of a MHD model tens to hundreds of times longer than currently achievable. Hence, the strategy is to find first a quasi-steady state of the gas surface density from MRI evolution, in which structures in the pressure survive the entire simulation (around 1000 inner disk orbits). Afterwards, to do the coagulation/fragmentation simulation of the dust in 1D taking the gas surface density for a specific azimuthal angle in the midplane from the results from MHD simulations.

Top plot of Fig. 2.13 shows the ratio of the time-averaged surface density at two different azimuthal angles where the amplitude of a pressure bump reaches a maximum and a minimum at two specific radii. We note, that the variations in the azimuthal angle are very uniform, around $\sim 5\%$. This is why we wish to work with the azimuthally averaged density.

For our simulations, we assumed that the pressure structure survives and is stable on dust growth and evolution timescales. The lifetime of these structures as determined by global disk simulations is still uncertain, but it has been found to be on the order of 10-100 local orbits (at the radial position of the bump) (Johansen et al. 2009; Uribe et al. 2011). It is still an open question whether this behavior can be directly re-scaled to apply to the outer parts of the disk and in any case, the structures should be eventually diffused on turbulent diffusion timescales. In the future, the continuous generation and evolution of these structures should be implemented alongside the dust evolution. However, for lack of a better model of this time-dependence at this stage, we assumed these structures to be static.

Since these MHD simulations use a radial domain where $r \in [1; 10]$, we rescaled this grid logarithmically, such that the gas surface density was taken from 10AU to 100AU, and scaled the surface density such that the total disk mass was $0.05 M_\odot$ (see Fig. 2.1-left plot (solid-line)). Comparing the gas surface density obtained from MHD simulations with the assumed perturbed density Σ' (Eq. 2.1), we could see that the amplitude of the surface density perturbation from zonal flows was around 25% and comparable with the amplitude of 30% of Σ'. The widths of the bumps from Uribe et al. (2011) are not uniform, but our assumption of $f = 1$ agrees well with some of those bumps.

The bottom plot of Fig. 2.13 shows the azimuthal velocity with respect

to the Keplerian velocity for the azimuthal and time-averaged surface density of the midplane. We note that the azimuthal velocity exceeds the Keplerian velocity for some regions of the disk. This implies that for these regions, the presence of zonal flows allows us to have a positive pressure gradient leaving dust particles to move outwards. Therefore, the peaks of the pressure bumps created by zonal flows may be regions where dust particles can reach millimeter sizes.

Figure 2.14 shows the vertically integrated dust density distribution after 2 Myr and 4 Myr of dust evolution (using the model of Birnstiel et al. (2010a)). We note that at that time of evolution the pressure bumps caused by zonal flows are able to retain mm and cm sized particles in the outer regions of the disk. This is why a high mass disk was considered in this case, in order to simulate large grains. Around 50-60AU, there is clearly a region with a high vertically integrated dust density distribution for mm and cm-sized particles.We note that the peak around 100AU is a result of the boundary condition.

2.4 Conclusions

Theoretical models of dust evolution in protoplanetary disks show that the growth from sub-micron sized particles to larger objects is prevented basically by two phenomena: radial drift and fragmentation. Nevertheless, infrared and radio observations show that millimeter-sized particles can survive under those circumstances in the outer regions of the disks. Therefore, various theoretical efforts have focused on explaining the survival of those bodies.

We have taken into account the strong inhomogeneities expected to persist in the gas density profile e.g. zonal flows, and used the coagulation/ fragmentation and disk-structure models of Birnstiel et al. (2010a), to investigate how the presence of pressure bumps can cause a reduction in the radial drift, allowing the existence of millimeter-sized grains in agreement with observations. In this work, we assumed a sinusoidal function for the gas surface density to simulate pressure bumps. The amplitude and wavelength disturbances were chosen by considering the necessary conditions to have outward angular momentum transport in an α-turbulent type disk, outward radial drift of dust, and reasonable values compared to the predictions of studies of zonal flows (Uribe et al. 2011).

The results presented here suggest tha pressure bumps with a width of the order of the disk scale-height and an amplitude of 30% of the gas surface density of the disk, provide the necessary physical conditions for the survival of larger grains in a disk with properties summarized in Table 2.1. Com-

parisons between the observed fluxes of the Taurus, Ophiucus, and Orion Nebula Cluster star-forming regions with the results of the models ratify that the effect of the radial drift decreases allowing particles to grow. Figure 2.8 shows how models with these kind of disturbances reproduce more closely the mm-observations than models with full or without radial drift.

In addition, we have presented a comparison between the bumpy density profile assumed in this work and 3D MHD models of zonal flows that can cause long lived bumps in protoplanetary disks. We have shown that the pressure bumps produced by the zonal flows of Uribe et al. (2011) agree with the amplitudes and wavelengths used in this work. Therefore, considering these bumps, the survival of dust particles is possible in the outer regions after some Myr.

The simulated images using the CASA ALMA simulator (version 3.2.0) show that, with a different antenna configuration of the final ALMA stage, the ring structures, because of the pressure bumps, should be detectable. Future ALMA observations will have an important impact on our understanding the first stages of planet formation and will be very important in investigating if the grain growth and retetion can be explained by the presence of these kind of inhomogeneities in the gas density profile.

Chapter 3

Explaining millimeter-sized particles in Brown Dwarfs disk

Based on the paper by ***Pinilla P.****, Birnstiel, T., Benisty, M., Ricci, L., Natta, A., Dullemond, C. P., Dominik, C, Testi, L. accepted for publication in A&A*

Since the first confirmed discovery of Brown Dwarfs (BD) *Teide 1* (Rebolo et al. 1995) and *Gliese 229B* (Nakajima et al. 1995) both in 1995, several hundred of BDs have been identified and various efforts have been focused on understanding these objects that are considered to be an intermediate step between planets and stars. Observations of BD show near infrared excess emission (e.g. Muench et al. 2001; Liu et al. 2003) that reveals the existence of material around young BD. Moreover, typical fluxes measured with millimeter observations (e.g Klein et al. 2003; Scholz et al. 2006; Joergens et al. 2012) are in most of the cases lower than few mJy at 1 mm, implying that these circumstellar disks have masses of few $M_{\rm Jup}$ or even lower. Determining whether such kind of low mass disks can be the scene of the formation of planetesimals or even planets is still a subject of discussion.

Observationally, some aspects of disks around BD are different from the ones around T-Tauri and Herbig Ae/Be stars such as: lower accretion rate ($\sim 10^{-12}\ M_{\odot}\ yr^{-1}$, Herczeg et al. 2009), flat tendency for the disk geometry inferred from *Spitzer* observations and SED modeling (e.g. Apai et al. 2005; Allers et al. 2006; Guieu et al. 2007; Scholz et al. 2007; Morrow et al. 2008; Pascucci et al. 2009; Szűcs et al. 2010) and longer disk lifetime for low-mass disks (Carpenter et al. 2006; Riaz et al. 2012; Harvey et al. 2012b).

To study dust growth in protoplanetary disks, different mechanisms should be taken into account as e.g. turbulent mixing, settling, aerodynamical drag

with the gas, collision rates, fragmentation, etc. Essentially, when dust particles are small, they are well coupled to the gas, they move along with it and they grow as a consequence of surface forces. However, when particles get bigger, they start to decouple from the gas, relative velocities between particles increase leading to fragmentation collisions (Weidenschilling 1977; Brauer et al. 2008). In addition, before any meter-size object can be formed at Earth-Sun distances, dust drifts towards the central star due to the sub-Keplerian velocity of the gas. Millimeter (mm) grains experience the same rapid inward migration in the outer regions of the disks, even though mm-size particles have been observed in those regions of protoplanetary disks (e.g. Wilner et al. 2000; Natta et al. 2004; Rodmann et al. 2006; Ricci et al. 2010a,b, 2011; Ubach et al. 2012). The presence of local pressure maxima in disks have been proposed as a solution of this rapid inward drift (Klahr & Henning 1997; Johansen et al. 2009; Pinilla et al. 2012a).

Birnstiel et al. (2010b) showed that under typical T-Tauri parameters, neglecting radial drift and considering different parameters for the disk as e.g. turbulence, particles could reach millimeter sizes, meaning that the spectral index $\alpha_{1-3\mathrm{mm}}$ can have low values. Their models predict that for a disk mass lower than 5 M_{Jup}, such as the one of a BD, $\alpha_{1-3\mathrm{mm}}$ would be close to 3. However, recent millimeter-observations confirmed low values $\alpha_{1-3\mathrm{mm}}$ for two BD disks (Ricci et al. 2012; Ricci et al. 2013), with $\alpha_{1-3\mathrm{mm}} \approx 2.3$. In addition, as we will show later, the radial drift and fragmentation barriers are different for particles in disks around BD than for the ones around more massive and luminous stars. Radial drift indeed has a stronger influence for particles in BD disks and as a consequence any mechanism in a disk that may allow to reduce the inward migration of grains, has to be more extreme in BD disks, to lead to an effective trapping of particles. Explaining how the first pebbles are formed from interstellar dust in BD disks is therefore a very intriguing topic.

The purpose of this chapter is to investigate whether the dust growth models that were successful for T-Tauri disks are, when applied to BD disks, consistent with a short set of observations at millimeter-wavelengths (two measurements from recent ALMA and CARMA observations). As we mentioned before, infrared studies have on the other hand focused on large survey giving interesting trends such as flatter geometry. However, we do not aim to reproduce such trends, since infrared observations do not bring strong constraints on the dust evolution models (other than those that have already been studied by e.g. Mulders & Dominik (2012) or Szűcs et al. (2010)). Although the inclusion of the vertical structure calculation would be a step further in our model, this would depend on a number of additional properties, such as the vertical profile of turbulence, which is still a matter of

debate (Lyra et al. 2008; Simon et al. 2013).

For this work, dust coagulation/fragmentation models are considered in two main cases: first, the extreme case of setting the radial drift to zero and second, taking radial drift into account with strong inhomogeneities in the gas surface density that mimic long-lived pressure bumps. In both cases, different disk parameters are considered, to analyze which scenarios are the best incubators of the first pebbles found in BD disks with millimeter-observations. In Sect. 3.1, we describe the drift and fragmentation barriers for the specific case of BD disks and the physical parameters of the dust coagulation/fragmentation model. Numerical results, observational perspectives and comparison with current mm-observations are presented in Sect 3.2. A summary of the results with the corresponding discussion of this work are summarized in Sect. 3.3. Finally, the main conclusion of this chapter is in Sect. 3.4.

3.1 Dust evolution model, drift and fragmentation barriers in BD disks

The interaction between the gas and the dust is fundamental to understand how the particles evolve within the protoplanetary disk. When particles are well coupled to the gas, the dust relative velocities are mainly due to Brownian motion and settling to the midplane. Considering these two sources for the velocities, particles stick by van der Waals forces and collisional growth is very efficient, producing for typical T-Tauri disks, mm-size grains in the outer regions ($\gtrsim$ 50 AU) in timescales of $\sim 10^5$ years (Birnstiel et al. 2010a). Unfortunately, when particles grow, the relative velocities substantially increase due to turbulent motion and radial drift, the collision energies are therefore high enough to cause fragmentation, as is shown was experimentally shown by Blum & Wurm (2008). From the theoretical point of view, stellar and disk properties strongly influence these first steps of planet formation, meaning that effects such as the usual inward migration of dust grains may vary for BD disks. In this section, we first explain the main characteristics of the numerical model for the dust evolution, followed by an explanation of the drift and fragmentation barriers in BD disks and finally we describe the set-up for the numerical simulations that are considered in this work.

3.1.1 Dust evolution model

For the dust evolution, we use the coagulation/fragmentation model explained by Birnstiel et al. (2010a). The dust evolution is described by the

advection-diffusion differential equation of the dust surface density Σ_d, which for a single dust size, can be written in cylindrical coordinates as:

$$\frac{\partial \Sigma_d}{\partial t} + \frac{1}{r}\frac{\partial}{\partial r}\left(r\Sigma_d u_{\rm r,d}\right) - \frac{1}{r}\frac{\partial}{\partial r}\left(r\Sigma_g D_d \frac{\partial}{\partial r}\left[\frac{\Sigma_d}{\Sigma_g}\right]\right) = 0, \tag{3.1}$$

where D_d is the dust diffusivity and Σ_g is the gas surface density. Due to the fact that the timescales for gas viscous evolution are longer than the dust growth timescales, we consider that for the dust evolution models, the gas surface density remains constant with time. This equation is solved for each size using the flux-conserving donor-cell scheme (see Birnstiel et al. 2010a, Appendix A). The radial velocity of the dust $u_{\rm r,d}$ has two contributions: the first one $u_{\rm drag}$, due to the drag with the gas, that depends on the radial gas velocity $u_{\rm r,g}$ and on the size of the particles; and the second one due to radial drift $u_{\rm drift}$, which is proportional to the radial pressure gradient $\partial_r P$, such that:

$$u_{\rm r,d} = \frac{u_{\rm r,g}}{1+{\rm St}^2} + \frac{1}{{\rm St}^{-1}+{\rm St}}\frac{\partial_r P}{\rho_g \Omega}, \tag{3.2}$$

where the coupling constant St -the Stokes number- is defined as the ratio between the largest eddy turn-over time ($1/\Omega$, with $\Omega = \sqrt{G\ M_\star\ r^{-3}}$) and the stopping time of the particle within the gas. In the Epstein regime, where the ratio between the mean free path of the gas molecules $\lambda_{\rm mfp}$ and the sizes of the particles a is $\lambda_{\rm mfp}/a \geq 4/9$, St is defined at the disk midplane as:

$${\rm St} = \frac{a\rho_s}{\Sigma_g}\frac{\pi}{2}, \tag{3.3}$$

with ρ_s being the volume density of a dust grain, usually of the order of ~ 1 g cm^3.

In addition, the turbulent gas viscosity is considered as $\nu = \alpha_{\rm turb}\ c_s^2\ \Omega^{-1}$ (Shakura & Sunyaev 1973), where c_s is the isothermal sound speed, which is given by:

$$c_s^2 = \frac{k_B T(r)}{\mu m_p}, \tag{3.4}$$

k_B being the Boltzman constant, m_p the proton mass and μ the mean molecular mass. Magnetorotational instability (MRI) is the most likely source of turbulence in disks (e.g Johansen & Klahr 2005). MRI essentially depends on the disk temperature and penetration of cosmic, X- and UV-rays to the midplane. The dust diffusivity in Eq. 3.1 can be defined in terms of St when the gas diffusivity is considered to be the turbulent gas viscosity ν (Youdin & Lithwick 2007), hence:

$$D_d = \frac{\nu}{1 + \mathrm{St}^2}. \tag{3.5}$$

The Stokes number St, describes how well the particles are coupled to the gas. When $\mathrm{St} \ll 1$, the first term dominates in Eq 3.2 i.e. u_{drag}, and as a result these particles move along with the gas, meaning that they have sub-Keplerian velocities. When the particle size increases, the second term i.e. u_{drift} starts to dominate and reach the maximum value when $\mathrm{St} = 1$, and as a consequence these are the particles that strongest react to the sub-Keplerian velocity of the gas. The bodies with $\mathrm{St} \gg 1$ move with the own velocity i.e. Keplerian speed.

In addition, dust particles grow, fragment and crater depending on the relative velocities between them. For this the Smoluchowski coagulation equation (Smoluchowski 1916) is solved for the dust grain distribution $n(a, r, z)$ (see Birnstiel et al. 2010a, Eq. 35 and Eq. 36), considering three different physical processes: coagulation, fragmentation and erosion. For the relative velocities, we take Brownian motion, settling, turbulent motion (Ormel & Cuzzi 2007) and drift velocities in the azimuthal and radial direction. The fragmentation velocities v_f are estimated based on laboratory experiments and theoretical work of collisions, which are of the order of few m s^{-1} for silicates (Blum & Wurm 2008) and several m s^{-1} for ices (e .g. Wada et al. 2009, 2011). To describe the dust grain distribution, we usually refer to the vertically integrated dust surface density distribution per logarithmic bin, which is given by:

$$\sigma(r, a) = \int_{-\infty}^{\infty} n(r, z, a) \cdot m \cdot a dz \tag{3.6}$$

where m is the mass of a single particle of size a. Therefore the total dust surface density can be written as:

$$\Sigma_d(r) = \int_0^{\infty} \sigma(r, a) d \ln a. \tag{3.7}$$

3.1.2 High radial drift and fragmentation in BD disks

In a protoplanetary disk, large bodies do not feel pressure and move with Keplerian speed, while the gas is slightly sub-Keplerian. As a result, particles that have grown to a size that they start to decouple from the gas i.e. $\mathrm{St} \approx 1$, feel a strong headwind, losing angular momentum and moving inwards. Solving the radial Navier-Stokes equation, the azimuthal velocity of the gas is given by (Nakagawa et al. 1986):

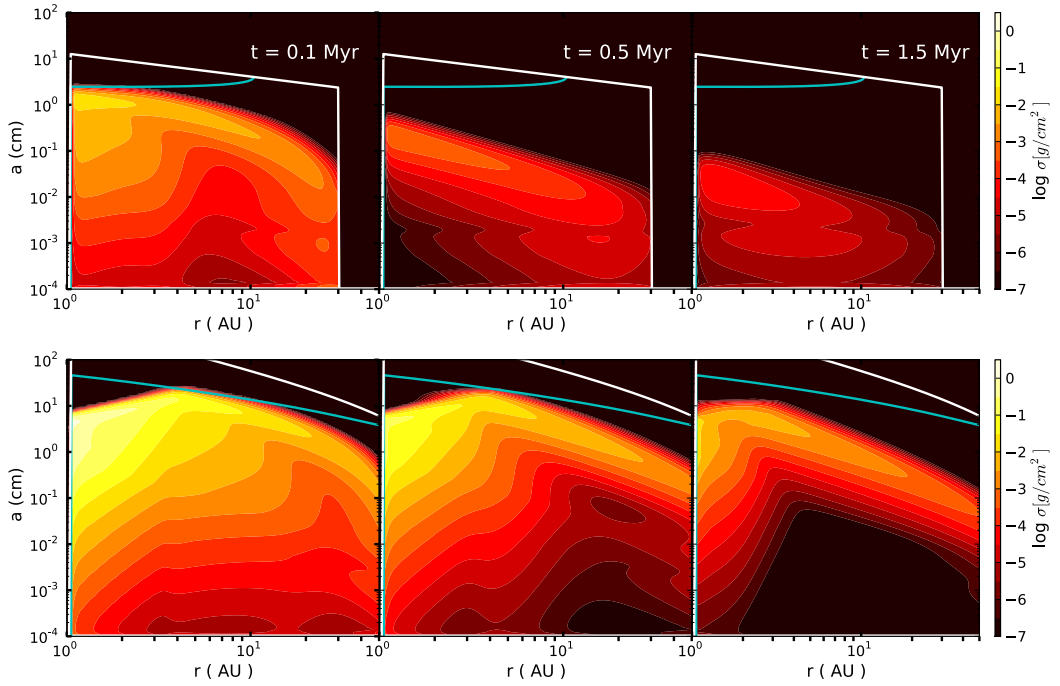

Figure 3.1: Vertically integrated dust density distribution (Eq. 3.6) after different times of evolution and including radial drift. *Top panels:* Case of the BD disk ρ-Oph102 parameters ($M_{BD} = 0.05\ M_{\odot}$, $L_{BD} = 0.03\ L_{\odot}$ and $T_{BD} = 2880\ K$) and $R_{\rm out} = 30$ AU, $\Sigma = \Sigma_0\ r^{-0.5}$, $M_{\rm disk} = 2\ M_{\rm Jup}$, $v_f = 10\ m\ s^{-1}$ and $\alpha_{\rm turb} = 10^{-3}$. The solid white line represents the particle size corresponding to St = 1 (Eq. 3.3) and reflects the shape of the gas density. The cyan line corresponds to the maximum size that particles can reach given a fragmentation velocity v_f. *Bottom panels:* Similar model parameters, but considering a T-Tauri disks as in Chapter 1.

$$u_{\phi,\mathrm{g}} = u_k \left(1 - \eta\right), \tag{3.8}$$

where u_k is the Keplerian speed and

$$\eta = -\frac{1}{2\rho_g(r,z) r \Omega^2} \frac{dP(r)}{dr}, \tag{3.9}$$

with $\rho_g(r,z)$ the gas density, such that the gas surface density is given by $\Sigma_g = \int_{\infty}^{\infty} \rho_g(r,z) dz$. For an ideal gas, the pressure $P(r)$ is defined as:

$$P(r) = c_s^2 \rho_g(r,z), \tag{3.10}$$

and therefore

$$\eta = -\frac{c_s^2}{2u_k} \left(\frac{d\ln\rho}{d\ln r} + \frac{d\ln c_s^2}{d\ln r} \right), \tag{3.11}$$

where the term in parenthesis depends only on the exponents that characterize the power-law gas density and temperature radial profiles in a flared disk. For the temperature, $T(r)$ can be approximated by (Kenyon & Hartmann 1987):

$$T(r) = T_\star \left(\frac{R_\star}{r} \right)^{1/2} \alpha_{\mathrm{inc}}^{1/4} \propto \frac{L_\star^{1/4}}{\sqrt{r}}, \tag{3.12}$$

when $r/R_\star \gtrsim 10^2$. α_{inc} is the angle between the incident radiation and the local disk surface. For the last proportionality of Eq. 3.12 the small dependence of α_{inc} with $R_\star$ is neglected. Considering Eq. 3.12 for the disk temperature and assuming a simple power-law function for the gas density profile, the difference between the orbital gas velocity and the Keplerian speed scales as (independently of the radial location r):

$$u_{\phi,\mathrm{g}} - u_k = \frac{c_s^2}{2u_k} \left(\frac{d\ln\rho}{d\ln r} + \frac{d\ln c_s^2}{d\ln r} \right) \propto \frac{T(r)}{\sqrt{M_\star r^{-1}}} \propto \frac{L_\star^{1/4}}{\sqrt{M_\star}}. \tag{3.13}$$

This difference determines how much angular momentum the particles lose and as a consequence how fast they drift to the central star. Taken Eq. 3.2 for the dust radial velocity, and considering grains with $\mathrm{St} \gtrsim 1$, the drag term (first term of Eq. 3.2) can be neglected and $u_{\mathrm{r,d}}$ can be written in terms of the difference $u_{\phi,\mathrm{g}} - u_k$ as:

$$u_{\mathrm{r,d}} = 2 \frac{u_{\phi,\mathrm{g}} - u_k}{\mathrm{St}^{-1} + \mathrm{St}}. \tag{3.14}$$

For comparison, taking the parameters of the BD know as $\rho-$Oph 102 (Ricci et al. 2012) and comparing them with a young solar type star, i.e. $M_{\rho-\mathrm{Oph102}} = 0.05 \times M_{\mathrm{sun}}$ and $L_{\rho-\mathrm{Oph102}} = 0.03 \times L_{\mathrm{sun}}$, this leads to:

$$(u_{\phi,\mathrm{g}} - u_k)_{\rho-\mathrm{Oph102}} \approx 2\,(u_{\phi,\mathrm{g}} - u_k)_{\mathrm{sun}}\,. \tag{3.15}$$

The fact that the radial drift is higher for BD disks than for Sun-like disks also implies that destructive collisions due to radial drift are more likely because it contributes to increase the relative velocities between the particles. Therefore fragmentation and rapid inward drift are major problems for particles in BD disks.

In addition, the maximum turbulent relative velocity of particles with a given Stokes number is given by (Ormel & Cuzzi 2007):

$$\Delta u^2_{\mathrm{max}} \simeq \frac{3\ \alpha_{\mathrm{turb}}}{\mathrm{St} + \mathrm{St}^{-1}} c_s^2. \tag{3.16}$$

When the radial drift is set to zero, the maximum size of particles a_{max} is calculated when the turbulent relative velocities (Eq. 3.16) are equal to the fragmentation velocities v_f. For particles with $\mathrm{St} \lesssim 1$, a_{max} is approximately given by,

$$a_{\mathrm{max}} \approx \frac{2\Sigma_g}{3\pi\alpha_{\mathrm{turb}}\rho_s} \frac{v_f^2}{c_s^2}. \tag{3.17}$$

This implies that considering only turbulent velocities, a_{max} will depend on disk parameters as α_{turb}, Σ_g, and $T(r)$, which strongly varies between BD and T-Tauri disks. Whether turbulence or radial drift is the cause for destructive collisions for the dust within the disk, fragmentation would occur differently for BD disks as we will discuss in the following sections.

As a general illustration of this problem in BD disks, the top panels of Fig. 3.1 shows the vertically integrated dust density distribution (Eq. 3.6) after different times of evolution, including radial drift and using the dust evolution model described in Sect. 3.1.1. For this case, taking the parameters of the case of ρ-Oph 102 ($M_{BD} = 0.05\ M_{\odot}$, $L_{BD} = 0.03\ L_{\odot}$ and $T_{BD} = 2880\ K$), a truncated power law is taken for the gas density profile with $\Sigma = \Sigma_0\ r^{-0.5}$ and $r \in (1, 30)$ AU such that the mass of the disk is $M_{\mathrm{disk}} = 2\ M_{\mathrm{Jup}}$. The maximum size that particles can reach is represented by the solid cyan line, which is computed considering the fragmentation velocity as $v_f = 10\ m\ s^{-1}$ and the turbulence parameter as $\alpha_{\mathrm{turb}} = 10^{-3}$. The solid white line corresponds to $\mathrm{St} = 1$, which reflects the shape of the gas surface density base on Eq. 3.3 and particles that feel the strongest radial drift. The dust particles initially grow in the disk allowing to have mm size

grains in the outer regions ($r \gtrsim 10$ AU) after 0.1 Myr of evolution (left-top panel of Fig. 3.1). However, when particles grow to sizes close to St $\sim$ 1, turbulence and radial drift lead to fragmentation and inward migration of particles, and only in 0.5 Myr of evolution (middle-top panel of Fig. 3.1), the outer region is empty of mm-grains, contrary to the case of T-Tauri disks (bottom panels of Fig. 3.1), in which case the drift effect is less effective (Eq. 3.15), but it still happens. This scenario does not change significantly with time (right panels of Fig. 3.1), however the inner region ($r \lesssim 10$ AU) is even more depleted of mm grains, since they continue fragmenting and drifting towards the star, leading to have a dust poor disk after 1.5 Myr. As a result, explaining how micron-size dust grows to pebbles and how those are retained in the outer regions of BD disks is very challenging.

In addition, if perfect sticking and micron-sized compact particles are considered to be formed, the mean growth time of monomers with mass m at a fixed distance from the star is (Brauer et al. 2008; Okuzumi et al. 2011):

$$\tau_{\rm grow} = \left(\frac{1}{m}\frac{dm}{dt}\right)^{-1}, \tag{3.18}$$

where $dm/dt = \rho_d \sigma_{\rm coll} \Delta v$, with ρ_d is the dust density, $\sigma_{\rm coll}$ the collision cross section and Δv the collision velocity. For a narrow size distribution, perfect mixing and settling assumed in the Epstein regime, a given dust-to-gas ratio, the growth timescale is proportional to:

$$\tau_{\rm grow} \propto \frac{\Sigma_g}{\Sigma_d}\Omega^{-1}, \tag{3.19}$$

with Σ_d as the dust surface density. A comparison of the growth timescale in disks of BD and T-Tauri disks can be done considering, for example, regions of similar temperature. Following Mulders & Dominik (2012), we re-scale the distances with the stellar luminosity as well as the Keplerian frequency, to obtain

$$\tau^{\rm BD}_{\rm grow} \propto \frac{\Sigma_g}{\Sigma_d}\Omega^{-1}_{\rm BD} = \tau^{\rm TT}_{\rm grow}\sqrt{\frac{L_{\rm BD}}{L_\star}}, \tag{3.20}$$

where $\tau^{\rm BD}_{\rm grow}$ and $\tau^{\rm TT}_{\rm grow}$ correspond to the growth timescales in BD and T-Tauri disks respectively. This implies that, for micron-size particles and considering for simplicity only settling motion, the mean collision time $\tau_{\rm grow}$ is generally shorter for BD than for T-Tauri disks. As an illustration, if we again take the BD ρ - Oph 102, the growth timescale due to settling is approximately one order of magnitude shorter for dust particles around this BD than for particles in a Sun-like disk. As a consequence of the result that settling and

Table 3.1: Model parameters

Parameter	Values
$M_{BD}[M_\odot]$	0.05
$L_{BD}[L_\odot]$	0.03
T_{BD} [K]	2880
ρ_s [g/cm^3]	1.2
$M_{\rm disk}[M_{\rm Jup}]$	2.0
$R_{\rm in}$[AU]	1.0
$R_{\rm out}$[AU]	$\{15, 30, 60, 100\}$
$\alpha_{\rm turb}$	$\{10^{-5}, 10^{-4}, 10^{-3}\}$
v_f [m/s]	$\{10, 30\}$
A	$\{0.4, 0.6\}$
f	1

radial drift occur faster in BD disks, the very early stages of dust growth, when particles just stick and grow due to molecular interactions, is more efficient at the location of a given temperature in BD disks than in T-Tauri disks.

Based on the low spectral indices ($\alpha_{1-3\rm mm} < 3$) measure with recent ALMA-Cycle 0-observations at 3.2 mm and 0.89 mm of the young BD $\rho-$Oph 102 (Ricci et al. 2012) and CARMA observations of the BD disk 2M0444+2512 at 3 mm (Ricci et al. 2013) and 0.850 mm (Bouy et al. 2008), we aim to explain how mm-grains can form and be retained in disks around BD. We focus this work in two parts: In the first part, we do not allow particles to drift, to study whether we can create mm-grains, considering only grain growth and fragmentation. In the second part, we aim to explain how to trap these grains in the outer regions of BD disks, when radial drift is included.

3.1.3 Set-up

For the simulations of this work, we consider two different scenarios. In the first case, no dust radial evolution i.e. the drag and drift terms in Eq. 3.2 are neglected. In the second case, we consider dust radial evolution with pressure bumps. For the gas density, we consider truncated power law functions $\Sigma_g = \Sigma_0\, r^{-p}$, with $p = \{0.0, 0.5, 1.0\}$ and Σ_0 is computed such that the mass of the disk is always $M_{\rm disk} = 2\ M_{\rm Jup}$. For the outer radius of the disk, four possibilities are taken: 15, 30, 60 and 100 AU, since the exact typical disk spatial extent is unknown (Luhman et al. 2007; Ricci et al. 2012).

The turbulence parameter $\alpha_{\rm turb}$ is taken to have values between $10^{-5} - 10^{-3}$. This parameter influences directly the maximum size of particles (Eq. 3.17), if turbulence is the cause of fragmentation. Mulders & Dominik (2012) inferred $\alpha_{\rm turb} \sim 10^{-4}$ from SED modeling, assuming a fixed grain size distribution and gas-to-dust ratio. The fragmentation velocities are assumed to be $v_f = \{10, 30\}$ m s^{-1}, which are the values expected for ices (Wada et al. 2009). For all the simulations, the dust-to-gas ratio is initially considered to be 1%, the initial size of the particles is taken to be 1 μm and the maximum size that particles can reach in the simulations is fixed to be 1 km, as for these sizes gravitational effects start to play a role, which are not included in the present dust evolution model.

When we consider pressure inhomogeneities, we assume the same prescription as in Pinilla et al. (2012a) to simulate long-lived pressure bumps, with the unperturbed density as a simple power law:

$$\Sigma'_g(r) = \Sigma_0 \; r^{-p} \left(1 + A \cos\left[2\pi \frac{r}{L(r)}\right]\right), \tag{3.21}$$

where the wavelength of the perturbation $L(r)$ is taken to be a factor f of the vertical disk scale-height $h(r)$ i.e. $L(r) = f \; h(r)$, with

$$h(r) = c_s \; \Omega^{-1} \propto \frac{L_\star^{1/8}}{\sqrt{M_\star}} \sqrt{r}. \tag{3.22}$$

Pinilla et al. (2012a) showed that under these assumptions, for T Tauri disks an amplitude of $\sim 30\%$, with a wavelength of one scale-height, is necessary to reduce the radial drift and keep the particles in the outer regions of the disk after several Myr. However, in Sect 3.1.2, we showed that radial drift effects are stronger for BD disks, independently of the distance from the star of the particles. In addition, since the wavelength of the perturbation is considered proportional to the disk scale-height $h(r)$, therefore at a given distance r, $L(r)$ would by definition be larger for BD than for T Tauri disks (Eq. 3.22). This implies, that for a given amplitude of the perturbed density, the pressure gradient would be lower in BD disks, making the trapping of particles even more difficult. We use a fixed bump width equal to one scale height i.e. $f = 1.0$, since the scale of turbulent structures from MRI are of the order of the scale height of the disk (Flock et al. 2011), and they may be the origin of pressure inhomogeneities in the disk. The amplitudes considered are therefore higher than for T Tauri disks and these are taken A=$\{0.4, 0.6\}$. All the stellar and disk parameters are summarized in Table 3.1.

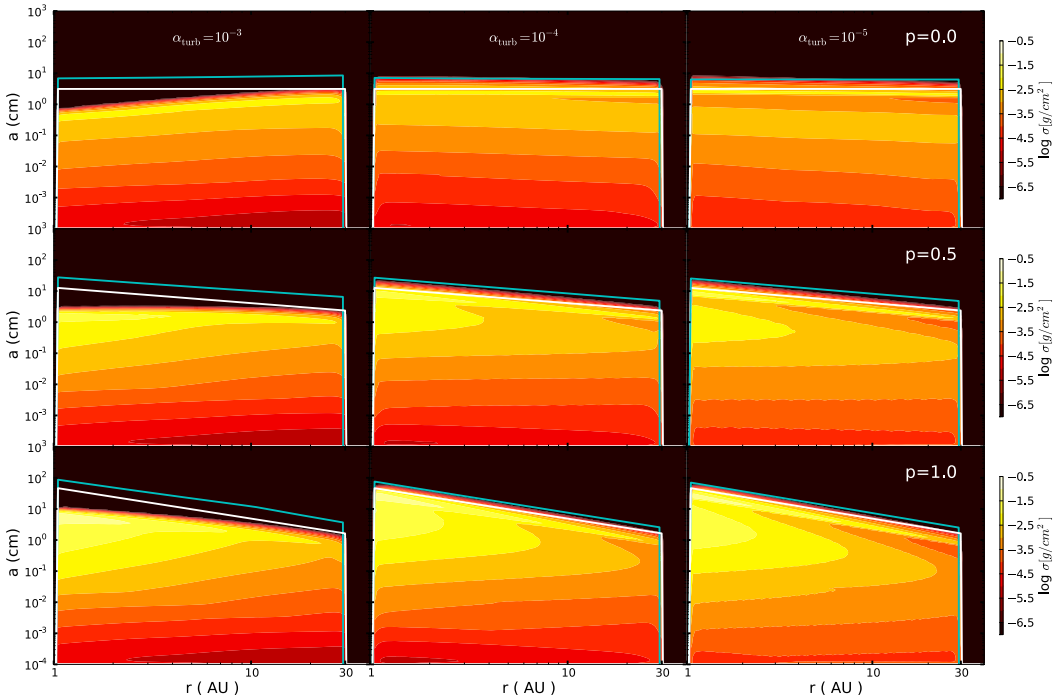

Figure 3.2: Vertically integrated dust density distribution after 1 Myr of evolution without including radial drift. Case of $R_{\rm out} = 30$ AU and $v_f = 10$ m s^{-1} and different values of the gas density slope $p = 0$ *(top panels)*, $p = 0.5$ *(middle panels)* and $p = 1.0$ *(bottom panels)*; with the turbulence parameter $\alpha_{\rm turb} = 10^{-3}$ *(left panels)*, $\alpha_{\rm turb} = 10^{-4}$ *(center panels)* and $\alpha_{\rm turb} = 10^{-5}$ *(right panels)*. The solid white line represents the particle size corresponding to St = 1 (Eq. 3.3) and reflects the shape of the gas density, while the cyan line represents the maximum size that particles can reach given a fragmentation velocity v_f.

3.2 Results

In this section, we present the results of the numerical simulations setting the radial drift to zero, followed by the case of non-zero radial drift and pressure bumps in the disk. For each case, the observational perspectives are also presented.

3.2.1 No radial drift

Dust density distribution

Figures 3.2 and 3.3 show the vertically integrated dust density distribution (Eq. 3.6) after 1 Myr of dust evolution when radial drift is set to zero, for the case of $R_{\rm out} = 30$ AU and two different values of the fragmentation velocity: 10 $m\ s^{-1}$ and 30 $m\ s^{-1}$ respectively. In each case, the three different values of the gas density slope p and the turbulence parameter $\alpha_{\rm turb}$ are plotted. For this case, the dust is considered to be in a steady state, therefore $u_{\rm drag}$ and $u_{\rm drift}$ are neglected in Eq. 3.2.

Effect of turbulence: when particles grow and reach sizes such that they are less coupled to the gas, the main sources of relative velocities are turbulent and azimuthal velocities, since radial drift velocities are set to zero. Due to the fact that the maximum turbulent relative velocities (Eq. 3.16) depends on $\alpha_{\rm turb}$ and the disk temperature is assumed to be very low in BD disks ($\sim$ 10K at 10 AU), fragmentation is not due to turbulent motions. Instead, it mainly happens because the azimuthal dust velocities $u_{d,\phi}$ are as high as the limit beyond which particles fragment (fragmentation velocity, v_f). The azimuthal drift velocity $u_{d,\phi}$ is given by (Birnstiel et al. 2010a)

$$u_{d,\phi} = \left| -\frac{\partial_r P}{\rho\Omega} \left(\frac{1}{1+{\rm St}^2} \right) \right|. \tag{3.23}$$

Hence, as we notice in Fig 3.2, the fragmentation limit and consequently $a_{\rm max}$ are independent of the $\alpha_{\rm turb}$ and for a given gas density slope, the maximum size that particles can reach is the same for each $\alpha_{\rm turb}$ and only depends on the gas density profile. On the other hand, we notice that the concentration of mm and cm-size grains is more evenly distributed in the whole disk for $\alpha_{\rm turb} = \{10^{-4}, 10^{-3}\}$ than for $\alpha_{\rm turb} = 10^{-5}$, for which they are mainly in the inner part of the disk.

The first remarkable difference of grain growth between T-Tauri and BD disks is that the turbulent mixing strength $\alpha_{\rm turb}$ does not play as important role for dust fragmentation in BD disks as it does for T-Tauri disks. Without radial drift, in T-Tauri disks, fragmentation mainly occurs because of

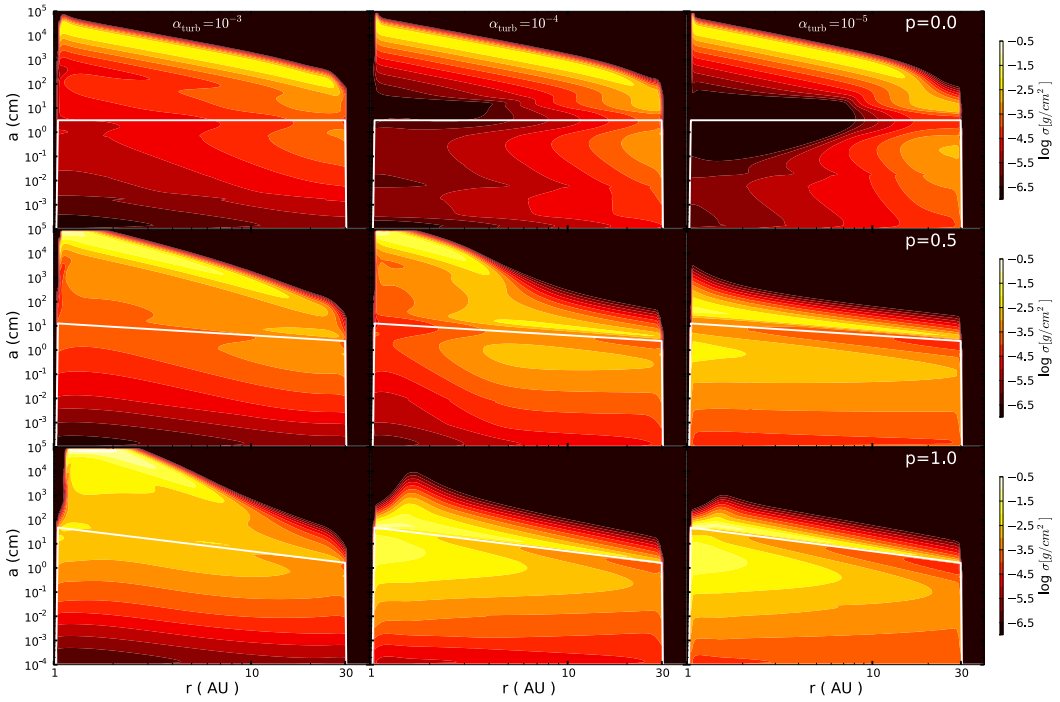

Figure 3.3: Vertically integrated dust density distribution after 1 Myr of evolution without including radial drift. Case of $R_{\rm out} = 30$ AU and $v_f = 30$ m s^{-1} and different values of the gas density slope $p = 0$ *(top panels)*, $p = 0.5$ *(middle panels)* and $p = 1.0$ *(bottom panels)*; with the turbulence parameter $\alpha_{\rm turb} = 10^{-3}$ *(left panels)*, $\alpha_{\rm turb} = 10^{-4}$ *(center panels)* and $\alpha_{\rm turb} = 10^{-5}$ *(right panels)*. The solid white line represents the particle size corresponding to St = 1 (Eq. 3.3) and reflects the shape of the gas density.

turbulent motion and the effect of different $\alpha_{\rm turb}$ values is significant (see e.g Birnstiel et al. 2010b, for the effect of turbulence in the spectral index), while for BD disks the azimuthal relative velocity dominates, which is independent of $\alpha_{\rm turb}$.

Effect of the gas density slope: For the same turbulence parameter and different gas density slope p, the dust density distribution changes (see Figs. 3.2 and 3.3). When $p = 1$ (steep surface density), large particles ($a > 1$ cm) are well coupled to the gas in the dense inner region, and grow to even larger sizes ($a \sim 50$ cm) before they fragment. Therefore, with $p = 1$ there is less concentration of mm-size particles in the region where the gas density is lower i.e. in the outer region of the disk ($r \gtrsim 10$ AU) than for $p = \{0.5, 1.0\}$.

Effect of the fragmentation velocity: when the velocity at which particles fragment increases to 30 $m\ s^{-1}$ (Fig. 3.3), grains can grow to very large sizes such that St > 1. Fragmentation does not occur and this implies that bodies that are no longer affected by gas ($a \gtrsim 1$ m) grow and even in some cases reach the maximum size of particles considered in these numerical simulations (~ 1 km). There is no replenishment of small particles and as a result the disk can be almost empty of small grains ($\lesssim 1$ cm). For example, when $p = 0$ and $\alpha_{\rm turb} = 10^{-5}$, most of the disk is made only of big grains ($a > 10$ cm). However, when p increases and the gas density is higher in inner regions, larger particles are coupled to the gas and can still be affected by gas turbulence. For this reason for the same $\alpha_{\rm turb} = 10^{-5}$ and $p = 1$, there is some mm-dust in the inner part.

As we discussed above, due to the low disk temperatures, destructive collisions due to turbulence are less likely in BD disks, and even more with these high fragmentation velocities considered for ices (such as $v_f = 30\ m\ s^{-1}$). With ices, the material properties varies, leading to fragmentation velocities of around $\sim 10 - 50\ m\ s^{-1}$ (Wada et al. 2009, 2011), however it is still a matter of debate if ices can have these high fragmentation velocities. Some scenarios produce disks with only large grains (Fig. 3.3), that may not allow to have a good agreement between these theoretical models and the recent sub-millimeter observations of disk around two BD. For this reason, we focus the following results to the case of $v_f = 10\ m\ s^{-1}$, where the fragmentation allows to have a constant replenishment of small particles.

Effect of the outer radius: When the outer radius of the disk decreases or increases, with the same $M_{\rm disk}$ and Σ_g profile, the same amount of dust is distributed in a smaller or larger region and the possibility of having cm-mm-size particles in the outer regions changes, effect that will be discuss in

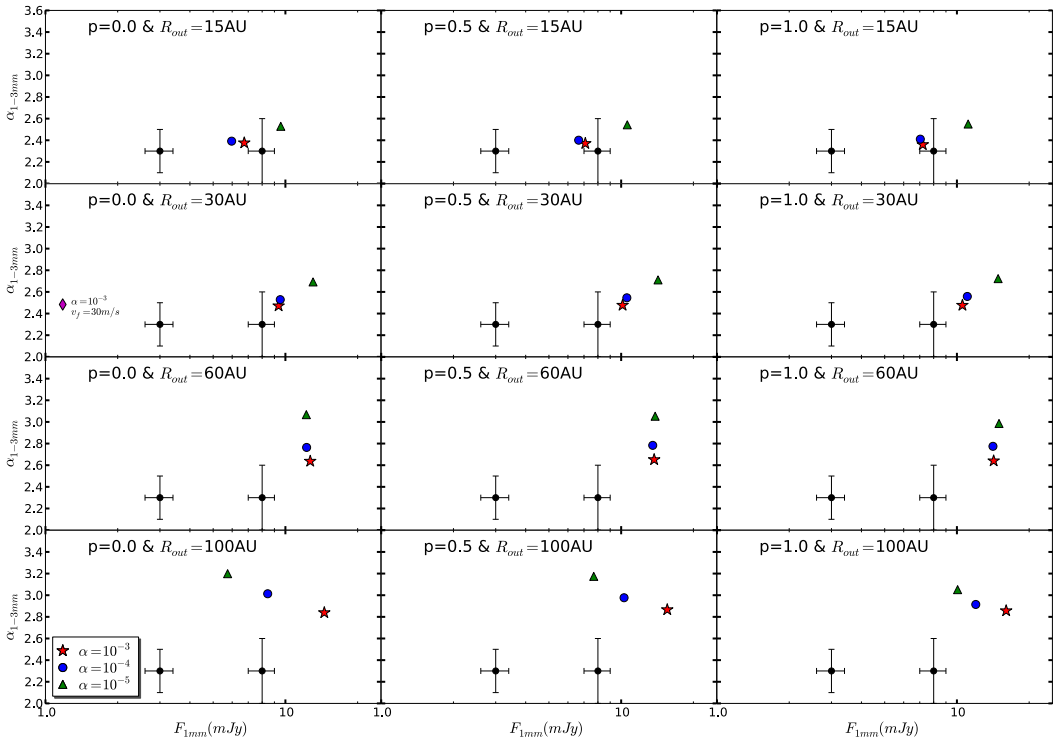

Figure 3.4: Predicted fluxes at 1 mm ($F_{1\mathrm{mm}}$) and the spectral index between 1 and 3 mm ($\alpha_{1-3\mathrm{mm}}$) after 1 Myr of dust evolution, without including radial drift, $v_f = 10\ m\ s^{-1}$ and for all the other parameters discussed in Sect. 3.1.3. Black dots with error bars are millimeter-observations of the young BD ρ-Oph 102 (Ricci et al. 2012) and 2M0444+2512 (Ricci et al. 2013)

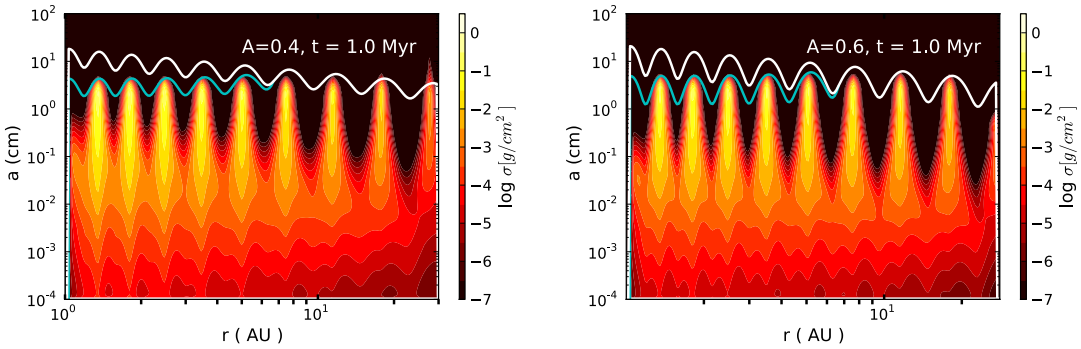

Figure 3.5: Vertically integrated dust density distribution after 5 Myr of evolution including radial drift and a bumpy gas surface density (Eq 3.21) with A = 0.4 *(left panel)* and A = 0.6 *(right panel)*. Case of $R_{\rm out} = 30$ AU, $v_f = 10$ m s^{-1}, $p = 0.5$ and $\alpha_{\rm turb} = 10^{-3}$. The solid white line represents the particle size corresponding to St = 1 (Eq. 3.3) and reflects the shape of the gas density, while the cy line corresponds to the fragmentation limit.

the following section.

Comparison with observations

In order to compare model predictions with disk fluxes of low mass disks, we take the dust distribution from the simulations after they reach almost a quasi-static state ~ 1 Myr. We calculate the opacities κ_ν for each grain size and at a given frequency ν. We use for simplicity optical constants for magnesium-iron silicates (Jaeger et al. 1994; Dorschner et al. 1995) from the Jena database[1] and following the Mie theory. Once the opacities are calculated, the optical depth τ_ν is computed as:

$$\tau_\nu = \frac{\sigma(r,a)\kappa_\nu}{\cos i}, \tag{3.24}$$

where i is the disk inclination which we take to be zero. The flux of the disk at a given frequency F_ν is therefore:

$$F_\nu = \frac{2\pi \cos i}{d^2} \int_{R_{\rm in}}^{R_{\rm out}} B_\nu(T(r))[1 - e^{-\tau_\nu}] r dr, \tag{3.25}$$

with d being the distance to the source, which is taken to be 140 pc as the young disks in Taurus and Ophiucus star forming regions. $B_\nu(T(r))$ is the Planck function for a given temperature profile $T(r)$. At mm wavelengths,

[1] http://www.astro.uni-jena.de/Laboratory/Database/databases.html

the flux is proportional to the dust mass in the outer region of the disks. Hence, the flux F_ν could be approximated as a power law $F_\nu \propto \nu^{\alpha_{\rm mm}}$, where the spectral index $\alpha_{\rm mm}$ gives information about the size of the grains and it is expected to be lower than 3 when the dust reaches mm sizes (Natta et al. 2007). Figure 3.4 shows the predicted fluxes at 1 mm ($F_{\rm 1mm}$) and the spectral index between 1 and 3 mm ($\alpha_{\rm 1-3mm}$) for $v_f = 10\ m\ s^{-1}$ and all other parameters considered in Sect. 3.1.3.

First of all, comparing $F_{\rm 1mm}$ and $\alpha_{\rm 1-3mm}$ for different $R_{\rm out}$, we notice how the spectral slope increases when the disk is more extended. This is a natural result of distributing initially the same amount of dust in a extended region, decreasing the possibility of having mm-size grains. The obtained fluxes are between $\sim$ 1-20 mJy for all cases. In addition, a single case (the only diamond-point of Fig. 3.4) where fragmentation does not happen is plotted, with $v_f = 30\ m\ s^{-1}$, $R_{\rm out} = 30$ AU and $p = 0.0$. It is possible to see that most of the dust in the disk have grown to large sizes (a $>$ 10 cm). When the particles have such a large size, they have very low opacities, which results in low millimeter fluxes. The predicted fluxes are very low (close to 1 mJy) compared with the other fluxes (see top-left panel of Fig. 3.3 and the corresponding diamond-point in the second left-panel from the top to the bottom of Fig. 3.4).

In general, when fragmentation still occurs, i.e. in the case of $v_f = 10\ m\ s^{-1}$, there is a weak dependence of the gas density slope p for the integrated flux, therefore we focus the subsequent results on the intermediate value i. e. $p = 0.5$. In most of the cases, the spectral slope and the flux are slightly sensitive to the turbulence parameter $\alpha_{\rm turb}$, and $\alpha_{\rm 1-3mm}$ increases for low turbulence. This is because the amount of mm-size grains that contributes to decrease the spectral index is less when $\alpha_{\rm turb}$ is low (Fig. 3.2 and Fig. 3.3), as it was discussed in Sect. 3.2.1.

Comparing with millimeter-observations (dot points with error bars in Fig 3.4) of two BD disks (2M0444+2512 and ρ Oph 102), it is important to notice that when radial drift is set to zero, it is possible to have a good match between the predicted and the observed values of $F_{\rm 1mm}$ and $\alpha_{\rm 1-3mm}$ for the brightest BD disk and, in particular for the case of $R_{\rm out} = 15$ AU. The errors bars come from the the optical depth uncertainties for different grain composition (Beckwith et al. 1990). When the extension of the disk increases to $R_{\rm out} = 30$ AU, the spectral slope have values in agreement compared to observations (specially for higher values of $\alpha_{\rm turb}$), but the fluxes are slightly higher than the ones detected by mm-observations. This leads to the conclusion that in this case, a combination of fragmentation with a minor drift, to reduce the number of mm-grains, is necessary for a better agreement between theoretical predictions and recent millimeter-observations

of 2M0444+2512. For the faintest disk ρ Oph 102, radial drift is indeed needed in any case. For $R_{\rm out} = 60$ AU, only few cases allow to have $\alpha_{1-3{\rm mm}} \lesssim 3$, nevertheless those cases are more unmatched with millimeter-observation. Finally, for most of the cases of $R_{\rm out} = 100$ AU, the model predictions for the millimeter fluxes and spectral indices are inadequate to explain the observations.

As a conclusion, theoretical models of dust evolution in which the radial drift is set to zero and considering BD disk conditions such as: low mass disks ($M_{\rm disk} = 2\ M_{\rm Jup}$), low radial extension ($R_{\rm out} = 15$ AU), presence of ices that allows to have fragmentation velocities of the order of $v_f = 10\ m\ s^{-1}$ and average turbulence strength $\alpha_{\rm turb} = \{10^{-4}, 10^{-3}\}$, are the models with the best agreement to mm- observations.

3.2.2 Radial drift and pressure bumps

We focus our attention to the most favorable cases: $R_{\rm out} = \{15, 30, 60\}$ AU (focusing further discussions on 15 and 30 AU) and $\alpha_{\rm turb} = 10^{-3}$. The gas density slope is taken to be $p = 0.5$. Considering long-lived pressure bumps, the amplitudes taken are $A = \{0.4, 0.6\}$ (Eq. 3.21). Pinilla et al. (2012a) showed that these kind of inhomogeneities are comparable with global simulation of zonal flows with an amplitude of $\sim 25\%$ by Uribe et al. (2011).

For the simulations with radial drift, $u_{\rm drag}$ and $u_{\rm drift}$ for Eq. 3.2 are taken into account. Therefore, radial drift also contributes to the total relative velocities of dust particles.

Dust density distribution

In a region where the pressure gradient is positive, gas moves with super-Keplerian velocity and particles with sizes corresponding to St $\sim$ 1 would move outwards. As a consequence, inside the pressure bumps there is a natural increment of the amount of dust, allowing to increase the frequency of sticking collisions. Figure 3.5 compares the dust density distribution after 1 Myr of evolution for the case of $R_{\rm out} = 30$ AU, $v_f = 10$ m s^{-1}, $p = 0.5$, $\alpha_{\rm turb} = 10^{-3}$ and two different values of the amplitude of the perturbation $A = 0.4$ and $A = 0.6$. In both cases, with the pressure bumps considered, it is possible to reduce the strong radial drift and retain mm-size particles even after million-year timescales. The efficiency of the presence of the pressure bumps is evident, with many more mm grains than in the test case of Fig. 3.1 (empty disk after 0.5 Myr of dust evolution, Fig. 3.1-top panels). In addition, the effectiveness of the strength of the amplitude i.e. the strength of the

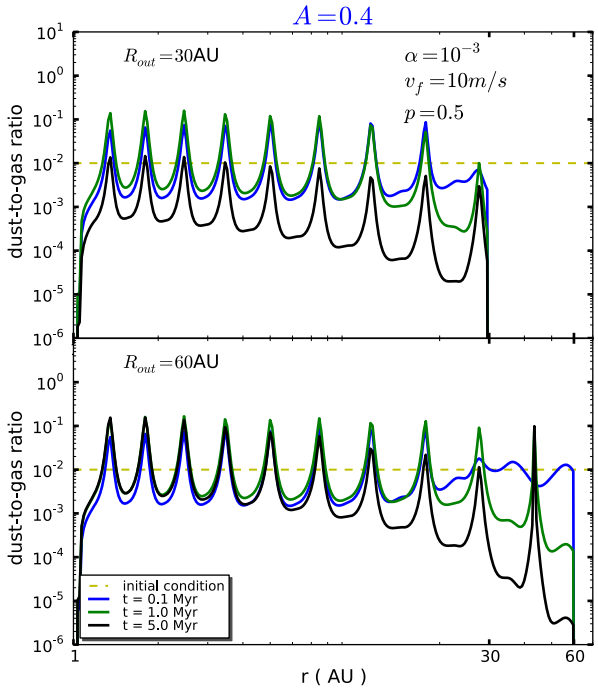

Figure 3.6: Dust-to-gas ratio at different times of dust evolution including radial drift and a bumpy gas surface density (Eq 3.21) with A = 0.4. Case of $\alpha_{\rm turb} = 10^{-3}$, $v_f = 10$ m s^{-1}, $p = 0.5$, $R_{\rm out} = 30$ AU *(top panel)* and $R_{\rm out} = 60$ AU *(bottom panel)*.

pressure gradient, for the trapping of particles is almost the same for both amplitudes after 1 My of evolution.

Inside the bumps, the radial drift is reduced and fragmentation is also less efficient than in the case of Fig. 3.1. With the fragmentation velocity of $v_f = 10\ m\ s^{-1}$, for the cases in Fig. 3.5, particles grow to sizes corresponding to St $\sim$ 1 and due to the positive pressure gradient, grains are trapped inside the bumps. However since fragmentation due to turbulent and azimuthal relative velocities is still happening, when particles collide and become smaller, such that St $<$ 1, are more difficult to trap in the pressure bump (Pinilla et al. 2012a) and would finally drift to the star.

Dust-to-gas ratio

Figure 3.6 shows the radial dependence of the dust-to-gas ratio at different times of evolution for the cases of $\alpha_{\rm turb} = 10^{-3}$, $v_f = 10$ m s^{-1}, $p = 0.5$, in a bumpy gas surface density with $A = 0.4$ and $R_{\rm out} = \{30, 60\}$ AU.

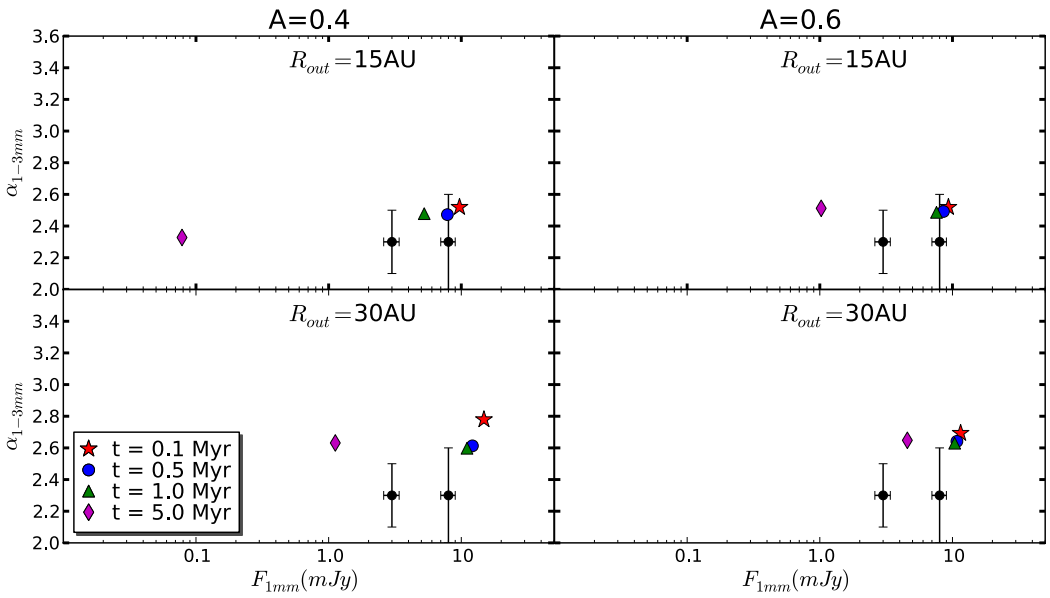

Figure 3.7: Time evolution of predicted fluxes at 1 mm ($F_{1\mathrm{mm}}$) and the spectral index between 1 and 3 mm ($\alpha_{1-3\mathrm{mm}}$) including radial drift and a bumpy gas surface density (Eq. 3.21) with $R_{\mathrm{out}} = \{15, 30\}$ AU, $\alpha_{\mathrm{turb}} = 10^{-3}$, $v_f = 10\ m\ s^{-1}$, A = 0.4 *(left panels)*, A = 0.6 *(right panels)* and $p = 0.5$. Black dots with error bars are millimeter-observations of the young BD ρ-Oph 102 (Ricci et al. 2012) and 2M0444+2512 (Ricci et al. 2013).

For this case, the dust-to-gas ratio remains almost constant with time until 1 Myr of evolution. It increases inside the pressure bumps and varies between $\sim 10^{-2} - 10^{-1}$, however there is a remarkable reduction after 5 Myr of evolution, where it can reach values of 10^{-3} in the inner part and $10^{-4} - 10^{-5}$ in the outer parts of the disk.

When the outer radius increases, the dust-to-gas ratio does not remain constant with time in the outer regions of the disk, and it is possible to distinguish how it decreases with time reaching even values of $\sim 10^{-6}$ in those regions (bottom panel of Fig. 3.6).

It is important to note that the gas density profile remains constant for our dust evolution models, since viscous evolution timescales are longer than dust growth timescales. In addition, we do not consider any mechanism that can selectively disperse the gas such as photoevaporation (see e.g. Gorti et al. 2009; Owen et al. 2011).

Comparison with millimeter-observations

Focussing the attention on the cases where fragmentation is effective (i.e. when $v_f = 10\ m\ s^{-1}$ and $\alpha_{\rm turb} = 10^{-3}$), Fig. 3.7 shows the time evolution of $F_{\rm 1mm}$ and $\alpha_{\rm 1-3mm}$ including radial drift and a bumpy gas surface density with $R_{\rm out} = \{15, 30\}$ AU, $p = 0.5$ and A = $\{0.4, 0.6\}$. For $A = 0.4$, we notice a good match between the theoretical predictions and the observations, even after 1 Myr of evolution, there is still enough mm-grains in the outer regions that contribute to have high values of the flux at 1 mm. The fluxes become lower at 5 Myr, because a significant amount of grains continue to fragment and drift towards the star. However, $F_{\rm 1mm}$ and $\alpha_{\rm 1-3mm}$ at intermediate time steps like e.g. 1 - 2 Myr, coincide well with the observed values, and they are in the range of the estimated ages of the observed BD disks. The effect of increasing the pressure gradient, i.e., higher A is notable, since the fluxes increase due to the fact that there are more grains trapped, in particular at long time-scales, for instance 5 Myr.

To have a better agreement of the predicted fluxes $F_{\rm 1mm}$ and the spectral index $\alpha_{\rm 1-3mm}$ with the current mm-observations of 2M0444+2512 and ρ Oph 102, it would be necessary to increase the mass of the disk. Figure 3.8 shows the comparison of $F_{\rm 1mm}$ and the $\alpha_{\rm 1-3mm}$ for two different disk masses ($M_{\rm disk} = \{2, 5\}\ M_{\rm Jup}$) and the specific case of $R_{\rm out} = 15$ AU, $p = 0.5$, $\alpha_{\rm turb} = 10^{-3}$, $v_f = 10\ m\ s^{-1}$ and $A = 0.4$. Due to the fact that there is a largest amount of dust for $M_{\rm disk} = 5\ M_{\rm Jup}$ than for $M_{\rm disk} = 2\ M_{\rm Jup}$, there is more mm-grains that contribute to the integrated flux and therefore the spectral slope can be lower.

3.3 Summary and discussion

One of the most important problems in the core accretion theory for planet formation is "the meter size barrier". This phenomenon results from the combination of high radial drift and fragmentation. A meter-size object at 1 AU drifts towards the star in timescales much shorter than the growth timescales. In the colder regions of a disk, the same problem occurs when translated to mm-sized grains. Both, radial drift and fragmentation, appear to be different for particles in BD disks.

We have studied how dust evolves and we explore different scenarios where mm-grains survive in BD disks. For the results presented here, we consider typical BD parameters. For instance, the disk outer regions reach temperatures of ~ 10 K. Assuming that MRI is the source of turbulence, which depends basically on the disk temperature and considering $\alpha_{\rm turb}$-prescription,

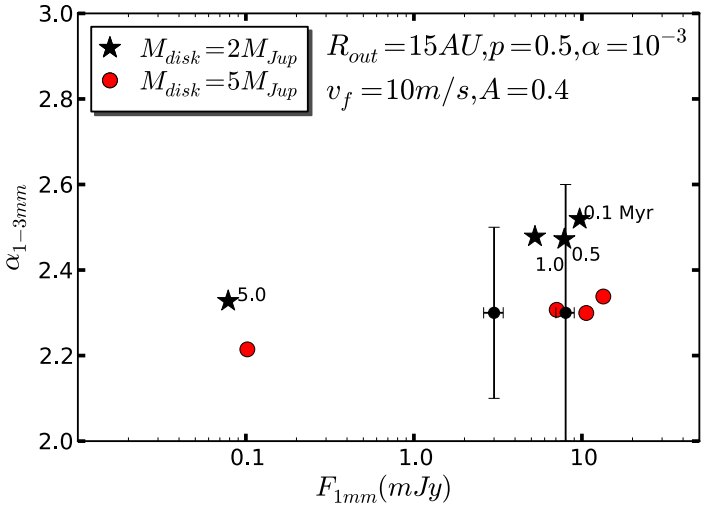

Figure 3.8: Comparison of the predicted fluxes at 1 mm ($F_{1\mathrm{mm}}$) and the spectral index between 1 and 3 mm ($\alpha_{1-3\mathrm{mm}}$) for two different disk masses (M_{disk} = 2 M_{Jup}-star points and M_{disk} = 5 M_{Jup}-dot points). Time evolving data from the right to the left (from 0.1-5.0 Myr as Fig. 3.7). Case of R_{out} = 15 AU, $p = 0.5$, α_{turb} = 10^{-3}, v_f = 10 $m\ s^{-1}$ and A = 0.4.

low and moderate values of α_{turb} were taken (10^{-5} – 10^{-3}). In addition, the presence of ices in the disk was assumed and fragmentation velocities were taken to be v_f = $\{10, 30\}$ $m\ s^{-1}$, based on numerical simulations of collisions with ices (see e.g. Wada et al. 2009). Furthermore, we considered low mass disks (2 M_{Jup}) and typical values for masses and luminosities of BD (see Table 3.1). For the radial extension of BD disks, we considered R_{out} = $\{15, 30, 60, 100\}$ AU. Luhman et al. (2007) present observations combining Spitzer spectroscopy and high-resolution imaging from HST, of a circumstellar disk that is inclined close to edge-on around a young brown dwarf in Taurus, estimating a disk radius of $\sim$ 20-40 AU. ALMA-Cycle 0 observations of ρ-Oph 102 (Ricci et al. 2012) do not resolve the disk, but they estimate an outer radius for the dust of $\sim$15-40 AU. From 3 mm CARMA observations of 2M0444+2512 (Ricci et al. 2013), the outer radius for the dust is estimated to be $\sim$ 20-75 AU for p = 1 and $\sim$ 15-30 AU for p = 0.5.

3.3.1 Fragmentation and drift barriers

We have shown how several dust growth aspects in BD disks differ from T-Tauri and Herbig Ae/Be disks. In the first stages of dust evolution, when particles move along with the gas and coagulate, relative velocities are mainly

due to Brownian motion and settling to the midplane. It was discussed in Sect. 3.1.2 that growth timescales due to settling are shorter at the location of a given temperature in BD than in T-Tauri disks.

When particles reach sizes such that they start to decouple from the gas (i.e. St $\sim$ 1), radial drift and turbulent motion become the main sources for relative velocities. On one hand, we demonstrated in Sect. 3.1.2 that radial drift can be even twice as fast for particles in BD disks than in T-Tauri disks, and as a consequence they would be depleted on shorter timescales. On the other hand, considering moderate $\alpha_{\rm turb}$ and low disk temperatures, turbulent relative velocities are quite low. If turbulence is the main cause for fragmentation, destructive collisions are less likely in BD disks than in T-Tauri disks. When radial drift and fragmentation are considered, BD disks would be dust-poor after only few Myr due to the fast inward migration of dust grains (Fig. 3.1-top panels).

3.3.2 No radial drift

This drastic case, where radial drift is not included, is important to study whether mm-grain can be indeed formed considering dust coagulation/ fragmentation models. When radial drift is set to zero, we found that two different scenarios can happen under BD disk conditions. One scenario is when fragmentation happens due to relative azimuthal velocities taken $v_f = 10\,m\,s^{-1}$ (Fig. 3.2). In this case, it is possible to form mm-grains particles in BD disk and have a good match for the predicted mm-fluxes and spectral indices, in particular for the brightest BD disk 2M0444+2512 (Fig. 3.4) for $R_{\rm out} = 15$ AU. However, for larger disk sizes i.e. $R_{\rm out} = \{30, 60\}$ AU, a slight radial drift is necessary to decrease the predicted mm-fluxes. For the other BD disk ρ Oph 102, radial drift is always needed to reduce by at least a factor of 3 the mm-fluxes.

The second scenario is when fragmentation is less likely i.e. $v_f = 30\,m\,s^{-1}$ (see e.g. Fig. 3.3), when most of the disk is made of big grains (a $>$ 10 cm), leading to low mm-fluxes, underestimating millimeter observations. Therefore, values as $v_f = 30\ m\ s^{-1}$ do not allow to have a good agreement between models and observations and average values of $v_f = 10\ m\ s^{-1}$ are needed.

3.3.3 Radial drift and pressure bumps

In order to reduce the rapid inward drift that dust particles experience in protoplanetary disks and explain the presence of mm-grains in the outer regions of disks, pressure bumps have been suggested as a possible solution

(see e.g. Pinilla et al. 2012a). In this work, when radial drift was taken into account, we considered strong gas density inhomogeneities (40% and 60% of amplitude), that lead to regions in the disk where the pressure gradient is positive. These kind of pressure bumps could be the result of MRI effects (Johansen et al. 2009; Uribe et al. 2011). However, there are no known mechanisms that could produce such kind of pressure bumps with these high amplitudes globally present in the disk. Nevertheless, if the scale-height of a disk is higher as in the case of BD disks, the scale of turbulent structures increases leading to have higher pressure scales (e.g. Flock et al. 2011).

Besides global pressure inhomogeneities from MRI in the disk, a single and high pressure bump can exist in disks. For instance, Rossby wave instability (RWI) generated by the presence of a dead zone (Regály et al. 2012) would create a high-single pressure bump. The possibility of a dead zone in a BD disk is still a debatable subject. On the other hand, the presence of a massive planet could be also the reason to have trapping of particles in a single huge pressure bump (Pinilla et al. 2012b). However, from low mass disks, it is unlikely to have planets massive enough to open a gap. The criterion to open a gap in a disk depends on the local scale height $h(r)$, leading that a clear gap would be less likely for BD than T-tauri disks under the same disk and planet parameters (Crida et al. 2006). Hence, these two possibilities were ruled out for the conditions that we have considered for BD disks and we only focused on global-synthetic pressure bumps that allow to have a large radial distribution of millimeter dust grains in the whole disk.

For simulations with pressure bumps, we considered a sinusoidal perturbation for the gas surface density with two different amplitudes $\mathrm{A} = \{0.4, 0.6\}$ (Eq 3.21) and a wavelength equal to one disk scale-height. The parameters considered for these simulations were taken from the most optimistic no-drift cases. The presence of pressure bumps cause an accumulation of dust in the location of pressure maxima, where radial drift is reduced and fragmentation due to radial drift decreases. Inside those regions, fragmentation would happen only because turbulent or azimuthal motions and it is possible to have a good match between theoretical perspectives and spectral slopes found with millimeter-observations for the two BD disks, specially for the cases of $R_{\rm out} = \{15, 30\}$ AU. Increasing the mass of the disk from 2 to 5 $M_{\rm Jup}$, theoretical predictions and mm-observations match even better. The disk mass predictions for ρ-Oph 102 (Ricci et al. 2012) are 0.2-0 .6 $M_{\rm Jup}$ and for 2M0444+2512 Ricci et al. (2013) are 2.0-5.0 $M_{\rm Jup}$, assuming a gas-to-dust mass ratio of 100.

3.3.4 Comparison between T-Tauri and BD disks

Although T-Tauri and BD disks have very different properties, a first-order comparison between the models that show a good agreement with millimeter-observations in each case can be done. If we compare the best model described in Pinilla et al. (2012a) for T-Tauri disks (pressure bumps with an amplitude A of 30% and one scale-height of the disk as the wide f of the bumps) with the best model for BD disks ($A = 0.4$, $f = 1.0$, $R_{\rm out} = 15$ AU and $M_{\rm disk} = 2\ M_{\rm Jup}$), considering the same disk and dust properties (fragmentation velocity ($v_f = 10$m s^{-1}), viscosity ($\alpha_{\rm turb} = 10^{-3}$), initial dust-to-gas ratio(1/100), etc), we find that 85% of the dust mass is in grains larger than 1 mm in the BD case, versus the 70% for T-Tauri disks. As a consequence, we expect our models to produce slightly flatter SEDs for BD disks than for TTS disks. We stress that this conclusion, being inferred from our 1-D models that are only relevant in the mid-plane, should be taken with care. A proper vertical structure calculation is needed to assess this issue, and see if the effect is strong enough to account for 15-20% variation reported by e.g. Mulders & Dominik (2012) on Chameleon I targets.

3.3.5 Further improvements of the models

The aim of this chapter is to determine the best conditions for grain growth in the mid-plane of BD disks. Our 1-D model is well-suited to this goal, but requires to azimuthally average the surface density profiles, which implies that we do not take into account possible local disk features, that may locally affect dust growth. Going for 2-D and 3-D calculations would allow the vertical disk structure and vertical grain distribution to be computed, and to provide with predictions at shorter wavelengths (e.g. shape of the SED and of the silicate feature) that can be directly compared to large surveys.

Our model can also be improved on the prescription of the dust-evolution process. Recent laboratory experiments using silicates have revealed that particles should also bounce (Güttler et al. 2010), and this process is not included in our model so far. It is however an open question whether this happens in the case of collision between ices (Wada et al. 2011), and if it has a strong impact on dust growth. In fact, the bouncing barrier (Zsom et al. 2010) can be overcome if Maxwellian velocity distributions of relative velocities among dust grains are considered (Windmark et al. 2012a). Windmark et al. (2012b) also showed that after including bouncing effects and considering mass-transfer collisions, km-sized objects can still form at few AU from the star, but if radial drift is neglected and cm-sized seeds inserted initially.

Finally, the main caveat of our study is that we assume that the gas den-

sity profile remains static for million-year timescales, neglecting the impact of different physical processes, as for example the potential time evolution of the pressure bumps, as the case of zonal flows (see e.g. Uribe et al. 2011). Simultaneous modeling of gas and dust evolution is a step forward of our models

3.4 Conclusion

The first steps of planet formation differ between disks around T-Tauri stars than disks around BD. In BD disks, settling is more efficient and BD disks are expected to be flatter. In addition, when dust grows and particles start to decouple from the gas, radial drift is a major problem and fragmentation is less likely than in T-Tauri disks. Our models show that, if BD disks are small (e.g., $R_{\rm out} \lesssim 15$AU), radial drift needs to be completely suppressed to account for the mm-observations of the two BD disks observed so far. However, if disks are larger, then a small degree of radial drift is necessary. Including radial drift, the most favorable conditions after million-years timescales of dust evolution are with strong pressure inhomogeneities of an amplitude of $\sim$ 40%-60%. Global dust evolution models that include the vertical structure are the next step to reproduce all observational signatures of BD disks, as for example the flatter geometry of BD compare with T-Tauri disks, or the large average grain sizes in BD disk atmospheres.

Chapter 4

Ring dust shaped accumulation in transition disks

Based on the paper by ***Pinilla P.****, Benisty, M., Birnstiel, T.,A&A, 545, A81*

Circumstellar disks are the birthsites of planets. The physical conditions and the evolution of these disks control the planet formation mechanisms. An important goal is to provide theoretical models and observational constraints to understand the various stages in the evolution of gas and dust in the disk. Decrease of mass accretion rate (Sicilia-Aguilar et al. 2010; Fedele et al. 2010), and near-infrared excess with time (Hernández et al. 2007; Andrews et al. 2011b) indicate that disks have a range of lifetimes from 1 to 10 Myr.

With the advent of powerful infrared space telescopes such as *Spitzer*, a new class of objects has been identified, called the transition disks (e.g., Espaillat et al. 2010). Their spectral energy distribution (SED) and direct sub-millimeter (mm) imaging suggest that warm dust in the inner disk is strongly depleted compared to the outer disk. The small number of transition disks (Muzerolle et al. 2010) suggests an inside-out evolution that occurs rapidly. Various mechanisms have been proposed so far to explain the inner disk clearing: photoevaporation winds (e.g. Owen et al. 2011), grain growth (Klahr & Henning 1997; Tanaka et al. 2005) and dynamical interactions with companions (Lin & Papaloizou 1979). Transition disks are therefore excellent laboratories for planet formation models.

The clearing of a gap by a companion or planet, from a simplistic point of view, depends on the competition between the viscous torque from the disk and gravitational torques from the planet. For a laminar disk, a 1 $M_{\rm Jup}$ planet can clear a gap or hole. The recent discovery of a companion inside

a massive disk in T Cha (Huélamo et al. 2011) supports the scenario of a dynamical clearing, at least for this object. However, models show that a single planet seems unlikely to be capable of creating the observed large holes, which require multiple systems (Zhu et al. 2011; Dodson-Robinson & Salyk 2011).

Interestingly, for most of these transition disks the inner cavity is not empty. They still present relatively high accretion rates ($\sim 10^{-8} M_{\odot} yr^{-1}$; see e.g.,Calvet et al. (2005); Espaillat et al. (2007)) which implies that the inner cavity is not completely empty and that some gas flows through the gap. To allow mass flowing, a limit for the planet mass can be inferred, depending on the disk viscosity (Lubow & D'Angelo 2006). In addition to the gas, some transition disks also present a strong near-infrared excess, indicating the presence of dust close to the star. Rice et al. (2006) studied the filtration of dust in the gap, considering a fixed size for the dust particles, and concluded that increasing the planet mass from e.g. 0.5 $M_{\rm Jup}$ to 5 $M_{\rm Jup}$, the maximum particle size that sweeps into the gap decreases from ~ 10 μm to a few tenths of a micrometer.

Transition disks are potentially interesting laboratories to study processes related to the impact of planet formation on the disk. One of the most stubborn problems in planet formation is the so-called "meter-size barrier". A one meter size object at 1 AU drifts towards the central star in timescales shorter than the growth timescales, impeding it to grow (see e.g., Brauer et al. 2008; Birnstiel et al. 2010a). In addition, high relative velocities lead to numerous fragmentation collisions converting a large object into smaller dust particles. The same physical process happens to the millimeter-size particles that are observed in the outer regions of the disk (e.g., Wilner et al. 2000; Ricci et al. 2010b; Guilloteau et al. 2011). One possible solution to prevent the rapid inward drift and trap dust particles, is to consider pressure bumps (Klahr & Henning 1997; Fromang & Nelson 2005; Brauer et al. 2008; Johansen et al. 2009; Pinilla et al. 2012a). A long-lived positive pressure gradient can lead dust particles to move outwards, causing an accumulation of dust at the location of the pressure maximum. A large pressure bump is expected in protoplanetary disks as a consequence of the presence of a massive planet in a disk. In fact, when a planet carves a gap in a disk, the gas surface density shows a significant depletion, resulting in a large pressure bump at the outer edge of the gap. The dust material is trapped and piles up in this local pressure maximum where the gas motion is exactly Keplerian, and as a result there is no frictional drag between the gas and the particles. For that reason, not only do the particles not drift anymore, they also do not experience the potentially damaging high-velocity collisions due to relative radial and azimuthal drift. Under those circumstances, growth

to larger-than-usual sizes is expected, possibly even a breakthrough that leads to overcome the growth barrier. However, if turbulence is still strong enough, particles may fragment due to their relative turbulent velocities. This scenario is only possible if we assume the presence of a planet, formed by another mechanism than dust agglomeration.

In this chapter, the goal is to test the idea that the outer edge of a planetary gap is a particle trap. We consider the dust evolution in a disk, where the gas density profile is determined by its interaction with a massive planet. We then explore the case of LkCa 15, a transition disk (Mulders et al. 2010). The disk has been intensively observed at millimeter wavelengths (Piétu et al. 2006; Andrews et al. 2011b) with a maximum angular resolution corresponding to 28 AU (Isella et al. 2012). The dust continuum images show a ring-like structure from $\sim$ 42 to $\sim$120 AU, which is best fitted by a flat surface density profile. In addition, a $\sim$ 6 - 15 $M_{\rm Jup}$ planet in circular orbit and located at 15.7 $\pm$ 2.1 AU, was claimed (Kraus & Ireland 2011), but not confirmed yet.

We describe the numerical simulations of planet-disk interactions that are considered for this work, as well as the coagulation/fragmentation model of the dust evolution in Sect. 4.1. Section 4.2 describes the results of the numerical simulations. In addition, we present observation predictions in Sect. 4.3. Section 4.4 is a discussion of the main results of our work and Sect. 4.5 is a summary.

4.1 Disk-planet interactions and dust evolution

For the disk-planet interaction process, we use the two-dimensional hydrodynamical code FARGO (Masset 2000), that solves the Navier-Stokes and continuity equations. For the dust evolution, we use the code described in Birnstiel et al. (2010a), that computes the coagulation and fragmentation of dust grains, including turbulence, gas drag and radial drift.

4.1.1 Codes

FARGO uses finite differences and a fixed grid in cylindrical coordinates (r, ϕ).Its advantage lies in the calculation of the azimuthal advection. It allows each annulus of cells to rotate at its local Keplerian velocity and at the end of each timescale, the results are stitched together. This technique speeds up the corresponding calculations. FARGO has been used for numerous studies of disk evolution (e.g., Crida et al. 2006; Zhu et al. 2011; Regály et

Table 4.1: FARGO parameters

Parameter	Values
$M_\star[M_\odot]$	1.0
$\Sigma_0[M_\star/r_p^2]$ (flared disk)	1.26×10^{-3}
$\Sigma_0[M_\star/r_p^2]$ (wedge disk)	7.10×10^{-4}
$M_P[M_{\rm Jup}]$	$\{1.0, 9.0\}$
α	$\{10^{-4}, 10^{-3}, 10^{-2}\}$
β	$\{-1, -0.5\}$
$r_{\rm in}[r_p]$	0.1
$r_{\rm out}[r_p]$	7.0
$n_r \times n_\phi$	$[512 \times 1024]$
$\epsilon[h(r)]$	$\{0.6, 0.8\}$
Boundary conditions	open

al. 2012). We selected open inner and outer boundary conditions such that the material can leave the grid when the flow velocity at the inner or outer radial cells is pointing outwards. For this work, we only focus on the gas density profile at the outer edge of the open gap.

For the dust evolution, we consider that grains grow, crater and fragment due to radial drift, turbulent mixing and gas drag. Brownian motion, turbulence, vertical settling, radial and azimuthal drifts are taken into account to calculate the relative velocities of dust particles. For micron-sized particles, the relative velocities mainly result from Brownian motion and settling. These grains grow by coagulation as a result of van der Waals interactions. As they grow, they start to decouple from the gas, and turbulent motion as well as radial drift become the main sources for relative velocities.

When dust grains reach sizes with high enough velocities, they encounter destructive collisions. Particles above the fragmentation velocity always cause fragmentation if the impactor mass is within one order of magnitude of the target, otherwise they cause erosion. The transition from the 100% sticking probability to 100% fragmentation/erosion probability is linearly increasing between $0.2 \times v_f$ to v_f, as in Birnstiel et al. (2010a).

The fragmentation velocities of the dust grains can be estimated based on laboratory experiments and theoretical work of collisions for silicates and ices (e .g., Blum & Wurm 2008; Schäfer et al. 2007; Wada et al. 2009). For silicates, they are of the order of few m s^{-1} (e .g., Blum & Wurm 2008), and increase with the presence of ices (Schäfer et al. 2007; Wada et al. 2009).

Table 4.2: Dust model parameters

Parameter	Values
$M_\star[M_\odot]$	1.0
$M_{\rm disk}[M_{\rm Jup}]$	55.0
α	$\{10^{-3}, 10^{-2}\}$
$r_{\rm in}$[AU]	2.0
$r_{\rm out}$[AU]	140.0
$R_\star$ [$R_\odot$]	1.7
$T_\star$ [K]	4730
ρ_s [g/cm^3]	1.2
v_f [cm/s]	1000

To characterize how well the dust particles couple to the gas, we refer to the Stokes number St, which is defined as the ratio between the turn-over time of the largest eddy ($1/\Omega$) and the stopping time of the particle due to the friction with the gas. In the presence of a drag force, big particles are not affected by the drag and they move with their own Keplerian velocity, implying that St $\gg$ 1. When St $\ll$ 1, the particles are small enough to be well coupled to the gas and move with the gas.

In the Epstein regime, where the ratio between the mean free path of the gas molecules $\lambda_{\rm mfp}$ and the sizes of the particles a is $\lambda_{\rm mfp}/a \geq 4/9$, the Stokes number is at the midplane given by Birnstiel et al. (2010a),

$$\mathrm{St} = \frac{a\rho_s}{\Sigma_g}\frac{\pi}{2}, \tag{4.1}$$

where ρ_s is the intrinsic density of the dust particles, and Σ_g is the gas surface density given by $\Sigma_g = \int_\infty^\infty \rho(r,z)dz$, where $\rho(r,z)$ is the total gas density.

Due to the sub-Keplerian velocity of the gas, particles that are large enough and do not move with the gas velocity experience a head wind, leading them to lose angular momentum and move inwards. The radial component of the dust velocity is the sum of a term corresponding to the frictional drag force (which opposes the motion of the dust grain) and of a term corresponding to the drift velocity, $u_{\rm drift}$, with respect to the gas, which directly depends on the radial pressure gradient $\partial_r P$. It is given by:

$$u_{\rm r,dust} = \frac{u_{\rm r,gas}}{1+\mathrm{St}^2} + \frac{1}{\mathrm{St}^{-1}+\mathrm{St}}\frac{\partial_r P}{\rho\Omega}, \tag{4.2}$$

where $u_{\rm r,gas}$ is the gas radial velocity. The first term is the dominant contribution for St $\ll$ 1. Equation 4.2 assumes low values for the dust-to-gas ratio.

The drift velocity is usually negative, unless the pressure gradient is positive at a given radius. Particles with St = 1 experience the highest possible radial drift.

When particles reach certain sizes due to coagulation, they have relative velocities that may be high enough to cause fragmentation. For particles with St $\sim$ 1, the maximum turbulent relative velocity is given by (Ormel & Cuzzi 2007)

$$\Delta u_{max}^2 \simeq \frac{3}{2}\alpha \mathrm{St} c_s^2, \tag{4.3}$$

where α is the turbulence parameter (Shakura & Sunyaev 1973).

For dust particles with $\alpha/2 \lesssim \mathrm{St} \lesssim 1$ relative velocities are dominated by turbulent motion and radial drift. However, if the radial drift is reduced due to a positive pressure gradient, an approximation of the maximum size of the particles is obtained when the turbulent relative velocities are as high as the fragmentation velocity v_f, therefore:

$$a_{\max} \simeq \frac{4\Sigma_g}{3\pi\alpha\rho_s}\frac{v_f^2}{c_s^2}, \tag{4.4}$$

The dust grain distribution $n(r, z, a)$ depends on coagulation and fragmentation collisions and is described by the Smoluchowski equation (see Birnstiel et al. 2010a, Eq. 35 and Eq. 36). The vertically integrated dust surface density distribution per logarithmic bin is

$$\sigma(r, a) = \int_{-\infty}^{\infty} n(r, z, a) \cdot m \cdot a dz \tag{4.5}$$

where m is the mass of a single particle of size a, hence the total dust surface density is:

$$\Sigma_d(r) = \int_0^{\infty} \sigma(r, a) d \ln a. \tag{4.6}$$

For the coagulation process, the midplane is the most important region, therefore the vertically integrated dust surface density distribution is a good approximation for describing the dust grain distribution. The advection-diffusion differential equation that describes the evolution of the dust surface density Σ_d for a single dust size, can be written in cylindrical coordinates as:

$$\frac{\partial \Sigma_d}{\partial t} + \frac{1}{r}\frac{\partial}{\partial r}\left(r\Sigma_d u_r\right) - \frac{1}{r}\frac{\partial}{\partial r}\left(r\Sigma_g D_d \frac{\partial}{\partial r}\left[\frac{\Sigma_d}{\Sigma_g}\right]\right) = 0, \tag{4.7}$$

where D_d is the dust diffusivity and is equal to $D_d = \nu/(1+\mathrm{St}^2)$, if the gas diffusivity is taken to be the turbulent gas viscosity $\nu = \alpha\, c_s\, h$. Equation 4.7 is solved for each size using the flux-conserving donor-cell scheme (see Birnstiel et al. 2010a, Appendix A).

For a massive planet on a fixed orbit, the gap opening process reaches a quasi-steady state in timescales that are shorter ($\lesssim$ 1000 orbits) than the million-years timescales of the entire process of dust evolution. For this reason, we use the gas surface density after one thousand orbits ($\sim 10^{-2}$ Myr) and take it as an input for the dust evolution models. Therefore, we assume that the gas surface density remains stationary from one thousand orbits to several million years.

We consider that after the giant planet is formed, the disk remains dust-rich and we study how the remaining dust evolves after the gap is open and has reached a quasi-steady state. We consider that the gas does not have any feedback from the dust and stays static during the dust evolution process since the dust density is always less than the gas density. In addition, since the orbital timescales are much shorter than the dust evolution timescales and there are no strong asymmetries produced by the planet, we azimuthally average the surface density for our models. With these assumptions, the dust evolution at the outer edge of the gap is computed in an accurate way.

4.1.2 Set-up

For our simulations, we assume a locally isothermal disk and two different radial density profiles $\Sigma \propto r^{\beta}$. When the disk scale increases with radius as $h/r \propto r^{1/4}$ (flared disk) as suggested by modelling of T Tauri disks (D'Alessio et al. 2001), the temperature scales as $T \propto r^{-1/2}$, and $\beta = -1$. When h/r is constant (wedge disk), the temperature scales as $T \propto r^{-1}$ and $\beta = -0.5$. The α turbulence parameter is considered to have values between 10^{-4} to 10^{-2}, in agreement with magnetorotational instability (MRI) of active disks (Johansen & Klahr 2005). The numerical simulations are performed with $n_r = 512$ radial logarithmically, and $n_\phi = 1024$ azimuthal uniformly distributed grid cells.

All parameters such as the stellar properties, kinematic viscosity, disk mass, the scale height and the gas density profile of the disk are taken to be the same between the hydrodynamical gas evolution and the dust coagulation simulations.

For FARGO simulations, we use normalized units such that $G = M_\star + M_P = 1$ and the location of the planet is at $r = 1$. The simulations are performed from $r_{\rm in} = 0.1$ to $r_{\rm out} = 7.0$, such that the planet is

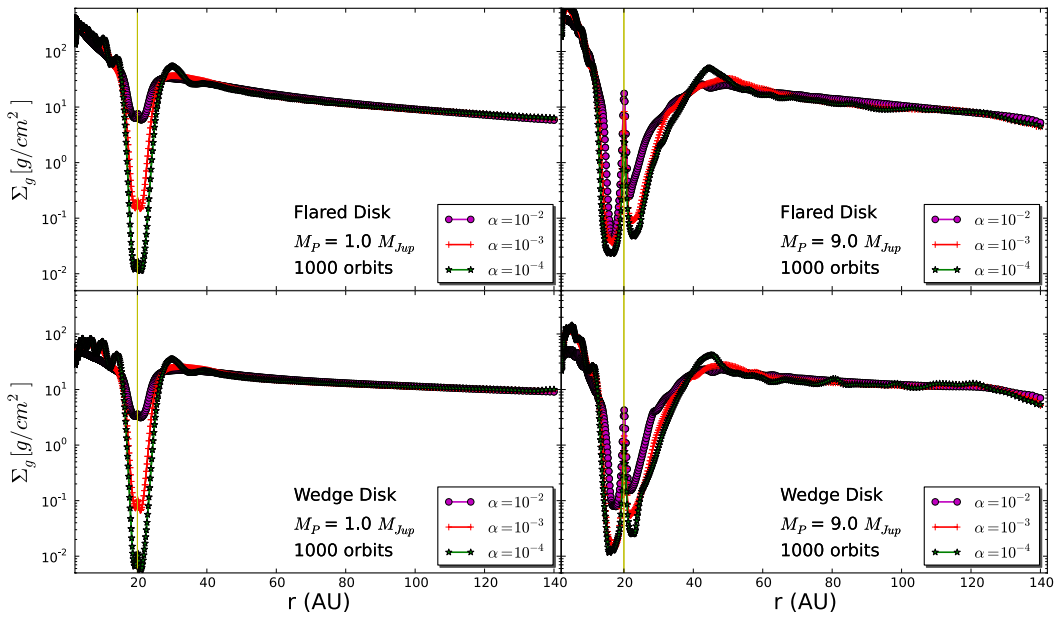

Figure 4.1: Azimuthally averaged surface density after 1000 orbits and three different values of α-turbulence for a gap created by a planet located in a fixed orbit at 20 AU of 1 $M_{\rm Jup}$ in a flared disk (top-left), 9 $M_{\rm Jup}$ in a flared disk (top-right), 1 $M_{\rm Jup}$ in a wedge disk (bottom-left) and 9 $M_{\rm Jup}$ in a wedge disk (bottom-right). The peak of the gas surface density at the position of the planet is due to the strong gravitational effect of the massive planet on the gas of the disk.

at $r_p = 20$ AU for a grid from 2 AU to 140 AU. The initial gas surface density Σ_0 at the position of the planet is fixed $\Sigma = \Sigma_0(r/r_p)^\beta$, such that it is around $\sim$ 1-1.5 the minimum mass solar nebula (Hayashi 1981), and the disk mass is around $\sim$0.055 $M_\star$. We consider a planet at a fixed orbit, with two different masses, 1 $M_{\rm Jup}$ and 9 $M_{\rm Jup}$. The planet is introduced slowly into the smooth disk to avoid numerical issues. Planetary accretion is not taken into account since this process is still debated. We use $M_\star = 1\ M_\odot$, and consequently, $M_{\rm disk} = 55\ M_{\rm Jup}$. Finally, the gravitational effect of the planet is smoothed out, such that the gravitational potential ϕ is softened over distances comparable to the disk scale height:

$$\phi = -\frac{GM_P}{(r^2+\epsilon^2)^{\frac{1}{2}}}, \tag{4.8}$$

where ϵ is taken to be 0.6 h. The main FARGO parameters are summarized in Table 4.1.

For the dust evolution, we consider that all particles are initially 1 μm large, and a dust-to-gas ratio is 0.01, with an intrinsic volume density of $\rho_s = 1.2$ gcm^{-3} and a fragmentation velocity of $v_f = 1000$cm s^{-1}. Two additional stellar parameters are taken into account, the stellar radius which is taken to be $R_\star = 1.7\ R_\odot$ and the star effective temperature $T_\star = 4730$ K, as typical values for T Tauri stars. The parameters of the dust evolution simulations are in Table 4.2.

4.2 Results

4.2.1 Gas density profile

Figure 4.1 shows the azimuthally averaged gas surface density after 1000 orbits in four different cases: a 1 $M_{\rm Jup}$ and a 9 $M_{\rm Jup}$ planet on a fixed orbit at 20 AU in a flared and wedge disk respectively. In each case, three different values for α turbulence parameter are considered.

With a 1 $M_{\rm Jup}$ planet and a high value of $\alpha = 10^{-2}$, the viscous torque on the gas exceeds the gravitational torque by the planet, resulting in a much less pronounced gap than in the cases of $\alpha = 10^{-3}$ and $\alpha = 10^{-4}$. The gap is replenished easily because of the high viscosity of the disk as already predicted by different authors (e.g De Val-Borro et al. 2006; Crida et al. 2006). However, for all α values, the width of the gap is roughly the same. It is independent of the viscosity and it depends basically on the mass and location of the planet. We notice that with low viscosity, the density waves

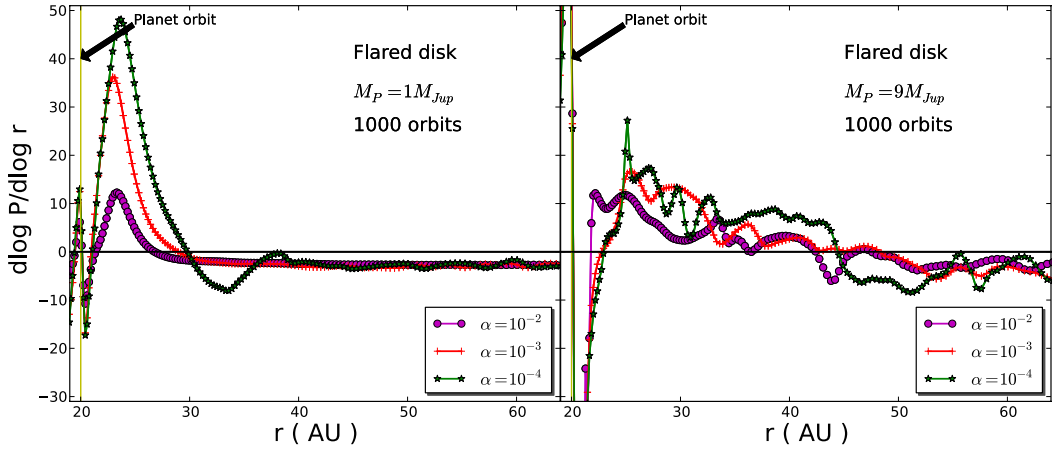

Figure 4.2: Radial pressure gradient after 1000 orbits and three different values of α turbulence for a gap created by a planet located in a fixed orbit at 20 AU of 1 $M_{\rm Jup}$ and 9 $M_{\rm Jup}$ in a flared disk.

that are produced by the planet-disk interaction at the gap edges, become more pronounced but they eventually damp with radius. Indeed, with a 1 $M_{\rm Jup}$ planet, these waves disappear beyond 40 AU and the disk surface density profile follows the initial power law. In this case, the main difference between the two disk geometries that we consider, is that for each value of α, the gap is slightly deeper for a wedge than for a flared disk.

With a 9 $M_{\rm Jup}$ planet, the gravitational torque dominates the viscous torque and the depth of the gap is almost independent of the values that we consider for α. After 1000 orbits the surface density reaches almost the same values near the planet and the width of the gap slightly changes for the different values of turbulence, when the disk is less turbulent the gap is moderately wider. The density perturbation waves are more evident in this situation than for 1 $M_{\rm Jup}$, however, for $\alpha = 10^{-3} - 10^{-2}$, they again damp with radius, and at around 60 AU the gas surface density follows the initial power law. After 1000 orbits and $\alpha = 10^{-4}$, the density perturbation due to the planet is still propagating, for this reason the wiggles in the density profile are stronger than in the cases of $\alpha = 10^{-3} - 10^{-2}$. These wiggles are still present for $r > 100$ AU and they change slightly with the geometry of the disk.

In all four cases, it is possible to distinguish a peak in the surface density at the position of the planet, due to circumplanetary material. This is a natural consequence of the planet insertion in a smooth disk, and because the accretion onto the planet is not considered, the peak remains unaltered

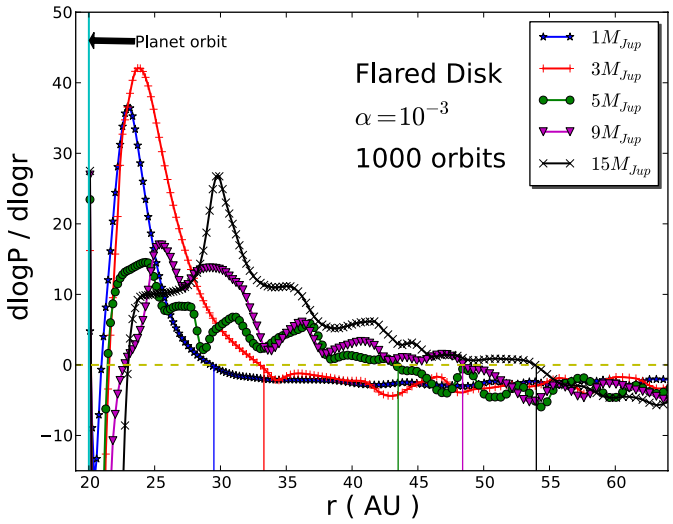

Figure 4.3: Effect of the planet mass on the radial pressure gradient after $\sim$ 1000 orbits in a flared disk, $\alpha = 10^{-3}$ and five different values of the planet mass. The planet is located at 20 AU. The vertical lines indicate the locations of the pressure maximum.

during the simulations.

4.2.2 Pressure gradient

As explained before, the rapid inward drift of the particles stops if the gradient of pressure is positive and the particles pile up in the pressure maxima. Depending on the strength of the pressure gradient, the particles can be trapped or not in the pressure bump (Pinilla et al. 2012a). Figure 4.2 shows the radial pressure gradient considering the azimuthally averaged gas surface density after one thousand orbits, in the case of a flared disk and with an isothermal equation of state. The pressure is given by $P(r) = \rho(r)\, c_s^2(r)$, where the sound speed is defined as

$$c_s = \sqrt{\frac{k_B T}{\mu m_p}}, \tag{4.9}$$

where k_B is the Boltzmann constant, m_p is the proton mass and μ is the mean molecular mass, which is $\mu = 2.3$ in proton mass units. If the temperature is considered as a smooth decreasing function with radius, density variations induce pressure inhomogeneities. We can see that for a 1 $M_{\rm Jup}$ planet, there is a noticeable difference in the amplitude of the pressure gra-

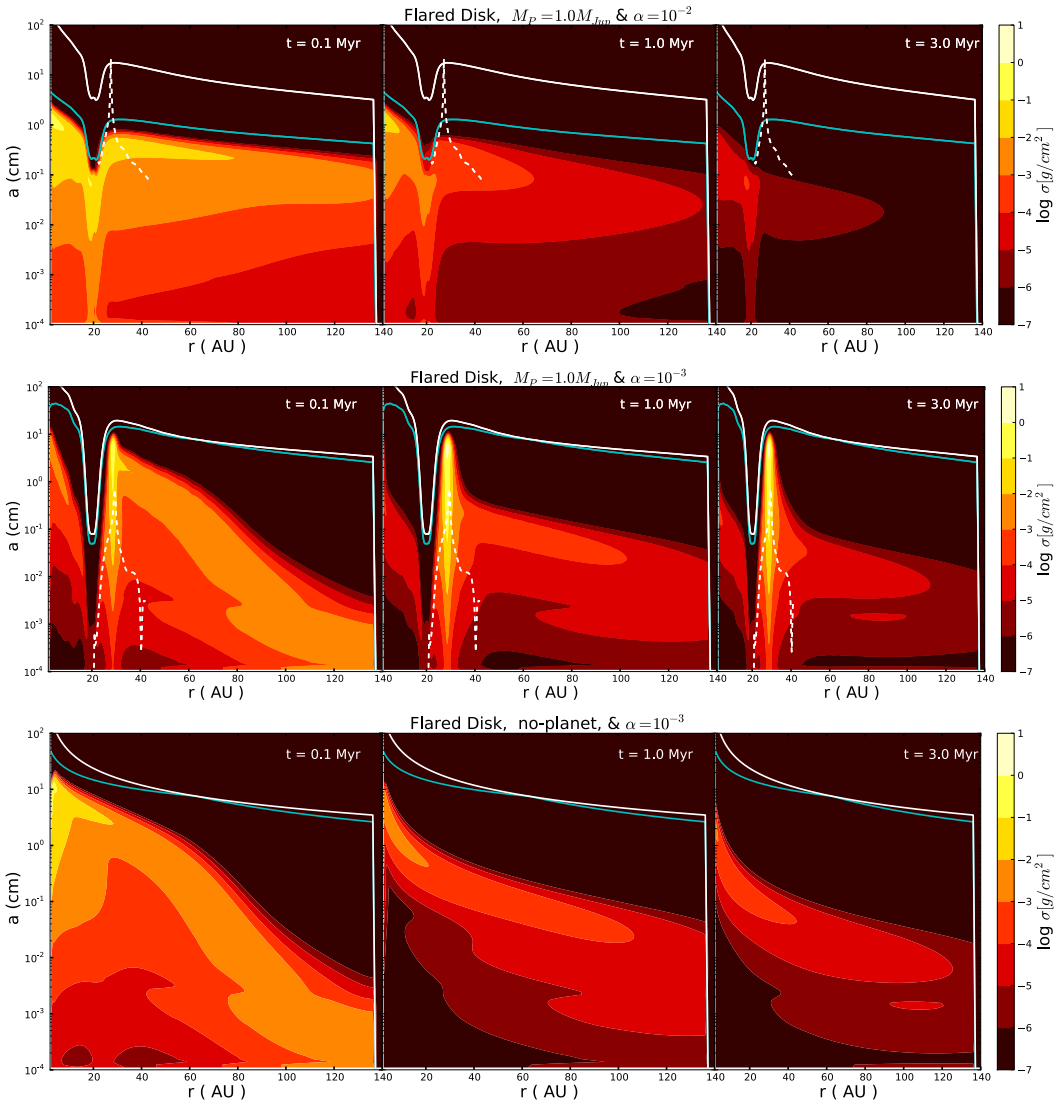

Figure 4.4: Vertically integrated dust density distribution at different times of evolution. Case of a surface density with a gap created by 1 $M_{\rm Jup}$ located in a fixed orbit at 20 AU in a flared disk and $\alpha = 10^{-2}$ (top panel), $\alpha = 10^{-3}$ (middle panel). Case with no planet and $\alpha = 10^{-3}$ (bottom panel). The solid white line represents the particle size corresponding to St = 1, while the blue line corresponds to the fragmentation barrier according to Eq. 4.4 (Brauer et al. 2008; Birnstiel et al. 2010a). The dashed line corresponds to the size for which particles drift faster than those dragged by the gas. Particles above the dashed line are perfectly trapped.

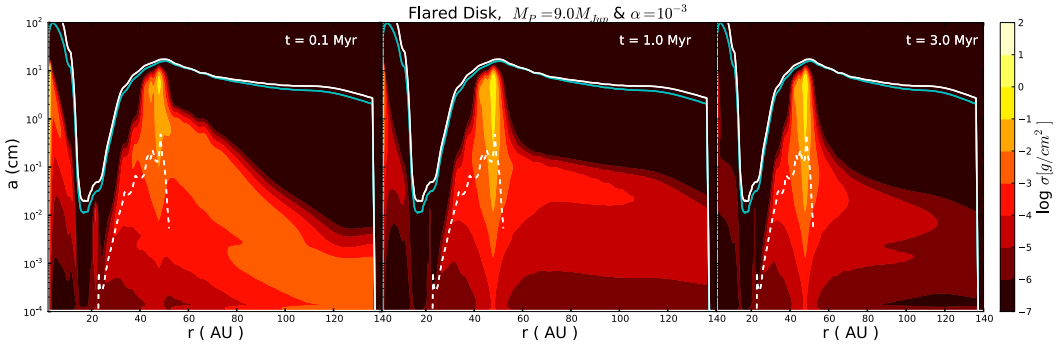

Figure 4.5: Vertically integrated dust density distribution at different times of evolution for a surface density with a gap created by 9 $M_{\rm Jup}$ located in a fixed orbit at 20 AU in a flared disk and $\alpha = 10^{-3}$. Lines are as in Fig. 4.4.

dients for $\alpha = 10^{-2}$ and $\alpha = 10^{-4} - 10^{-3}$. The pressure gradient is positive from ∼22 AU to ∼30 AU, and since $u_{\rm drift} \propto \partial_r P$ (Eq. 4.2), the dust particles have positive drift velocities and move outwards. In all cases, the zero point of the pressure gradient is located at ∼ 10 AU (with a slight variation with viscosity) from the planet orbit and does not change with the geometry of the disk, since the density profile behaves almost the same for flared and wedge disks.

For a 9 $M_{\rm Jup}$ planet orbiting at 20 AU, the pressure gradient on average behaves similarly for each of the α values. The wiggly profile of the gradient is due to the density waves that are produced by the interaction between the planet and the disk. For this planet mass and all values of α, the pressure gradient is positive right after the planet location and remains positive until around 48 AU, and then becomes again negative for both cases of flared and wedge disks. The influence of the planet mass on the range where the pressure gradient is positive is remarkable.

In both mass regimes, it is clear that the location of the pressure maximum differs from the outer edge radius of the gap, where the gas density again starts to increase. Therefore, if the pressure gradient is high enough to moderate the rapid inward drift, dust particles are trapped further away from the gap outer edge in the gaseous disk. This implies that the gap width for the gas is smaller than the one for the dust.

Figure 4.3 summarizes these findings, and shows pressure gradient curves for additional planet masses, $M_p = \{1, 3, 5, 9, 15\} M_{\rm Jup}$ with orbital radius $r_p = 20$ AU. The pressure gradient has its zero point at around $\{29.5, 33.5, 43.5, 48.5, 54.0\}$ AU respectively.

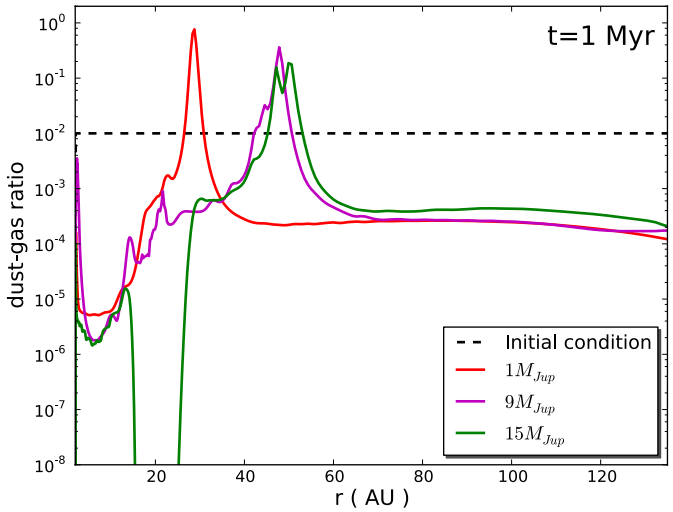

Figure 4.6: Dust-to-gas ratio for 1, 9 and 15 $M_{\rm Jup}$ planet, after 1 Myr of dust evolution

As a comparison, we use the Hill radius r_H, defined as $r_H = r_p\,(M_p/3M_\star)^{1/3}$. In spite of the fact that the outer gap edge in the gas is at most 5 r_H (see e.g. Dodson-Robinson & Salyk 2011), we find that the location where dust accumulates (i.e., the location of the maximum of the pressure) is at $\sim 7\ r_H$ for 1 and 3 $M_{\rm Jup}$ planets, and $\sim 10\ r_H$ for planets with $M_p \geq 5\ M_{\rm Jup}$. This result will be discussed in more detail in Sect. 4.4.

Note that for the FARGO simulations in the case of a 15 $M_{\rm Jup}$ planet, we insert the planet in the disk after more orbits than in the other cases studied in Sect. 4.2.1, we use non-reflecting boundary conditions and a smoothing parameter of $\epsilon = 0.8h$ (see Eq. 4.8) to smooth out the strong density waves produced in this scenario.

4.2.3 Dust size evolution

For the study of the density distribution of dust particles, we again focus on the flared disks, since this disk geometry is in good agreement with observations of T Tauri disks (D'Alessio et al. 2001). For this section, the surface density peak at the planet location was smoothed out to avoid artificial effects at this location.

Top and middle panels of Fig. 4.4 show the vertically integrated dust density distribution at different evolution times for a gas surface density with a gap created by a 1 $M_{\rm Jup}$ planet located in a fixed orbit at 20 AU, and two different values of α turbulence. As explained before the timescales of the

gap opening process are much shorter than the whole dust evolution process, which allows us to take the gas surface density after $\sim$ 1000 orbits and consider that it remains quasi-stable during the dust evolution. The solid white line has the shape of the gas surface density profile and is calculated when the particle size corresponds to a Stokes number of unity (Eq. 4.1). The blue line is the maximum size that particles can reach before they have velocities higher than the fragmentation limit. It is important to note that the maximum size of the particles is inversely proportional to the turbulence parameter (Eq. 4.4), for this reason the maximum possible grain size (blue line) differs by one order of magnitude for each α turbulent parameter considered.

The dashed line provides an approximation of the minimum size of the particles that are trapped in the pressure maximum. Particles with sizes over the dashed line are trapped and the ones below the line are dragged by the gas. This condition is found when the radial component of the dust velocity (Eq. 4.2) is positive, therefore:

$$\mathrm{St} > -\frac{u_{\mathrm{r,gas}}}{\partial_r P}\rho\Omega, \tag{4.10}$$

which in terms of the particle size and pressure gradient can be written as:

$$a_{\mathrm{critical}} = \frac{6\alpha\Sigma_g}{\rho_s\pi|(d\log P/d\log r)|}\left|\left(\frac{3}{2}+\frac{d\log\Sigma_g}{d\log r}\right)\right|. \tag{4.11}$$

Effect of turbulence

We notice a significant influence of the trapping of dust particles on the strength of the pressure gradient. Micron-size particles (St $\ll$ 1), which are easily mixed due to turbulence, are more difficult to trap, they go through the gap and finally drift towards the star. Dust grains with larger Stokes number can perfectly be trapped because they feel a tail-wind due to the fact that the gas moves with super-Keplerian velocity where the pressure gradient is positive, resulting in an outwards movement for those particles.

For $\alpha = 10^{-2}$, the pressure gradient is less steep, the turbulent mixing and drag along the accretion flow wins over the trapping, and the dust gets lost onto the star. Even when the pressure gradient is positive in a range ($\sim$ 22-30) AU, it is not sufficient to trap the particles in the pressure maximum. Indeed, after 3 Myr there is almost no dust remaining in the whole disk.

For $\alpha = 10^{-3}$ turbulence mixing is less strong and in the range of ($\sim$ 22-30) AU, the pressure gradient is greater (Fig. 4.2-left panel), and is

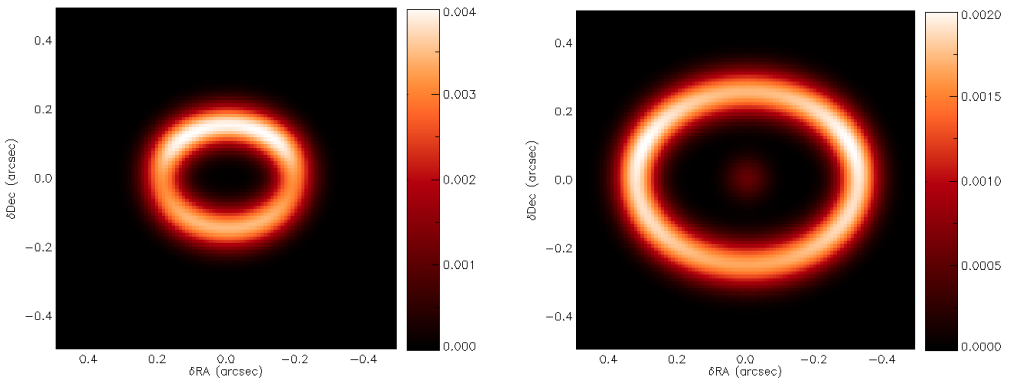

Figure 4.7: Left: 1.3 mm map in the 1 $M_{\rm Jup}$ case, convolved with a beam of 0.1" × 0.1". Units are in Jy/beam. Right: same for 9 $M_{\rm Jup}$.

high enough to stop the rapid inward drift of the particles. The particles are quickly trapped at the location of the pressure maximum ($\sim$ 30 AU) and stay there after several Myrs. The gap created in this case filters out all particles larger than a few μm and the particles that are inside the gap eventually drift towards the star. The gap formed by 1 $M_{\rm Jup}$ mass planet with $\alpha = 10^{-3}$ produces a pressure gradient high enough to create a concentration of dust particles at 10 AU from the location of the planet and the particles reach sizes of a few cm.

As we note in Fig. 4.2- left panel, for 1 $M_{\rm Jup}$ and $\alpha = 10^{-4}$, the pressure gradient is slightly higher than in the case of $\alpha = 10^{-3}$, therefore the dust particles should be easily trapped in this case reaching even larger sizes (Eq. 4.4). For comparison, we notice in the bottom panel of Fig. 4.4, that in the case without planet and with the same disk and stellar parameters, the dust instead of being trapped, grows, fragments, mixes and drifts to the star without forming any mm-size pebbles in the outer regions of the disk $r > 20$ AU.

The necessary size that particles have to reach to be trapped (Eq. 4.11) is higher than the maximum sizes reached due to relative turbulent motion (Eq. 4.2). The influence of turbulence for the dust dynamics is remarkable, if turbulence is not considered, particles grow enough to be decoupled from the gas and they would be trapped because of the positive pressure gradient regardless of its strength. However, we conclude that the high turbulence causes particles to go through the gap and drift finally to the star, due to the fact that they reach high relative turbulent velocities which favors fragmentation, so the mm-size particles become again micron-size grains which are not possible to trap with the strength of the pressure gradient produced

with $\alpha = 10^{-2}$.

Effect of planet mass

In the case of a 9 $M_{\rm Jup}$ planet, the pressure gradient is roughly similar for each of the values of the turbulence parameter α (see Fig. 4.2-right panel), hence for the dust density evolution we concentrate on the intermediate value of the viscosity, $\alpha = 10^{-3}$. Figure 4.5 illustrates the vertically integrated dust density distribution for the case of 9 $M_{\rm Jup}$ at different times of evolution. Similar to the case of 1 $M_{\rm Jup}$ planet and $\alpha = 10^{-3}$, the dust particles grow and due to the positive pressure gradient between $\sim$ 22 and $\sim$ 48 AU (Fig. 4.2-right panel), the rapid inward drift is counteracted by the positive local pressure gradient and the particles are retained in a broad bump of $\sim$ 20 AU width. The dust particles in the outer regions of the disk grow until mm sizes and remain there even after a few Myrs. It is important to mention that even when the pressure gradient reaches a similar value to the case of 1 $M_{\rm Jup}$ and $\alpha = 10^{-2}$, for which there is not particle trapping at all, the turbulent relative velocities are lower and the range of positive gradient is wider, enabling dust retention (Pinilla et al. 2012a).

Comparing the dust evolution with $\alpha = 10^{-3}$ for a 1 $M_{\rm Jup}$ (Fig. 4.4-bottom panel) and a 9 $M_{\rm Jup}$ (Fig. 4.5), we can conclude that the planet mass directly influences the position where the dust can be retained and that the dust bump is wider for the more massive planet. In addition, the pressure gradient created by the different planet masses also affects the size for which particles are trapped. For the same turbulence parameter $\alpha = 10^{-3}$ and 1 $M_{\rm Jup}$, the maximum $a_{\rm critical}$ is equal to $\sim$ 0.70 cm, while for 9 $M_{\rm Jup}$ the maximum $a_{\rm critical}$ is $\sim$ 0.47 cm.

Dust to gas ratio

It is important to note that for the dust evolution models, we assume low values for the dust-to-gas ratio and we do not consider to have any feedback from the dust to the gas, since the gas density remains static. However, when the dust accumulates and grows forming a pile-up, the dust-to-gas ratio can reach values close to one. When the dust-to-gas density ratio is close to unity, the feedback from the dust to the gas is non negligible and the growth timescales can be faster than the drift timescales (Youdin & Goodman 2005), potentially leading to planetesimal formation in the absence of self-gravity. Nevertheless, these streaming instabilities are powered by the relative drift velocities between dust particles and gas, therefore in the pressure maximum where the radial drift of the dust is reduced, these instabilities are unlikely

and our assumptions are still valid.

Figure 4.6 shows the dust-to-gas ratio for each considered case of the planet mass after 1 Myr of dust evolution. The maximum value that the dust-to-gas ratio is $\sim \{0.76, 0.36, 0.18\}$ in the cases of 1, 9 and 15 $M_{\rm Jup}$, respectively. This variation of dust to gas ratio with the planet mass can be explained considering that as the pressure bump gets wider, the dust accumulates and grows in an extended radial region. The dust-to-gas ratio is therefore higher for lower planet mass, when the pressure gradient is higher and positive in a narrower region (see Fig 4.3). In addition, we can notice in Fig. 4.6 that for the 15 $M_{\rm Jup}$ mass planet, the dust-to-gas ratio reaches very low values at the location of the planet, for which the gas drag and drift is inefficient. Therefore the remaining dust in the inner region is just the initial dust that was initially in the inner part. If the initial size of the particles is taken smaller (e.g. 0.01 μm), the sub-micron size particles would go through the gap and replenish the inner part. However, for the 1 and 9 $M_{\rm Jup}$ cases, the micron size dust from the outer region which are not trapped, can drift and be dragged by the gas and finally move through the gap.

4.3 Observational predictions

4.3.1 Emission maps

In this section, we present continuum maps computed at a wavelength of 1.3 mm. We use the gas profiles described in Sect. 4.1.2 and dust size distributions determined in Sect. 4.2.3 and shown in Fig. 4.4-middle panel and Fig. 4.5. We consider the same aspect ratio as in the FARGO and dust evolution simulations, and compute the volume density following:

$$\rho(r,z) = \frac{\Sigma(r)}{\sqrt{2\pi}h(r)} \times \exp\left(-\frac{z^2}{2h(r)^2}\right), \tag{4.12}$$

with Σ, the dust surface density and $h(r)$, the scale height. After retrieving the optical constants[1], we compute the opacities for silicate grains, following the Mie theory. The dust temperature is then computed self-consistently after solving the radiative transfer with the RADMC3D code [2].

We consider the cases of $\alpha = 10^{-3}$, a planet with masses of 1 and 9 $M_{\rm Jup}$ planets and orbiting at 20 AU, after 1 Myr. We use 40° and 90°, as the disk inclination and position angle, respectively, and a distance of 140 pc. The images are convolved with a 0.10"x0.10" beam as required for ALMA for

[1] http://www.astro.uni-jena.de/Laboratory/Database/databases.html
[2] http://www.ita.uni-heidelberg.de/~dullemond/software/radmc-3d/index.shtml

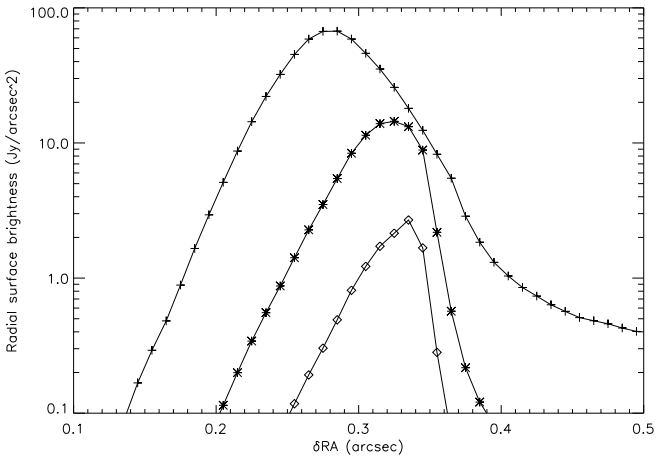

Figure 4.8: Radial surface brightness in the 9 $M_{\rm Jup}$ case, computed at 160μm (crosses), 360μm (stars) and 870μm (diamonds).

typical sizes and distances of protoplanetary disks. As shown in Fig. 4.7, our model images are very similar to the transition disks observations in the (sub-)millimeter regime, that reveal a continuum emission as a resolved ring-like feature (e.g., Williams & Cieza 2011; Andrews et al. 2011a; Isella et al. 2012). In addition, after 1 Myr of dust evolution, we estimate a spectral index of ∼2.7 by integrating the flux over the entire disk at wavelengths of 1 mm and 3.0 mm. This value is in agreement with recent observations (Ricci et al. 2010b).

Due to the wide distribution of particles around the pressure bump (see, e.g., Fig. 4.5), the brightness distribution is expected to change with wavelength. This feature is also reproduced by our model, as shown in Fig. 4.8.

4.3.2 The case of LkCa 15

In this section, we apply and discuss our model in the context of the transition disk LkCa15, for which a wealth of observational data is published. Andrews et al. (2011a) presented a 870 μm image obtained at high angular resolution (0.25″) combining observations from the Submillimeter Array (SMA) and Plateau de Bure Interferometer (PdBI). These observations of the dust continuum emission confirms a ring-like structure at ∼50 AU from the star. They compared these observations with four possible models, concluding that their best fit corresponds to a gap possibly opened by a 9 $M_{\rm Jup}$ companion at $\sim$ 16 AU in a wedge disk, with a constant disk aspect ratio of $h/r = 0.05$ and constant viscosity $\nu = 10^{-5}$ (which corresponds to

$\alpha \sim 10^{-3}$). In Sect. 4.2, we demonstrated that, in the case of a 9 $M_{\rm Jup}$ planet and $\alpha = 10^{-3}$, the pressure maximum is located around $\sim 1.4\ r_p$ from the planet (with r_p, the planet location), which implies that the pile-up of dust (up to cm-sizes) would be located at around $\sim$ 38 AU. Therefore, to have an agreement with the depletion of dust opacities until $\sim$ 50 AU, a bit more massive or/and further located companion is necessary to reproduce the ring-like structure as we will discuss below.

Although not confirmed, Kraus & Ireland (2011) claimed to have detected a $\sim\ 6-15\ M_{\rm Jup}$ planet at 15.7 ± 2.1 AU in LkCa15. Considering the upper limit for the mass and the location of the planet at 20 AU, the zero point for the pressure gradient would be located $\sim$ 54 AU (Fig. 4.3). Hence, dust would accumulate at $\sim$ 54 AU distance from the star, in better agreement with the observed ring radius.

Figure 4.9-top panel shows the vertically integrated dust density distribution after 1 Myr of evolution in the case of a gap opened by a 15 $M_{\rm Jup}$ planet, embedded in a flared disk with $\alpha = 10^{-3}$ and the same parameters given in Tables 4.1 and 4.2. Considering this dust distribution, Fig. 4.9-bottom panel gives the 1.3 mm continuum map, considering a disk inclination of 51°, a disk position angle of 64.4°, a distance of 140 pc, and convolved with a beam of $0.21'' \times\ 0.19''$ (Isella et al. 2012). This image shares striking similarities with the ones published, with similar inner radii for the ring and similar surface brightness. We note however, that we do not reproduce the observed width of the ring, as after 1 Myr already, most of the outer disk particles are retained in a very narrow region. Nevertheless, Pinilla et al. (2012a) demonstrated that the presence of long-lived pressure bumps such as results from MRI can explain the presence of mm-size grains in the regions of the disk outside 50 AU. The combination of those pressure inhomogeneities and the interaction between a massive planet with the disk may explain the radial extent.

Unlike our models with an alpha-viscosity and a massive planet embedded in the disk, Isella et al. (2012) model a gas density profile which increases with radius for the inner part due to the extremely rapid increase of the viscous accretion velocity for smaller radius. They fit their CARMA 1.3 mm observations assuming no planet with the following gas surface density:

$$\Sigma(r) = \Sigma_t \left(\frac{r_t}{r}\right)^{-\gamma} \times \exp\left\{-\frac{1}{2(2-\gamma)}\left[\left(\frac{r}{r_t}\right)^{2-\gamma} - 1\right]\right\}, \qquad (4.13)$$

where the viscosity is given by $\nu(r) \propto r^{\gamma}$. Their best fit model corresponds to $\gamma = -2.15$, $r_t = 60$ AU and $\Sigma_t \sim 10.37$ g.cm^{-2}, for a disk extending

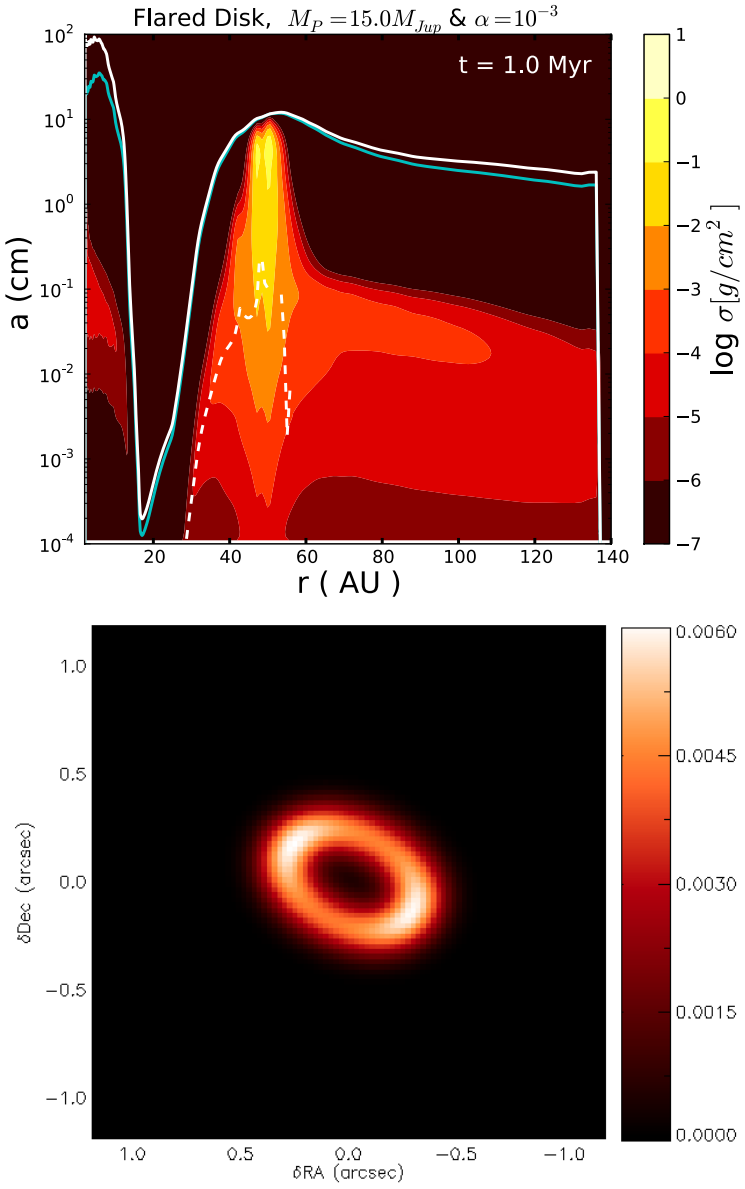

Figure 4.9: Vertically integrated dust density distribution at 1 Myr of evolution for a surface density with a gap created by 15 $M_{\rm Jup}$ located in a fixed orbit at 20 AU in a flared disk and $\alpha = 10^{-3}$ (top-panel). Bottom-panel is the 1.3 mm continuum model map for LkCa15 considering the dust density distribution shown in top-panel. The map is convolved with a beam of 0.21" × 0.19", corresponding to the maximum angular resolution achieved by Isella et al. (2012). Units are in Jy/beam.

from 0.2-160 AU. Their gas density profile suggests that the pressure gradient would be positive from the inner radius until the characteristic radius r_t and smoothly becomes negative until the outer radius of the disk. This implies that the dust particles would have a positive drift velocity in the inner regions, and negative in the outer regions of the disk. They would therefore move outwards from the inner radius to r_t, and from the outer radius inwards to r_t, creating a wide concentration of dust around 60 AU.

This complementary study, that uses a prescription of the surface density based on the viscous evolution of the disk, leads to the same conclusion as our model, i.e., a pressure maximum around 60 AU. In fact, the profiles are very similar in the range of radii in which the dusty ring is observed (see Fig. 1 in Isella et al. (2012)).

4.4 Discussion

Hydrodynamical simulations of planet/disk interactions combined with dust coagulation/fragmentation models can reproduce the ring-like emission of some transition disks.

4.4.1 Dust evolution

To compute the evolution of dust, one has to account for four important physical mechanisms: coagulation, fragmentation, radial drift and turbulent mixing. Coagulation is important for grains to grow to large sizes, as inferred from millimeter observations. Fragmentation continuously replenishes the disk in small grains. If we do not consider fragmentation, in the region where the pressure gradient is positive, particles would accumulate, grow above the fragmentation barrier and reach the maximum size of $\sim$2 m considered in our models. This would happen on timescales as short as $\sim$ 0.1 Myr, and would result in a disk only made of large particles. As meter-size objects have St $\gg$ 1, they would therefore not be coupled with the gas anymore, move at Keplerian velocity, and would not be trapped. These grains would in addition have very low opacities, which would result in the underestimation of millimeter fluxes in the millimeter.

Radial drift is essential to distribute the grains over the disk extent. Birnstiel et al. (2010b) showed that if the radial drift is neglected, dust grains could acquire millimeter sizes, but would lead to over-predictions of mm-fluxes. In our model of LkCa15, we overcome this issue and obtain flux levels similar to the ones measured by Isella et al. (2012).

Finally, turbulent mixing provides the necessary relative velocities for

grains to fragment, directly influencing the maximum particle size (Eq. 4.4), and distribute the grains of various sizes all over the disk. In Sect. 4.2.3, we showed that the efficiency of particle trapping depends on the viscosity of the disk. For a shallow gap (see Fig 4.4), we concluded that when the pressure gradient is not high enough, drag forces and diffusion do not allow particles to be trapped.

Our model can however still be refined. Recent collision experiments with silicates show that particles should also bounce as an intermediate step between sticking and fragmentation (Güttler et al. 2010). In fact, Windmark et al. (2012b) showed that with the insertion of cm-sized seeds, considering mass transfer processes and bouncing, at a distance of few AU, small dust can grow to $\sim$ 100 meters on timescales of 1 Myr. A similar process could happen to mm-sized particles in the outer regions of the disks. However, in the presence of ices, the need to account for bouncing effects is still highly debated (e.g. Wada et al. 2011), and we do not consider it in this work.

4.4.2 Different gap extents in the dust and the gas

The presence of a planetary or sub-stellar companion has been suggested in many studies to explain the properties of transition disks. However, studies based on hydrodynamical simulation of gap opening in a gaseous disk have shown that a single planet could not open the large gap inferred from spatially resolved millimeter observations (e.g. Dodson-Robinson & Salyk 2011; Zhu et al. 2011). Most studies in fact consider a maximum radius for the gap of 5 Hill radii. According to the definition of the Hill radius, the increase of the planet mass does not produce a significant widening of the gap, and none of these models with a single planet can reproduce the observed characteristics of transition disks. In this study, we include for the first time the modelization of dust growth and evolution, in addition to the hydrodynamical simulations. We predict grain size distributions (and therefore brightness distributions) and show that the gap edges are different in dust and gas, and that therefore the extent of the gap due to a single planet is larger than expected based on gas simulations. We demonstrate in Sect. 4.2 that for a given planet, dust particles are trapped further out than the location of the edge of the gap in the gas. For example, in the specific case of a 15 $M_{\rm Jup}$ planet at 20 AU, the outer edge for the gas would be located at 37 AU, while the dust ring would be at 54 AU.

For $M_p \geq 5\ M_{\rm Jup}$, the density waves produced by the planet are still changing with time after few thousands orbits. Kley & Dirksen (2006) showed that the disk becomes eccentric with the presence of a planet with a mass $M_p > 3M_{\rm Jup}$ (for a constant viscosity given by $\nu = 10^{-5}$), which may cause a

change in the equilibrium state. However, the disk precesses slowly enough that the eccentric pattern appears to be nearly stationary, and for a critical mass of 5 $M_{\rm Jup}$, the eccentricity of the disk reaches a threshold. In fact, we demonstrated in Sect. 4.2.2 that for 1 and 3 $M_{\rm Jup}$ the dust would accumulate at 7 r_H from the location of the planet r_p, and at 10 r_H from r_P for 5, 9 and 15 $M_{\rm Jup}$. We attribute this difference in the locations of the zero point of the pressure gradient to the fact that the disk becomes eccentric for planets whose mass is higher than 3 $M_{\rm Jup}$. As a result, we have the pressure maximum further away for more massive planets, when the disk is eccentric, than for less massive planets.

4.4.3 The inner disk

Near-infrared excesses are measured in some transition disks (sometimes called pre-transition disks), and indicate the presence of dust close to the star, that can be spatially resolved in a few cases (e.g., Olofsson et al. 2011; Benisty et al. 2010; Pott et al. 2010). Besides, these objects show signs of on-going accretion (see e.g Espaillat et al. 2007). In this work, we do not treat the inner disk because our prescription for it is not accurate. In order to have self-consistency between gas hydrodynamical simulations and dust evolution models, we considered for the kinematic viscosity $\nu = \alpha\, c_s\, h$. With this viscosity and the two considered assumptions for the gas density profiles, the accretion rate $\dot{M} = 3\,\pi\,\nu\,\Sigma$ is independent of the radius. With the disk and stellar parameters considered for the two cases (Tables 4.1 and 4.2), $\dot{M}$ is of the order of $\sim 10^{-9}\ M_\odot\ yr^{-1}$, about an order of magnitude lower than the measured values in some transitional disks ($\sim 10^{-8}\ M_\odot\ yr^{-1}$; Calvet et al. (2005); Espaillat et al. (2007)). The low model value implies that even considering open boundary conditions, the gas surface density, in both inner and outer regions, only slightly decreases over the 1000 orbits (Fig. 4.1). In addition, the insertion of a very massive planet in the disk leads to strong density waves that may lead to unrealistic effects at the inner boundary (e.g., Crida & Morbidelli 2007). Therefore, our prescription for the inner disk is not accurate.

Besides, it is important to notice that inside the ice-line the absence of ices can change our results. In fact, according to laboratory experiments, the fragmentation velocity varies with the material properties (e.g. Gundlach et al. 2011). In the presence of ices, the fragmentation velocity reaches a value of $v_f \sim$ 1000cm s^{-1}, the value that we consider for the outer disk. However, this threshold decreases in the inner AUs, inside the ice-line. This directly impacts the maximum particle size (Eq. 4.4).

Finally, the radial drift in our model leads to empty the inner disk in

timescales that can be shorter than the age of some transition disk with NIR excess (e.g., HD100546). Replenishment from the outer disk with small grains passing through the gap, or from planetesimal collisions (Krijt & Dominik 2011) is needed.

4.5 Summary and conclusions

The sub-Keplerian radial velocity of the gas in protoplanetary disks makes millimeter-size particles in the outer regions of the disk exposed to a rapid inward drift, implying that they migrate towards the star on timescales shorter than a million years. Therefore, in planet formation, rapid inward drift is one of the main issues with models to form planetesimals. The idea of the presence of pressure bumps in protoplanetary disks has been proposed as a solution to stop the rapid inward drift. With the presence of a massive planet in a disk, a pressure bump is created in the outer edge of the cleared gap. Particles may experience a positive pressure gradient and as a result, do not drift anymore and not experience the high-velocity collisions due to relative radial and azimuthal drift. Nevertheless, particles can still fragment due to turbulence motion, and the resulting micron-size particles are less easily trapped and they can finally drift inwards.

Some transition disks reveal gaps that can result from the presence of a massive planet, making them potentially interesting laboratories for studying dust growth under the favorable circumstances of having a significant pressure bump. In this work, we combine two-dimensional hydrodynamical simulations for the gas with one-dimensional coagulation/fragmentation dust evolution models, to study how dust evolves in a disk which gas density has been disturbed by a massive planet.

We investigate the influence of the disk geometry, turbulence and planet mass on the potential trapping of particles. The disk geometry does not have a significant effect on the gap opening process. For a 1 $M_{\rm Jup}$ planet, there is an important influence of the α turbulence parameter on the depth of the gap and has important consequences for the trapping of particles. Unlike the case of $\alpha = 10^{-2}$, with $\alpha = 10^{-3}$, the particles are trapped at a distance of $\sim$ 0.5 r_p from the planet position r_p. While the gas gap has a radius of $\sim$ 0.35 r_p (or 5 Hill radii), the dust is retained at a further distance. Without considering turbulence mixing for the dust dynamics would produce trapping of particles for certain sizes regardless of α value provided that the pressure gradient is positive. In the case of 9 $M_{\rm Jup}$ planet, the gap depth is independent of the turbulence and as a consequence the pressure gradient behaves similarly for all α values. The dust particles are trapped at a distance of 1.4 r_p from the

planet orbit r_p. The planet mass strongly influences the location where the dust is retained and the width of the dust bump.

Observations at millimeter wavelengths reveal some transition disks with very wide gaps. We show that the location where the dust piles up does not coincide with the gap outer edge in the gaseous disk. This mismatch suggests that multiple planets may not necessarily be needed to account for the observed large opacity holes. We reproduce the main observed features of the disk around LkCa15, in which a companion was recently detected. Reproducing asymmetric features in the disk, such as the ones found in HD135344B (Brown et al. 2009) is subject of future work, as they will be well detectable with ALMA.

Chapter 5

Lopsided dust rings in transition disks

Based on the paper by Birnstiel, T., Dullemond C. P, ***Pinilla P.****, A&A 550, L8*

If we want to test by observations whether the scenario of particle trapping actually occurs in nature, we are faced with a problem. The terrestrial planet-forming region around a pre-main sequence star is usually too small on the sky to be spatially sufficiently resolved to test this trapping scenario. Moreover, the optical depth of this inner disk region is likely to be too large to be able to probe the mid-plane region of the disk. Fortunately, what constitutes the "meter-size drift-barrier" at 1 AU is a "centimeter-size drift-barrier" at ~ 50 AU. Those disk regions are optically thin at millimeter (mm) wavelength and particles in the mm size range can be spectroscopically identified by studying the mm spectral slope (Testi et al. 2001; Natta et al. 2004; Ricci et al. 2010a,b). So the goal that has been pursued recently is to identify observational signatures of dust particle trapping of millimeter-sized particles in the outer regions of disks, as a proxy of what happens in the unobservable inner regions of the disk (Pinilla et al. 2012a,b). The chapter 4 suggests that the huge mm continuum rings observed in most of the transition disks (Piétu et al. 2006, Brown et al. 2008, Hughes et al. 2009, Isella et al. 2010b, Andrews et al. 2011a), may in fact be large global particle traps caused by the pressure bump resulting from, for example, a massive planet opening up a gap.

In previous chapters, we have focused on the intermediate - scale (zonal-flow-type) and the large-scale (global) pressure bumps, simply because current capabilities of mm observatories (including ALMA) are not yet able

to resolve small-scale structures such as vortices. The vortex trapping scenario thus appears to remain observationally out of reach. However, a closer look at the mm maps of transition disks suggest that some of them may exhibit a deviation from axial symmetry. For instance, the observations presented in Mayama et al. (2012) or the mm images of Brown et al. (2009) suggests a lopsided banana-shaped ring instead of a circular ring. Regály et al. (2012) proposed that these banana-shaped rings are in fact a natural consequence of mass piled up at some obstacle in the disk. Once the resulting ring becomes massive enough, it becomes Rossby-unstable and a large banana-shaped vortex is formed that periodically fades and re-forms with a maximum azimuthal gas density contrast of a factor of a few. Regály et al. (2012) showed that this naturally leads to lopsided rings seen in mm wavelength maps (see also earlier work by Wolf & Klahr 2002) on radiative transfer predictions of observability of vortices with ALMA). The formation of such Rossby-wave induced vortices was previously demonstrated by Lyra et al. (2009), who showed that they may in fact (when they are situated much farther inward, in the planet forming region) lead to the rapid formation of planetary embryos of Marsmass. Sándor et al. (2011) subsequently showed that this scenario may rapidly produce a 10 Earth-mass planetary core.

The goal of the current chapter is to combine the scenario of forming a lopsided gas ring (e.g., Regály et al. 2012) with the scenario of particle trapping and growth presented by Pinilla et al. (2012b). In Sect. 5.1 we will outline the physical effects involved and derive analytical solutions to the dust distribution along the non-axisymmetric pressure bump [1] and in Sect. 5.2 we will test the observability of these structures in resolved (sub-)mm imaging and in the mm spectral index. Our findings will be summarized in Sect. 5.3.

5.1 Analytical model

Dust particles embedded in a gaseous disk feel drag forces if they move relatively to the gas. The radial and azimuthal equations of motion have been solved, for example, by Weidenschilling (1977) or Nakagawa et al. (1986) for the case of an axisymmetric, laminar disk. It was found that particles drift inward towards higher pressure. In this chapter we will focus on the case where a non-axisymmetric structure has formed a long-lived, non-axisymmetric pressure maximum in the disk. This pressure maximum is able to trap inward-spiralling dust particles. As was done in the aforementioned works, we can solve for a stationary drift velocity, but contrary to the calculations of Nakagawa et al. (1986), the *radial* pressure gradient is zero at

[1] This analytical model was mainly developed by T. Birnstiel

the pressure maximum while the *azimuthal* pressure gradient can be different from zero. This leads again to a systematic drift motion of the dust particles towards the pressure maximum, but now in azimuthal instead of in radial direction.

The equations of motion in polar coordinates relative to the Keplerian motion become (see Nakagawa et al. 1986)

$$\frac{\partial u_{\mathrm{d},r}}{\partial t} = -A\,\rho_{\mathrm{g}}(u_{\mathrm{d},r} - u_{\mathrm{g},r}) + 2\Omega_{\mathrm{k}} u_{\mathrm{g},\phi} \tag{5.1}$$

$$\frac{\partial u_{\mathrm{d},\phi}}{\partial t} = -A\,\rho_{\mathrm{g}}(u_{\mathrm{d},\phi} - u_{\mathrm{g},\phi}) - \frac{1}{2}\Omega_{\mathrm{k}} u_{\mathrm{d},r} \tag{5.2}$$

$$\frac{\partial u_{\mathrm{g},r}}{\partial t} = -A\,\rho_{\mathrm{d}}(u_{\mathrm{g},r} - u_{\mathrm{d},r}) + 2\Omega_{\mathrm{k}} u_{\mathrm{g},\phi} \tag{5.3}$$

$$\frac{\partial u_{\mathrm{g},\phi}}{\partial t} = -A\,\rho_{\mathrm{d}}(u_{\mathrm{g},\phi} - u_{\mathrm{d},\phi}) - \frac{1}{2}\Omega_{\mathrm{k}} u_{\mathrm{g},r} - \frac{1}{r\,\rho_{\mathrm{g}}}\frac{\partial P}{\partial \phi}, \tag{5.4}$$

where $u_{\mathrm{d},r}$ and $u_{\mathrm{d},\phi}$ are the r and ϕ components of the dust velocity, respectively, $u_{\mathrm{g},r}$ and $u_{\mathrm{g},\phi}$ the r and ϕ components of the gas, Ω_{k} the Keperian frequency, P the gas pressure, and ρ_{d} and ρ_{g} the dust and gas densities; A denotes the drag coefficient (see Nakagawa et al. 1986, Eqs. 2.3 and 2.4). Solving the above equations for the velocity along the ϕ direction at the mid-plane ($z = 0$) gives

$$u_{\mathrm{d},\phi} = \frac{1}{\mathrm{St} + \mathrm{St}^{-1}\,(1+X)^2}\,\frac{1}{\rho_{\mathrm{g}}\,V_{\mathrm{k}}}\frac{\partial P}{\partial \phi}, \tag{5.5}$$

where $X = \rho_{\mathrm{d}}/\rho_{\mathrm{g}}$ is the dust-to-gas ratio, V_{k} the Keplerian velocity, and the Stokes number[2] is given by

$$\mathrm{St} = \frac{\rho_{\mathrm{s}}\,a}{\rho_{\mathrm{g}}\,c_{\mathrm{s}}\,\sqrt{8/\pi}}\,\Omega_{\mathrm{k}}, \tag{5.6}$$

with ρ_{s} as internal density of the dust, particle radius a, and the isothermal sound speed c_{s}. Dust is advected with the velocity given in Eq. 5.5, but it is also turbulently stirred. Together, the evolution of the dust density along the ring is then described by

$$\frac{\partial \rho_{\mathrm{d}}}{\partial t} = \frac{\partial}{\partial y}\left(\rho_{\mathrm{d}}\,u_{\mathrm{d},\phi}\right) - \frac{\partial}{\partial y}\left(D\,\rho_{\mathrm{g}}\,\frac{\partial}{\partial y}\left(\frac{\rho_{\mathrm{d}}}{\rho_{\mathrm{g}}}\right)\right), \tag{5.7}$$

[2]St =1 typically corresponds to particles of mm to cm sizes in the outer disk. For typical disk conditions $a \simeq 0.4\,\mathrm{cm}\cdot\mathrm{St}\cdot\Sigma_{\mathrm{g}}/1\,\mathrm{g\,cm^{-2}}$.

where $y = r\,\phi$ is the coordinate along the ring circumference. We use a dust diffusion coefficient D according to Youdin & Lithwick (2007), $D = D_{\rm gas}/(1+\mathrm{St}^2)$, where we assume the gas diffusivity to be equal to the gas viscosity, taken to be $\nu = \alpha_{\rm t}\, c_{\rm s}^2/\Omega_{\rm k}$, with $\alpha_{\rm t}$ as the turbulence parameter (see Shakura & Sunyaev 1973). Equation 5.7 can be integrated forward in time numerically, but assuming that the turbulent mixing and the drift term have reached an equilibrium, and also assuming a low dust-to-gas ratio, we can analytically solve for the dust density in a steady-state between mixing and drifting, which yields

$$\rho_{\rm d}(y) = C \cdot \rho_{\rm g}(y) \cdot \exp\left[-\frac{\mathrm{St}(y)}{\alpha_{\rm t}}\right], \tag{5.8}$$

where C is a normalization constant and $\mathrm{St}(y)$ is the Stokes number which depends on y via the changes in gas density. Equation 5.8 thus predicts the distribution of dust for any given profile of the gas density $\rho_{\rm g}$. The contrast between the position of the azimuthal pressure maximum and its surrounding then gives

$$\frac{\rho_{\rm d}^{\rm max}}{\rho_{\rm d}^{\rm min}} = \frac{\rho_{\rm g}^{\rm max}}{\rho_{\rm g}^{\rm min}} \exp\left[\frac{\mathrm{St}^{\rm min} - \mathrm{St}^{\rm max}}{\alpha_{\rm t}}\right], \tag{5.9}$$

which is plotted in Fig. 5.1. The Stokes numbers at the pressure maximum and minimum are $\mathrm{St}^{\rm max}$ and $\mathrm{St}^{\rm min}$ (note: $\mathrm{St}^{\rm max} < \mathrm{St}^{\rm min}$). It can be seen that once the particle's Stokes number becomes larger than the turbulence parameter $\alpha_{\rm t}$, the dust concentration becomes much stronger than the gas concentration. However, the time scales on which these concentrations are reached can be significant. To get an estimate for this time scale, we compare the advection time scale $t_{\rm adv} = L/u$ and the diffusion time scale $t_{\rm diff} = L^2/D$ with velocity u and length scale L. The ratio of these time scales is known as the Péclet number Pe and using Eq. 5.5, can be written as

$$\mathrm{Pe} = \frac{t_{\rm diff}}{t_{\rm adv}} = \frac{\mathrm{St}}{\alpha_{\rm t}} \frac{L}{\rho_{\rm g}} \frac{\partial \rho_{\rm g}}{\partial y} \simeq \frac{\mathrm{St}}{\alpha_{\rm t}} \frac{\Delta \rho_{\rm g}}{\rho_{\rm g}}. \tag{5.10}$$

It describes the relative importance of advection and diffusion and confirms that dust accumulations occur only for particles with $\mathrm{St} \gtrsim \alpha_{\rm t}$, because otherwise diffusion dominates over advection which means that variations in the dust-to-gas ratio are being smeared out. It also shows that for those large particles the advection time scale is the shorter one, thus setting the time scale of the concentration process, which can be written as

$$t_{\rm adv} = \frac{\pi^2}{\delta \mathrm{St}} \left(\frac{H}{r}\right)^{-2} \frac{1}{\Omega_{\rm k}}, \tag{5.11}$$

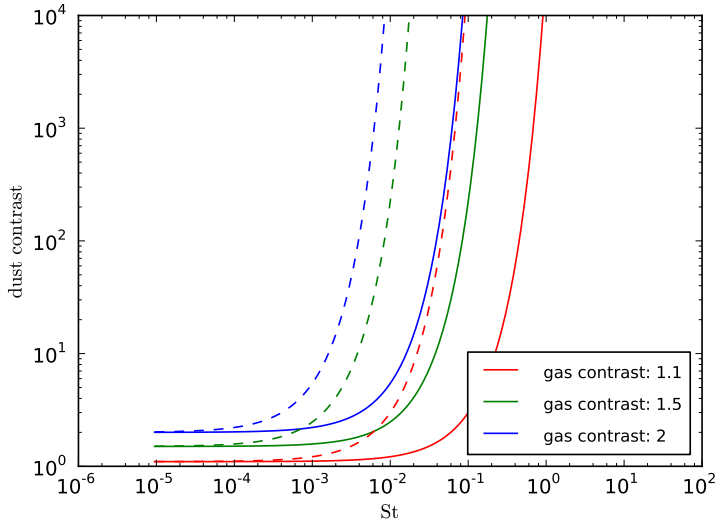

Figure 5.1: Contrast between the dust density in the azimuthal maximum and its surroundings for different gas density contrasts ($\rho_\mathrm{g}^\mathrm{max}/\rho_\mathrm{g}^\mathrm{min}$) and Stokes numbers, as derived in Eq. 5.9. Turbulence parameters are $\alpha_\mathrm{t} = 10^{-2}$ (solid) and $\alpha_\mathrm{t} = 10^{-3}$ (dashed).

where $H = c_\mathrm{s}/\Omega_\mathrm{k}$ is the pressure scale height, and we have used a mean velocity $\overline{u} = \frac{1}{\pi}\left|\int_0^\pi u\,\mathrm{d}\phi\right| = \frac{c_\mathrm{s}^2}{\pi V_\mathrm{k}}\delta\mathrm{St}$, with

$$\delta\mathrm{St} = \left|\mathrm{arccot}\left(\mathrm{St}^\mathrm{min}\right) - \mathrm{arccot}\left(\mathrm{St}^\mathrm{max}\right)\right|, \tag{5.12}$$

which for $\mathrm{St} < 1$ simplifies to $\delta\mathrm{St} = \mathrm{St}^\mathrm{min} - \mathrm{St}^\mathrm{max}$. Furthermore, we define the pressure maximum and minimum to be at $\phi = 0$ and $\phi = \pi$, respectively. As an example, at 35 AU, for $H/r = 0.07$, a Stokes number of 0.2, and a gas density contrast of $\rho_\mathrm{g}^\mathrm{max}/\rho_\mathrm{g}^\mathrm{min} = 2$, the time scale is 3×10^5 years, but could be as short as 10^2 orbits for optimal conditions. Any gas structure therefore has to be long-lived to cause strong asymmetries in the dust, making the asymmetries caused by a planet or long-lived vortices the best candidates (Meheut et al. 2012). If such an accumulation is formed and the gas asymmetry disappears, it still takes t_diff to "remove" it, which at 35 AU is of the order of Myrs. It remains to be shown whether short-lived, but reoccurring structures like zonal flows are able to induce strong dust accumulations.

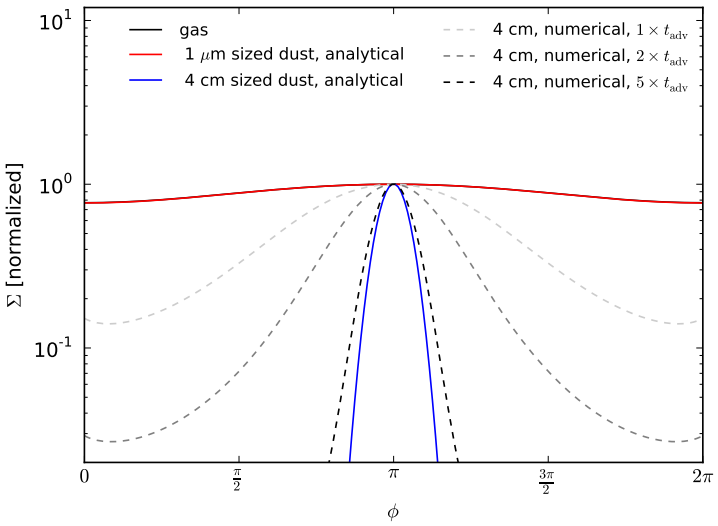

Figure 5.2: Azimuthal steady-state solutions for small dust grains (red line) and large dust grains (blue line) for a given sinusoidal gas profile (black line, identical with red line). Dashed lines show numerical solutions at 1, 2, and 5 advection time scales.

5.2 Simulated Observations

In the following, we will evaluate whether the dust structures we expect would be observable in resolved mm images of ALMA. We used the results of Pinilla et al. (2012b) for the radial profile of the gas surface density $\overline{\Sigma}_{\rm g}(r)$ and temperature $T(r)$. These simulations represent a disk of mass $M_{\rm disk} = 0.05\,M_{\odot}$ around a solar mass star with a 15 Jupiter-mass planet at 20 AU. For simplicity, as two-dimensional gas surface density we used

$$\Sigma_{\rm g}(r,\phi) = \overline{\Sigma}_{\rm g}(r) \cdot \left[1 + A(r) \cdot \sin\left(\phi - \frac{\pi}{2}\right)\right] \tag{5.13}$$

$$A(r) = \frac{c-1}{c+1} \cdot \exp\left[-\frac{(r-R_{\rm s})^2}{2\,H^2}\right], \tag{5.14}$$

where $c = \Sigma_{\rm g,max}/\Sigma_{\rm g,min}$ is the largest contrast of the gas surface density, taken to be 1.5 and $R_{\rm s}$ is the position of the radial pressure bump. The dust size distribution $\Sigma_{\rm d}(r,a)$ was also taken from the simulations of Pinilla et al. (2012b) and distributed azimuthally using the analytical solution from Eq. 5.8 (see Fig. 5.2). We also confirmed the analytical solution and time scales by solving Eq. 5.7 numerically, as shown in Fig. 5.2. Strictly speaking,

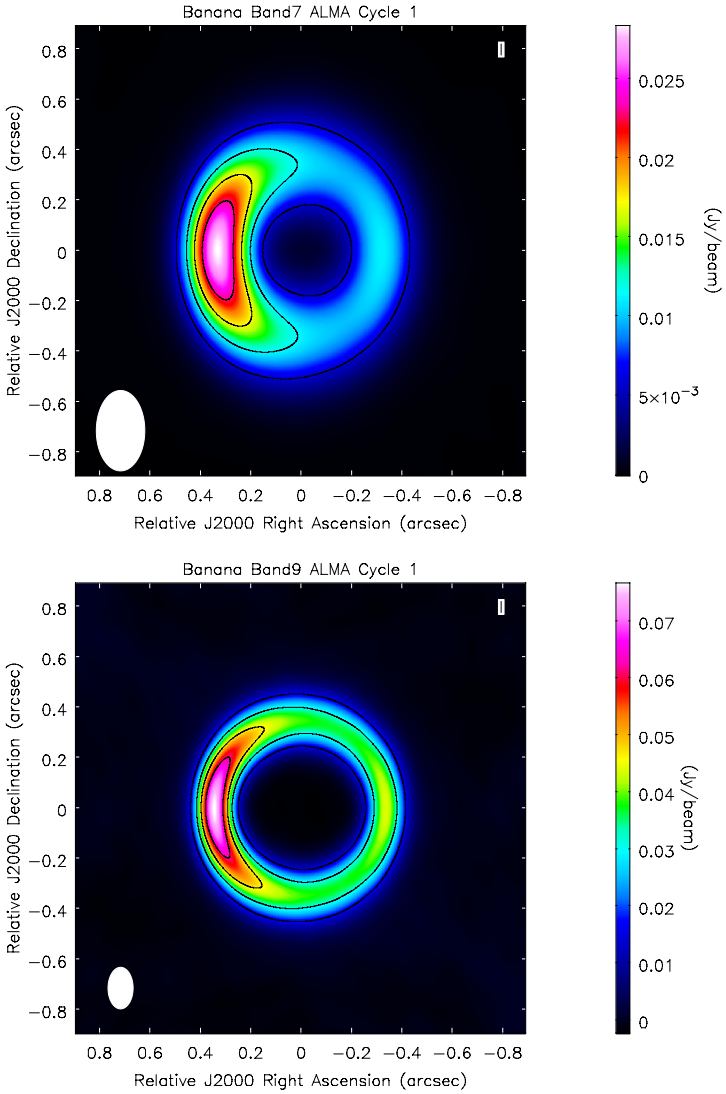

Figure 5.3: *Top panel:* ALMA simulated images at 345 GHz with an observation time of 2 hours. The total flux of the source is 0.13 Jy and the contour lines are at 2, 4, 6, and 8 times the rms of 0.22 mJy. *Bottom-Panel:* ALMA simulated images at 675 GHz with an observation time of 2 hours. The total flux of the source is 0.71 Jy and the contour lines are at 2, 4, 6, and 8 times the rms of 0.87 mJy.

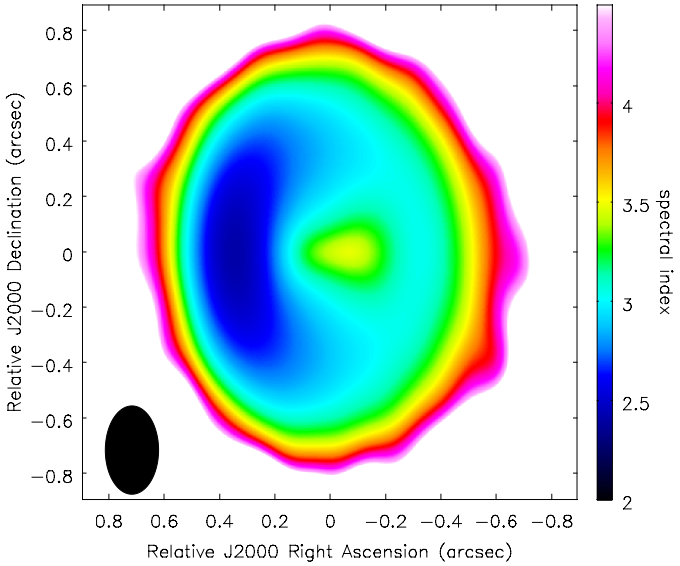

Figure 5.4: Spectral index $\alpha_{\rm mm}$ using simulated images at bands 7 and 9. The antenna configuration was chosen such that the angular resolution is similar for both bands ($\sim$ 0.16", 22 AU at 140 pc).

this analytical solution only holds at the position of the radial pressure bump, but since most of the mm emission comes from the large grains which in the simulations of Pinilla et al. (2012b) are trapped near the radial pressure maximum, this should be a reasonable approximation. Full 2D simulations will be needed to confirm this and to investigate the effects of shear.

To compare directly with current ALMA observations, we calculated the opacities for each grain size at different wavelengths and assumed spherical silicate grains with optical constants for magnesium-iron grains from the Jena database[3]. The continuum intensity maps were calculated assuming that in the sub-mm regime most of the disk mass is concentrated in the optically thin region. We assumed the same stellar parameters as in Pinilla et al. (2012b), azimuthally constant temperature $T(r)$, typical source distances (d = 140 pc), and zero disk inclination. We ran ALMA simulations using CASA (v. 3.4.0) at 345 GHz (band 7) and 675 GHz (band 9), shown in Fig. 5.3. We considered 2 hours of observation, the most extended configuration that is currently available with Cycle 1, generic values for thermal and atmospheric noises, and a bandwidth of $\Delta\nu$ = 7.5 GHz for continuum. At these two different frequencies it is possible to detect and resolve regions

[3]http://www.astro.uni-jena.de/Laboratory/Database/databases.html

where the dust is trapped creating a strong azimuthal intensity variation.

The spectral slope $\alpha_{\rm mm}$ of the spectral energy distribution $F_\nu \propto \nu^\alpha$ is directly related to the dust opacity index at these long wavelengths (e.g., Testi et al. 2003), and it is interpreted in terms of the grain size ($\alpha_{\rm mm} \lesssim 3$ implies mm sized grains). With the simulated images in Fig. 5.3, we compute the $\alpha_{\rm mm}$ map (Fig. 5.4), considering an antenna configuration that provides a similar resolution of ~ 0.16" ($\sim$ 22AU at 140 pc) for each band. This resolution is enough to detect $\alpha_{\rm mm}$ variations along the azimuth, confirming that those are regions where dust accumulates and grows due to the presence of an azimuthal pressure bump.

5.3 Summary and conclusions

We have shown that weak, but long-lived azimuthal asymmetries in the gas density can cause very efficient accumulation of dust at the position of the azimuthal pressure maximum. We have derived analytical steady-state solutions for the dust distribution for any given azimuthal gas density distribution and the time scales on which these distributions develop. Good agreement has been found between the solutions and numerical simulations.

For this dust concentration mechanism to work, particles must grow to sufficiently large sizes (St $> \alpha_{\rm t}$) such that the azimuthal drift becomes stronger than the turbulent diffusion. This typically corresponds to particles of sub-mm to cm sizes. The strong concentration of the largest grains leads to a size-sorting which is observable via low spectral indices at mm wavelengths and also in lopsided banana-shaped structures in resolved (sub-)mm images. Finding the size range where the bifurcation between concentration and diffusion happens would put constraints on the turbulence strength and the local gas density of the disk.

Chapter 6

Asymmetric transition discs: Vorticity or eccentricity?

Based on the paper by Ataiee S.; ***Pinilla, P.****; Zsom, A; Dullemond, C. P.; Dominik, C.; Ghanbari, J., A&A 553, L3*

Most models of protoplanetary disks which aimed at fitting observations are axisymmetric (e.g. D'Alessio et al. 1998; Pinte et al. 2006; Woitke et al. 2009; Min et al. 2011) because until recently, with a few exceptions, observations did not have enough spatial resolution and sensitivity to detect strong deviations from axial symmetry in these disks. Recent observations, however, unveil some non-axisymmetric structures in protoplanetary disks and have changed the situation. Scattered light images of a number of disks around Herbig Ae/Be stars reveal complex structures such as spirals and rings (e.g. Fukagawa et al. 2004; Oppenheimer et al. 2008; Muto et al. 2012). Millimeter continuum maps show asymmetries as well (Piétu et al. 2005). Spatially resolved mm maps consistently show that transitional disks -protoplanetary disks with a strong deficiency of dust inward of a few AU or in other words disks with huge inner hole (Andrews et al. 2011a)- appear as rings on the sky often with a lumpy structure along the ring (Brown et al. 2009; Casassus et al. 2013). Near-infrared scattered light images of some of these disks also show clearly non-axisymmetric structures (Rameau et al. 2012). Altogether, non-axisymmetry turns out to be a regular phenomenon in disks, particularly in transition disks.

Recent theoretical work has been aimed to explain the origin and physical processes involved with these asymmetries (for example the model described in Chapter 5). For instance, Regály et al. (2012) and Lyra & Mac Low (2012) have shown that if gas accumulates at some location in the disk, such

as a sharp jump in viscous stress or resistivity, the gas "bump" can become Rossby unstable and produce large anti-cyclonic vortices. In these models, initially, a number of small vortices are generated and they eventually merge to form a giant banana-shaped vortex, or in other words, a lopsided ring. These vortices could also form in the edge of a gap produced by a massive planet. As the planet opens up a gap in the disk and prevents (or at least hampers) the gas flowing toward the star, the gas accumulates in the outer edge of the gap, becomes unstable and produces vortices (Koller et al. 2003; Li et al. 2005; De Val-Borro et al. 2007; Lin & Papaloizou 2011; Lin 2012). However, it is less clear how long these vortices can survive (Meheut et al. 2012).

In addition, a massive enough planet can make its gap eccentric and therefore produce another kind of large asymmetry. Kley & Dirksen (2006) showed that a planet with the mass beyond $3M_{\rm Jup}$ in a disk with viscosity $\alpha \approx 4 \times 10^{-3}$, is able to make the disk eccentric which means the gas parcels in the disk are on elliptic orbits. Due to Kepler laws, the gas velocities at the apocenter of the elliptic orbits are lower than at the pericenter. As a result of this "traffic jam", for nearly constant mass flux (ρu_ϕ) along the ellipse, the density ρ is expected to be higher at apocenter than at pericenter. This leads to a lopsided disk structure too.

The question arises here is how the basic differences between two models, vortex and eccentric disk, can affect the observational features of transition disks. One important difference between the eccentric structure and vortex refers to the density contrast. A higher contrast is achievable if the planet makes the disk more eccentric, in which case the eccentricity of the orbit presumably becomes apparent in the image. Another notable difference is that the eccentric "traffic jam" is not comoving with the fluid but is instead nearly stationary in the inertial frame (Kley & Dirksen 2006). In simple words, similar to galactic spiral arms, the mass flows in from one side and flows out from the other side. As a result, this kind of asymmetry can not trap particles and the dust asymmetry would be similar to the gas. This has been confirmed by Hsieh & Gu (2012) which shows that in an eccentric disk with a $\sim 5M_{\rm Jup}$ planet, the dust density follows the gas density pattern. Instead, anticyclonic vortices, which are local pressure "bumps", act as dust traps (e.g Barge & Sommeria 1995; Klahr & Henning 1997; Lyra et al. 2009). The dust trapping may lead to an even stronger azimuthal asymmetry in the dust continuum (Birnstiel et al. 2013).

The objective of this chapter is to study the observational appearance of asymmetries caused by a planet and answer the question that if we observe a transition disk and we see a large-scale asymmetric ring, if this is due to a vortex or an eccentric disk? We aim to find out under which conditions

eccentricities or vortices are the dominant sources of azimuthal asymmetries.

6.1 Method and simulations

Both a vortex and an eccentric disk, which cause an asymmetry in a gas disk, can be produced by a massive planet and affected by the physical parameters of the disk in the same manner, although they have different formation mechanisms. In Sec. 6.1.1 we briefly diskuss the formation of these asymmetries and the parameters that can affect them, afterwards, we describe our numerical methods.

6.1.1 Vortex and eccentric shape

A large-scale vortex can be created by Rossby wave instability (RWI) and live long under suitable conditions. RWI can be considered as the rotational analogy of the Kelvin-Helmholtz instability (Lovelace et al. 1999). Li et al. (2000) studied the condition of RWI formation in a disk with either a density bump or a density jump and concluded that a 10-20% surface density change over a radial length scale of about the thickness of the disk is enough to perturb the rotational velocity of the gas and produce the RWI. Wherever this condition is satisfied in the disk, the instability occurs. De Val-Borro et al. (2007) showed that not only planets as massive as Neptune and Jupiter are able to excite the RWI and generate vortices on the both edges of the gap, but also the vortices can live longer than 100 orbits. A 3D study by Meheut et al. (2012) shows that RWI can survive for long timescales ($\sim$ hundred orbits) and they explain that, as long as the overdensity is sustained permanently by an external driving force such as (in our case) a planet, the vortex does not decay and is not destroyed by mechanisms such as elliptical instability. Therefore, parameters like viscosity and planet mass, that control the accretion rate through the gap and consequently the density gradient in the outer edge of the gap, can influence the formation and the lifetime of the vortex.

An eccentric gap is another by-product of gap formation by a massive planet and is affected by similar parameters which influence a vortex. Kley & Dirksen (2006) investigated the response of disk eccentricity upon changing planet mass and physical parameters of the disk such as viscosity and temperature. They showed that if the planet is massive enough to clear up a gap until the outer 1:2 Lindblad resonance, the disk becomes eccentric. Like vortex formation, the eccentric structure is also altered by viscosity and planet mass. High viscosity and lower planet mass narrow the gap and re-

duce eccentricity of the disk. We run 132 hydrodynamical simulations to study the effects of these parameters on the maintaining of a vortex and/or an eccentric feature.

6.1.2 Hydro-simulations

We use locally isothermal version of the FARGO code (Masset 2000). Our basic model is a two-dimensional viscous disk with a massive planet which opens a gap. We alter viscosity and mass of the planet to see how they affect the asymmetric features. We perform 12 runs in inertial frame for 1000 orbits. To distinguish between a vortex and an eccentric shape, we follow the disk surface density evolution at high time resolution. Therefore, we conduct an extra set of 10 runs per model to extend every output in each simulation for another 2 orbits saving 100 outputs during each orbit.

We consider a flared disk with aspect ratio $h = 0.05(r/r_p)^{0.25}$. Considering the aspect ratio definition $h(r) = H/r = c_s/v_K$ where c_s is the local sound speed and v_K is the Keplerian velocity, the temperature profile scales as $T \propto r^{-1/2}$. The surface density follows the relation $\Sigma = \Sigma_0\ (r/r_p)^{-1}$, with $\Sigma_0 = 2 \times 10^{-4}\ M_\star/r_p^2$ and in order to keep the disk viscously stable, we use viscosity as $\nu = \alpha c_s H$ (Shakura & Sunyaev 1973). The viscosity parameter α takes the values 10^{-2}, 10^{-3} and 10^{-4} in our models. The disk extends from $r_{\rm min} = 0.1r_p$ to $r_{\rm max} = 7.0r_p$ where r_p is the orbitals radius of the planet and is used as length scale. The disk is covered by $N_r \times N_s = 512 \times 757$ grid cells with logarithmic radial spacing. We choose this resolution to avoid the numerical issues due to high density gradient at the gap edge and to have squared cells. We use the FARGO non-reflecting boundary condition to reduce the effect of wave reflections from the boundaries.

The planet mass in our simulations gets the values $M_p = 5, 10, 15$ and $20\ M_{\rm Jup}$ with $M_{\rm Jup} = 10^{-3}M_\star$. The planet is held at $r_p = 1$ in a circular orbit. The potential of the planet ϕ is softened by the parameter $\epsilon = 0.6R_H$ to avoid a singularity:

$$\phi = -\frac{GM_p}{(r^2 + \epsilon^2)} \tag{6.1}$$

where R_H is the planet Hill radius of the planet and G is the gravitational constant.

For applying our results to the observed features of transition disks, we need planet orbital radius and mass of the star in physical units. The rest of the quantities can be calculated using these two numbers. In this work we consider a planet that orbits a solar mass star at the distance of $r_p = 20$AU.

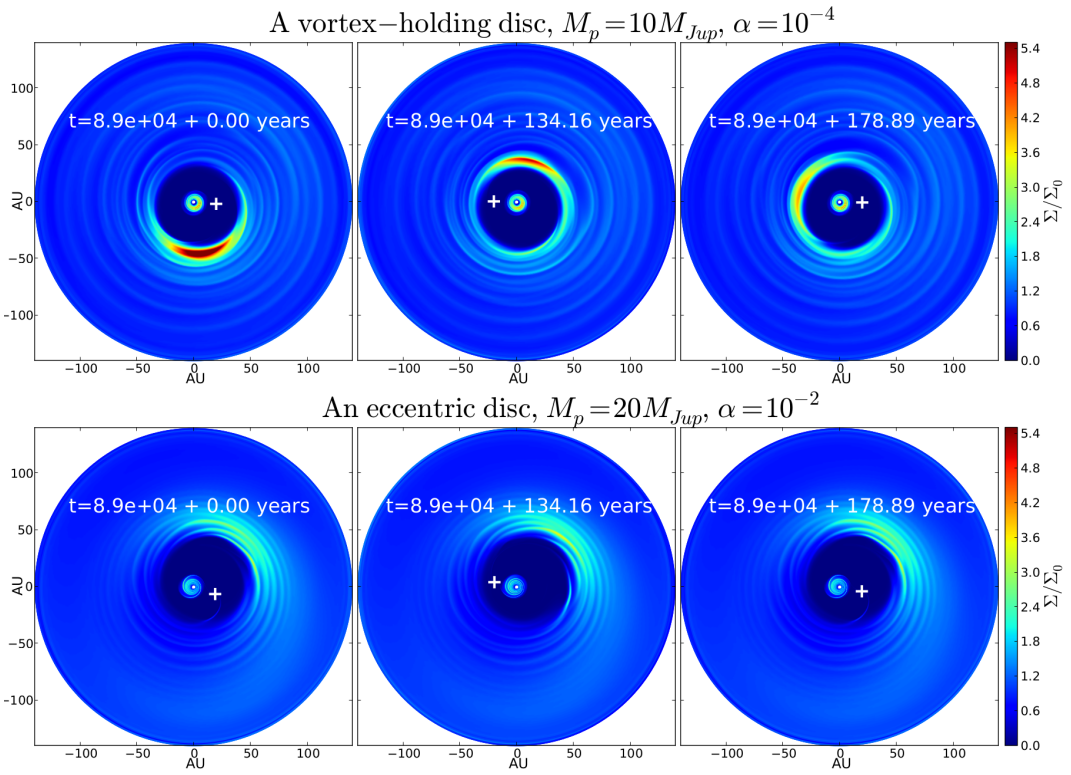

Figure 6.1: Evolution of a vortex-holding disk and an eccentric disk from 1000 orbits (left column) to 1002 orbits (right column). Top panels show how a vortex moves within two orbital time of the planet. Bottom panels show the same snapshots as the top panels but for an eccentric disk. It can clearly be seen that the eccentric feature is fixed during two planetary orbits. The crosses display the position of the planet.

Therefore, the disk extends from $r_{\rm min} = 2$AU to $r_{\rm max} = 140$AU and it has a mass of $M_{\rm disk} = 0.008 M_{\odot}$. The initial surface density Σ_0 is therefore $\Sigma_0 \sim 4.44\ (r/20{\rm AU})^{-1}{\rm g\ cm}^{-2}$.

6.1.3 Recognizing a vortex from an eccentric shape

We distinguish a vortex from an eccentric asymmetry in our hydro-simulations by checking whether the structure is fixed or co-moving with the gas in the inertial frame. While a vortex revolves around the star with the local orbital frequency, an eccentric feature is almost fixed with small precession (Kley & Dirksen 2006). Therefore, we follow the structures in all models to decide

whether the asymmetry is a vortex or an eccentric feature (Fig. 6.1).

6.1.4 Dust simulations

To compare the dust distribution between a vortex and an eccentric feature, we conduct dust simulations for the models in Fig. 6.1 [1]. We use the numerical code developed by Zsom et al. (2011) which solves the restricted three body problem for dust particles in 2D spherical coordinates taking into account gas drag that results in radial drift (for details refer to Paardekooper 2007; Zsom et al. 2011). To mimic the turbulence mixing, we allow the particles to pace every timestep in a random direction with the step-size $l = \sqrt{D_p \Delta t}$ where $D_p = \nu/(1+{\tau_s}^2)$ is the diffusion coefficient for the particles with dimensionless stopping time τ_s (see Youdin & Lithwick 2007). The viscosity ν is taken self-consistent with our hydrodynamical simulations. Since we are only interested in the dust distribution, we do not consider the dust coagulation and fragmentation. We run two sets of simulations for two particle masses 0.05 and 0.5g. These masses, in our simulations, correspond to the sizes $\sim$ 2 and $\sim$ 5mm which suffer the highest and moderate radial drift at $\sim 50AU$ respectively. We distribute 10000 dust particles with the same density profile as the gas at 1000 orbits and allow particles to evolve for 200 orbits.

6.2 Results

Figure 6.2 gives a summary of the results of our models in terms of the presence or absence of a vortex and/or an eccentricity. The horizontal and vertical axes are mass of the planet and logarithm of the α viscous parameter respectively. According to Fig. 6.2, eccentric shape is a very common feature in our models. This figure shows that a vortex can be created and survive until the end of the simulations for low viscosity, i.e. $\alpha = 10^{-4}$.

In none of the simulations with the highest viscosity parameter $\alpha = 10^{-2}$, a vortex is formed. In the model with a $5M_{\rm Jup}$ planet, a narrow circular gap is created and stays until the end of the simulations. A more massive planet $M_p = 10M_{\rm Jup}$ starts to stablish an eccentric gap from 200 orbits and succeeds to make it at 400 orbits ($\sim 3.6 \times 10^4$ years). For more massive planets, the disk becomes eccentric even at 200 orbits ($\sim 1.8 \times 10^4$ years).

For the intermediate value of the viscosity, i.e. $\alpha = 10^{-3}$, the disk passes through three stages. First a vortex appears in the disk and survives until 200-300 orbits. The longevity of the vortex greatly depends on mass of

[1] The dust simulations of this chapter were done by S. Ataiee.

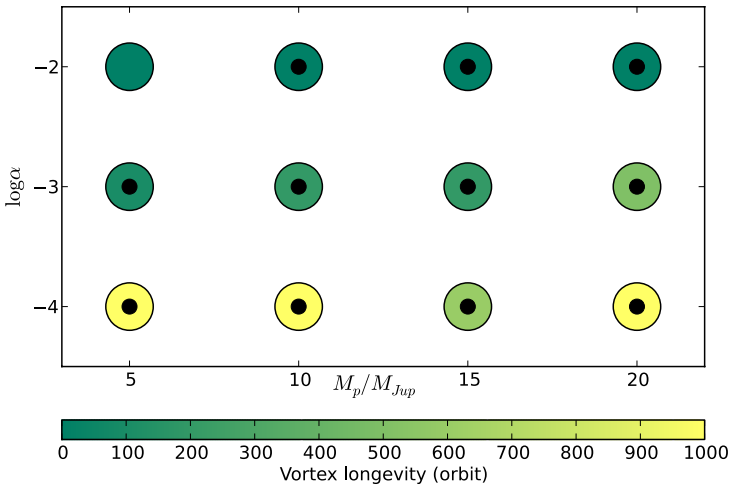

Figure 6.2: Dependency of eccentricity and vortex longevity on planet mass and viscosity. The color represents the longevity of vortices and the eccentric disks are marked by a dot. For $M_p = 15M_{\rm Jup}$ and $\alpha = 10^{-4}$, the asymmetries are extremely mixed and undistinguishable after 600 orbits.

the planet. The more massive the planet is, the longer the vortex survives. During the second stage, which lasts until orbit 800 for $M_p = 5M_{\rm Jup}$ and 500 for the rest, the features are mostly undistinguishable and mixed. Therefore, even if we observe a moving denser region or a vague asymmetry, we consider it neither as a vortex nor as an eccentric disk. Eventually the planet succeeds to reform the gap into eccentric and the disk keeps the eccentric shape until the end of the simulation.

The models with low eccentricity $\alpha = 10^{-4}$ produce the most interesting results for the vortex formation. For lower planet masses, i.e. $M_p = 5M_{\rm Jup}$ and $10M_{\rm Jup}$, the vortex is the dominant feature. Although the disk is slightly eccentric, the asymmetric density feature due to it is not high enough to be distinguished and therefore the vortex remains as the strongest asymmetry in the disk. On the other hand, the eccentric feature in the models with more massive planets $M_p = 15M_{\rm Jup}$ and $20M_{\rm Jup}$ is strong to such a degree that can mix with the vortex. Figure 6.3 shows how a vortex travels through the eccentric shape. When the both features overlap, the density contrast is the the highest.

Figure 6.4 illustrates the results of the dust simulations for the two disk models in Fig. 6.1. The first row of Fig. 6.4 shows the dust distribution for the case of the disk with the vortex. In this case, particles move toward the vortex and after 200 orbits most of the dust is accumulated in the vortex

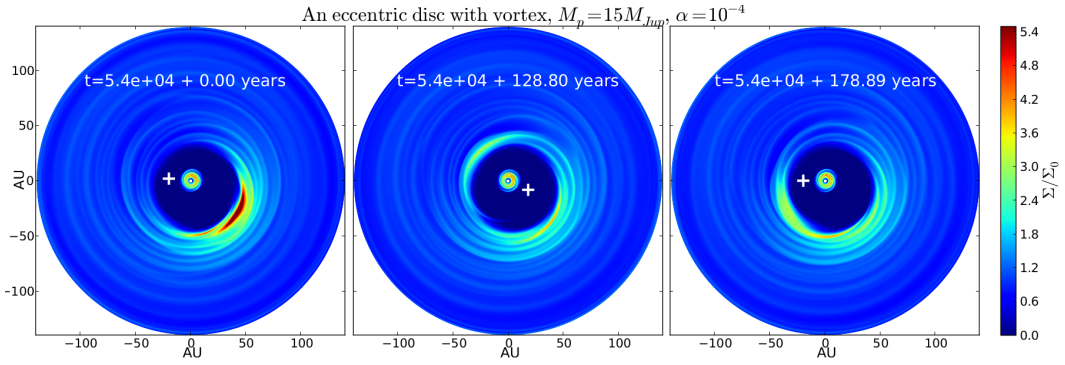

Figure 6.3: Evolution of a vortex through the eccentric shaped disk. The simulation is carried out for $M_p = 15\ M_{\rm Jup}$ and $\alpha = 10^{-4}$. The left panel shows the gas surface density at 600 orbits and the right one shows the disk after 2 orbits.

center. The middle panels of Fig. 6.4 display the the dust distribution in the eccentric case. Contrary to the vortex case, the particles are only trapped in the radial direction producing a ring which is wide due to the high diffusion ($\alpha = 10^{-2}$). After the quasi-static state is reached, no strong azimuthal asymmetry is produced. We define the *dust enhancement factor* f as:

$$f(\phi) = \frac{(M_{\rm dust}/M_{\rm gas})_{t=1019\ \rm orbits}}{(M_{\rm dust}/M_{\rm gas})_{t=1000\ \rm orbits}} \tag{6.2}$$

which is calculated for $r \in [30, 140]$AU and the azimuthal slice between ϕ and $\phi + \Delta\phi$. We plot $f(\phi)$ in the bottom panels of Fig. 6.4 to compare the dust azimuthal accumulation between our models. These plots show that the dust enhancement factor in a vortex is at least more than twice as high as the value for the eccentric case. Therefore, the vortex produces a stronger azimuthal asymmetry in a narrower azimuthal range compare to the eccentric disk.

6.3 Observational consequences

The difference between azimuthally density contrast in a vortex-holding and an eccentric disks is a very useful tool to recognize them observationally. Our results show that we need $\sim 50 \times (R_s/20AU)^{1.5}$ years (R_s is the position of the asymmetry) to distinguish an eccentric feature from a vortex using the

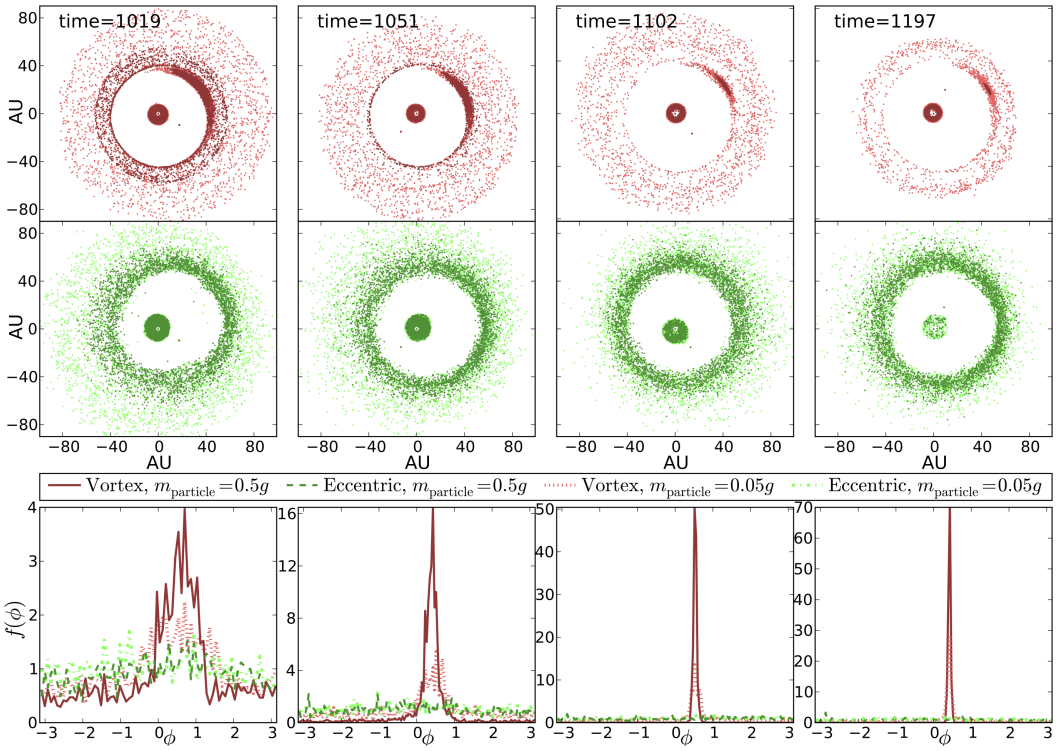

Figure 6.4: Dust distribution comparison at time=1019, 1051, 1102, 1197 orbits. We choose these snapshots because the vortex locates at the same azimuthal position of the eccentric feature and therefore we can compare the azimuthal concentration of particles more easily. The top and middle rows reflect the difference between the dust trapping in a vortex-holding disk and an eccentric disk respectively. The light and dark colors represent the 0.05g and 0.5g particles respectively. In the bottom panels, we plot the dust enhancement factor against azimuth at each corresponding snapshot.

comparison of the position of the azimuthal density variation. However, different observational features at (sub-)millimeter wavelengths are fortunately diskernible in one single snapshot. When a planet carves out a gap in a disk, particle trapping in the *radial* direction would happen for both cases (see e.g Pinilla et al. 2012b) while particle trapping in *azimuthal* direction could only happen in the vortex case. Because a "traffic jam" in an eccentric disk is not a particle trap, the azimuthal contrast in the continuum would be as high as the contrast in the gas surface density, which can reach values of $\Sigma/\Sigma_0 \sim 3$ (Fig. 6.1) and the dust azimuthal extension of the asymmetry would be similar to gas. Instead, vortices are indeed particle traps and they can be long-lived (up to 10^5 years) when very massive planets (15-20 $M_{\rm Jup}$) and moderate viscosity ($\alpha = 10^{-4}$) are able to maintain the density bumps and the RWI. Therefore, the vortices can create strong variations in the azimuthal dust distribution of millimeter particles and the asymmetry feature would be less azimuthally extended for the dust than the gas (Birnstiel et al. 2013). Hence, stronger and more compact dust azimuthal asymmetry is expected for a vortex than for an eccentric disk. The results shown in Fig. 6.4 give us a good impression of what is expected with millimeter observations with high sensitivity and angular resolution. It is important to notice that neither in a vortex nor in an eccentric case, we expect the location of the planet along its orbit to be correlated with the location of the vortex or ellipse of disks.

6.4 Conclusion

One exciting explanation of the wide gaps observed in transition disks is the interaction of a massive planet with the disk. When the planet is massive enough and moderate values for the disk viscosity are taken, two different scenarios can create azimuthally variations in the gas surface density: eccentric disks and a vortex excited by the RWI. The azimuthal contrast of the gas surface density varies for both cases and it is much higher for the vortex situation. In this case, particle trapping is possible and very high azimuthal variations are expected at millimeter wavelengths as it is currently observed with ALMA.

Chapter 7

Observational evidence for grain growth in transition disks

Based on a paper in preparation by ***Pinilla P.****, Benisty, M., Ricci, L., Isella, A. et. al.*

Observations by infrared telescopes done with e.g. *Spitzer* and *Herschel*, and by millimeter observations with radio-interferometers as SMA, EVLA or ALMA have revealed different structures in circumstellar disks surrounding young stars. Transition disks are disks that show a lack of near-infrared radiation in the spectral energy distribution (SED) which indicates that they have inner opacity holes (e.g. Piétu et al. 2006; Espaillat et al. 2010). The recent potential discoveries of a companion inside a massive disk in T Cha (Huélamo et al. 2011) and in LkCa15 (Kraus & Ireland 2011) promote the idea that the holes in transition disks are the result of a planet or multiple planets interacting with the disk. Hydrodynamical simulations of planet-disk interactions have been explored for already several years (e.g. Lin & Papaloizou 1979; Paardekooper & Mellema 2004). The presence of a massive planet in a circumstellar disk not only affects the surrounding gas, but also the dust distribution in the disk. A planet of 1 $M_{\rm Jup}$ opens a gap in a laminar disk and depending on the particle size and the shape of the gap, gas and dust can flow through a gap (Rice et al. 2006; Zhu et al. 2012; Pinilla et al. 2012b). In transition disks, the overall dust distribution is therefore unknown, and observations at different wavelengths with high sensitivity and resolution are crucial to understand how dust evolves under circumstances of disk clearing processes.

The potential existence of a massive planet interacting with a disk opens the possibility of overcoming one of the major problems of the core accretion

theory. As shown in the previous chapters, one of the most critical problems of this multi-stage process, that starts with the coagulation of submicron-sized particles and ends with terrestrial or cores of giant planets, is to understand how to stop the rapid inward migration of dust grains. If a massive planet opens a gap in the early stages of the disk, a huge-single pressure bump is expected in the radial direction due to the depletion in the gas surface density. This pressure bump becomes a "particle trap", a region where particles accumulate and grow (Pinilla et al. 2012b). In addition, the non-axisymmetric maps recently observed with ALMA (see e.g. Sect. A.1) can indeed be explained by a vortex formed when a planet is interacting with the disk (Chapter 6). These azimuthal pressure traps lead to strong asymmetries in the dust distribution of millimeter particles (Chapter 5).

Observational evidence of the presence of millimeter (mm) grains in the outer regions of disks has made theoreticians look for the missing piece of this rapid inward drift-puzzle. The slope of the spectral energy distribution $\alpha_{\rm mm}$ in the millimeter regime can be interpreted in terms of grains size (see e.g. Draine 2006) and low values of $\alpha_{\rm mm}$ ($\lesssim 3$) correspond to large grains. Large amount of sub- and millimeter observations of primordial protoplanetary disks have showed that the spectral index $\alpha_{\rm mm}$ reach values $\alpha_{\rm mm} \lesssim 3$ in Taurus, Ophiucus, and Chameleon star forming regions (e.g. Ricci et al. 2010a,b, 2011; Ubach et al. 2012). However the same statistical work for transition disks still needs to be done.

In this chapter, we present the first 3mm-observations of four transition disks: LkHα 330, UX Tau A, LRLL 31 and LRLL 67 using Plateau de Bure Interferometer (PdBI). The observations and data reduction are presented in Sect. 7.1. We collect the available photometric measures on these disks, to constrain different parameters of these disks doing the corresponding fitting of the SEDs. Additionally, combining previous observations done with the Submillimeter Array (SMA) at 345GHz of these sources by Brown et al. (2008); Brown et al. (2009); Andrews et al. (2011b); Espaillat et al. (2012), we calculate the mean spectral index $\alpha_{\rm mm}$. This work is still in progress, the preliminary results are in Sect. 7.3 and we discuss and conclude the fundings that we have so far in Sect. 7.4 and Sect. 7.5 respectively.

7.1 Observations and data reduction

7.1.1 PdBI data

The observations with PdBI were taken on 20th and 21st of September of 2012 under excellent weather conditions. The targets were observed in track-

Table 7.1: Source properties. Data from Andrews et al. (2011b) for LkHα 330 and UX Tau A and from Espaillat et al. (2012) for LRLL 31 and LRLL 67.

Name	$\alpha[J2000]$	$\delta[J2000]$	Region	$F_{345\mathrm{GHz}}(Jy)$	$\sigma(mJy)$
LkHα 330	03 45 48.29	+32 24 11.9	Perseus	0.21	2.1
UX Tau A	04 30 04.00	+18 13 49.3	Taurus	0.15	1.5
LRLL 31	03 44 18.00	+32 04 57.0	IC 348	0.062	6.0
LRLL 67	03 44 38.00	+32 03 29.0	IC 348	0.025	11

sharing mode, inter-scanned between the science target and quasars observations including 0333+321, 0234+285 and 0507+179 to calibrate the complex antenna gains.

For the amplitude and phase calibrations, additions observations of 3C84, MWC349 and 3C345 were done with constant intervals. For the data reduction, the Fourier inversion of the visibilities and the cleaning of the dirty image from the dust emission, the GILDAS software was used, obtaining good detections for four targets. The transition disk HD141569 was also observed, however the integration time of the observation ($\sim$ 20 mins) was not long enough for a good detection. Also, the position of this source in the south ($\delta_{J2000} = -03:\ 55:\ 16.3$), requires exceptional night conditions for a good detection with PdBI. This data set was discarded for this work.

Therefore, we present a sample of four transition disks: LkHα 330 a $\sim$ 3 Myr old, G3 pre-main sequence star in the Perseus molecular cloud. UX-Tau a $\sim$ 1 Myr old, G8 pre-main sequence star in Taurus star-forming region. LRLL 31 and LRLL 67 are G6 and M0.75 pre-main sequence stars respectively and both $\sim$ 3 Myr old in IC 348 region. The observations were carried at 3 millimeter continuum and with 6 antennas in the D-configuration. The D-antenna configuration is the most compact one with a resolution of 0.47" x 0.40" at 100GHz and for sources with a declination of $\sim$ 40°, and provides the lowest phase noise and highest sensitivity available using PdBI. These sources were selected based on the 880μm flux information available (Andrews et al. 2011b; Espaillat et al. 2012), the lack of 3 mm data in the literature and their position in the sky. The 880μm imaging of LkHα 330 and UX Tau A have confirmed a dust-depleted cavity for these disks. There

Table 7.2: Stellar Parameters. Data from Andrews et al. (2011b) for LkHα 330 and UX Tau A and from Espaillat et al. (2012) for LRLL 31 and LRLL 67.

Name	SpT	$T_{\rm eff}$ (K)	d (pc)	$L_\star$ ($L_\odot$)	$R_\star$ ($R_\odot$)	$M_\star$ ($M_\odot$)	$\dot{M}$ ($M_\odot$ yr^{-1})
LkHα 330	G3	5830	250	15	3.75	2.2	2.0×10^{-9}
UX Tau A	G8	5520	140	3.5	2.05	1.5	1.0×10^{-8}
LRLL 31	G6	5700	315	5.0	2.3	1.6	1.4×10^{-8}
LRLL 67	M.0.75	3720	315	0.5	1.8	0.5	1.0×10^{-10}

are not resolved images for LRLL 31 and LRLL 67. The available information about the fluxes of these disks and the corresponding stellar parameters are summarized in Tables 7.1 and 7.2 respectively, with the corresponding references.

LkHα 330: a G3 young star located in the Perseus molecular cloud at a distance of ∼250 pc. The first SMA observations were done by Brown et al. (2007); Brown et al. (2008) and then by Andrews et al. (2011a). From these observations, a gap of ∼68 AU radius at the continuum was reported. Assuming azimuthal symmetry, they derived an inclination between 42-84°. For this work, we assumed the fluxes measured by Andrews et al. (2011b), which combines SMA observations with the most extended configuration (V) supplemented by observations with the compact (C) and the extended (E) configurations, for a final resolution of 0.31" x 0.27".

UX Tau A: is a G8 primary star of a multiple system located in the region of Taurus at a distance of ∼ 140 pc. Andrews et al. (2011b) reported the first resolved observations of this disk with SMA, with a resolution of 0.31" x 0.28". From SED fitting, a gap of 25 AU of radius and a disk inclination of 52° were found. The emission from UX Tau B and UX Tau C do not contribute to the millimeter flux due they are fainter and due to the large separation between them (Furlan et al. 2006).

LRLL 31: a G6 young star locates in the IC 348 star forming region at a distance of $\sim$ 315pc. The only millimeter flux densities reported in the literature are by Espaillat et al. (2012) using the compact configuration (C) of SMA (with a maximum beam size of $\sim$ 2.12" x 1.90"). From the SED fitting, they classified this disk as a "pre-transition disk", with a optically thin inner disk of a radius of 0.32 AU, separated by an optically thin gap of a radius of 14 AU.

LRLL 67: a M0.75 young star, which is also located in the IC 348 region. It was observed with SMA by Espaillat et al. (2012) with the same antenna configuration than LRLL 31. From the SED modeling, this disk was classified by as a transition disk with a gap of 10 AU of radius.

7.1.2 Additional photometric observations

For the SED modeling, we collected the available fluxes at different wavelengths for these disks. For LkHα 330 the data comes from Brown et al. (2007); Brown et al. (2009); Andrews et al. (2011a), for UX Tau A the data is taken from Espaillat et al. (2007); Andrews et al. (2011a) and finally for LRLL 31 and LRLL 67 the data come from Muzerolle et al. (2009); Espaillat et al. (2012); Flaherty et al. (2012) and the citations therein.

7.2 Radiative transfer model of SEDs

We use the Monte Carlo-based 3-D radiative transfer code, MCFOST, to produce disk images and SEDs (Pinte et al. 2006) [1]. The temperature distribution is calculated following Bjorkman & Wood (2001), but with a continuous deposition of energy to estimate the mean intensity. We use a cylindrical grid, with an adaptive mesh at the inner edges of the disk. The radiation field and temperature structure estimated by the Monte Carlo runs are used to produce SEDs by calculating the formal solution of the radiative transfer equation along rays (ray-tracing method). We assume that the disk can be constituted of a mixture of carbon and silicate dust grains. Its structure is parametrized by power laws, therefore the surface density Σ, and the scale height H can be expressed as:

[1] The SED fitting by radiative transfer modeling was done by M. Benisty.

$$\Sigma(r) = \Sigma_{100\mathrm{AU}} \left(\frac{r}{100\mathrm{AU}}\right)^{q} \quad (7.1)$$

$$\mathrm{H(r)} = \mathrm{H}_{100\mathrm{AU}} \left(\frac{\mathrm{r}}{100\mathrm{AU}}\right)^{\beta}, \quad (7.2)$$

where β is the flaring exponent, $\Sigma_{100\mathrm{AU}}$ and $\mathrm{H}_{100\mathrm{AU}}$ are the values of the surface density and the height scale at a radius of 100 AU. The dust grain sizes (a) are distributed following a power law $a^{-3.5}$ (ISM), with a varying between the minimum and maximum sizes, a_{min} and a_{max} respectively. In addition, we fix the total dust mass ($\mathrm{M}_{\mathrm{dust}}$) of the disk, that is delimited by its inner and outer radii (R_{in} and R_{out}). For all targets, we consider $q = -1$, β has little effect on the inner disks that are very compact and is not well constrained.

For LkHα 330 and UX Tau A, we consider the radius of the cavity inferred from spatially resolved millimeter imaging with SMA (Andrews et al. 2011b). To keep such a large gap, but at the same time reproduce the significant mid and far infrared emission, we decouple the large and small grains into different layers to mimic dust sedimentation. The small grains layer is vertically more extended than for the large grains. We refer to the layer of large grains as the midplane. For UX Tau A, small grains also partially fill the cavity. This assumption is consistent with the mm observations, that probe large grains only, and with the recent findings on e.g. the transition disk SAO206462, where scattered light emission, that traces small grains in surface layers, is observed inside the mm cavity (Muto et al. 2012, and see also Appendix A.2). For LRLL31 and LRLL67 that have not been imaged so far, we consider the minimum number of zones/layers, i.e. two zones (inner and outer disks) for LRLL31 and only one for LRLL67. SED modeling being highly degenerate, images with mm interferometer are needed to spatially constrain the dust distribution, hence our models are not unique.

7.3 Results

7.3.1 3 mm maps and spectral index

Figure 7.1 shows the 3 mm continuum maps obtained with the PdBI observations for LkHα 330, UX Tau A, LRLL 31 and LRLL 67. The contour lines are every 3$\times\sigma$, 4$\times\sigma$, 2 $\times\sigma$ and 1$\times\sigma$ respectively.

At mm-wavelength the thermal emission of a protoplanetary disks comes from the optically thin dust, and therefore the total flux at a given wavelength is proportional to the mass of the dust M_d, i.e.

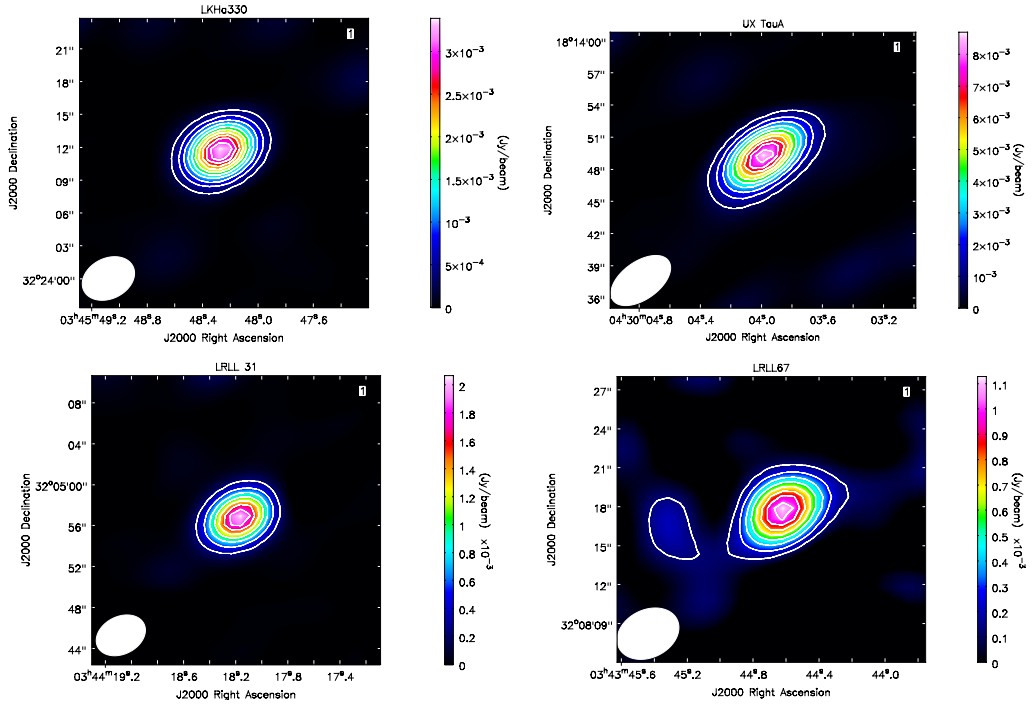

Figure 7.1: 3 mm continuum maps obtained with the PdBI observations for LkHα 330, UX Tau A, LRLL 31 and LRLL67. The contour lines are every 3×σ, 4×σ, 2 ×σ and 1×σ respectively, with σ summarized in Table 7.3 for each source.

Table 7.3: 3-millimeter fluxes and spectral indices

Source	$F_{3\mathrm{mm}}$ (mJy)	$\sigma_{3\mathrm{mm}}$ (mJy)	$\alpha_{0.88-3\mathrm{mm}}$
LkHα 330	3.9	0.10	3.25±0.032
UX Tau A	10.1	0.20	2.20±0.082
LRLL 31	2.88	0.13	2.46±0.223
LRLL 67	1.21	0.13	2.42±0.426

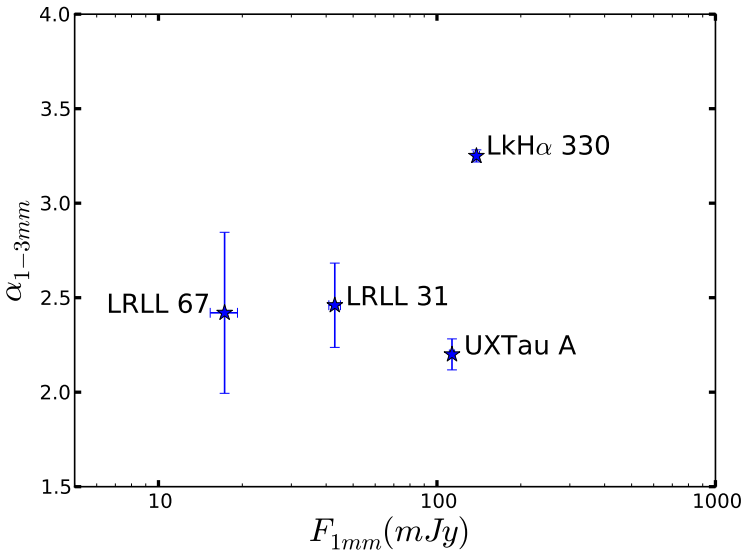

Figure 7.2: Spectral indices $\alpha_{1-3\mathrm{mm}}$ vs the flux at 1 mm for the observed transition disks, with the respectively uncertainties (Table 7.3)

$$F_\nu \approx \frac{\kappa_\nu M_d B_\nu(T)}{d^2}, \tag{7.3}$$

where κ_ν is the opacity of the dust particles at a given wavelength, d the distance to the source and $B_\nu(T)$ the blackbody radiation. In the Rayleigh-Jeans limit i.e. $h\nu \ll k_B T$ (being k_B the Boltzmann constant), $B_\nu(T)$ is proportional to the square of the frequency, i.e $B_\nu \propto \nu^2 T$. Therefore the flux depends on the power-law index of the opacity, usually call the opacity index β_{mm}, such that $\kappa_\nu \propto \nu^{\beta_{\mathrm{mm}}}$. The opacity index can be measured with multiwavelength observations ($\beta_{\mathrm{mm}} \equiv d\ln\kappa/d\ln\nu$) and the slope of the SED at long wavelengths can be approximated to $\alpha_{\mathrm{mm}} = \beta_{\mathrm{mm}} + 2$.

With the 3mm fluxes and the ones at 880 μm of these sources, we compute the flux at 1 mm and the spectral indices $\alpha_{1-3\mathrm{mm}}$ with the respectively uncertainties (see Table 7.3) and Fig. 7.2 summarizes our findings.

7.3.2 Disk parameters

The parameters of our models from the SED modeling are summarized in Tables. 7.4, 7.5, 7.6, 7.7, and fits of the SED for each target are shown in Fig. 7.3.

Table 7.4: Disk parameters for LkHα330

		inner disk	small grains layer	mid plane
M_{dust}	[$M_\odot$]	1.8e-10	1.6e-6	1.4e-4
R_{in}	[AU]	0.12	68	68
R_{out}	[AU]	5	125	125
H_{100AU}	[AU]	15	32	10
β		1.0	1.2	1.2
a_{min}	[μm]	0.05	0.05	100
a_{max}	[μm]	10	5	3000
carbon/silicate		0.6/0.4	0/1	0/1

Table 7.5: Disk parameters for UX Tau A

		inner disk	small grains layer	mid plane
M_{dust}	[$M_\odot$]	5e-12	2.2e-6	4e-4
R_{in}	[AU]	0.2	10	25
R_{out}	[AU]	1	300	300
H_{100AU}	[AU]	3	15	4.1
β		0.35	1.2	1.2
a_{min}	[μm]	0.05	0.05	500
a_{max}	[μm]	10	100	10000
carbon/silicate		0.6/0.4	0/1	0/1

7.4 Evidence for dust growth

Maps of submillimeter and microwave emission from the diffuse interstellar dust have showed that the typical values for the dust opacity index β_{mm} are $\sim 1.7 - 2.0$ (see e.g. Finkbeiner et al. 1999). Hence, if the dust in protoplanetary disks is similar to the interstellar medium (ISM) dust, it was expected α_{1-3mm} to be $\sim 3.7 - 4$. However, Beckwith & Sargent (1991) claimed for the first time that the spectral index α_{1-3mm} is lower for the protoplanetary disks.

The question of what exactly makes the opacity index to be lower for protoplanetary disks than for the ISM, has been addressed by different authors. One possible explanation is that the emission or part of the emission may come from regions where the dust is optically thick at millimeter wave-

Table 7.6: Disk parameters for LRLL31

		inner disk	outer disk
M_{dust}	[$M_\odot$]	3.5e-12	1.0e-3
R_{in}	[AU]	0.32	14
R_{out}	[AU]	1	300
H_{100AU}	[AU]	32	2
β		0.8	0.8
a_{min}	[μm]	0.05	0.05
a_{max}	[μm]	2	1000
carbon/silicate		0/1	0/1

Table 7.7: Disk parameters for LRLL67

		outer disk
M_{dust}	[$M_\odot$]	1.0e-3
R_{in}	[AU]	10
R_{out}	[AU]	300
H_{100AU}	[AU]	2
β		0.8
a_{min}	[μm]	0.05
a_{max}	[μm]	1000
carbon/silicate		0/1

lengths (Testi et al. 2003). Also the chemical composition (Semenov et al. 2003), porosity (Birnstiel et al. 2010b) and the geometry of the dust particles can affect the opacity index, although their impact is not significant (see e.g. Natta et al. 2004). Another possibility is that dust grains have grown to mm-sizes (see in addition to the authors mentioned in the introduction Calvet et al. 2002; Natta & Testi 2004).

Our results show that for three of the observed transition disks, UX-Tau, LRLL 31 and LRLL 67, the spectral index α_{mm} is lower than 3 implying that dust may have grown to mm-sizes in these disks (Fig. 7.2). However, this analysis is done assuming that the dust opacity (or β_{mm}) is constant throughout the disk and it does not depend on radius. Analysis of recent mm-observations at different wavelengths of several protoplanetary disks have

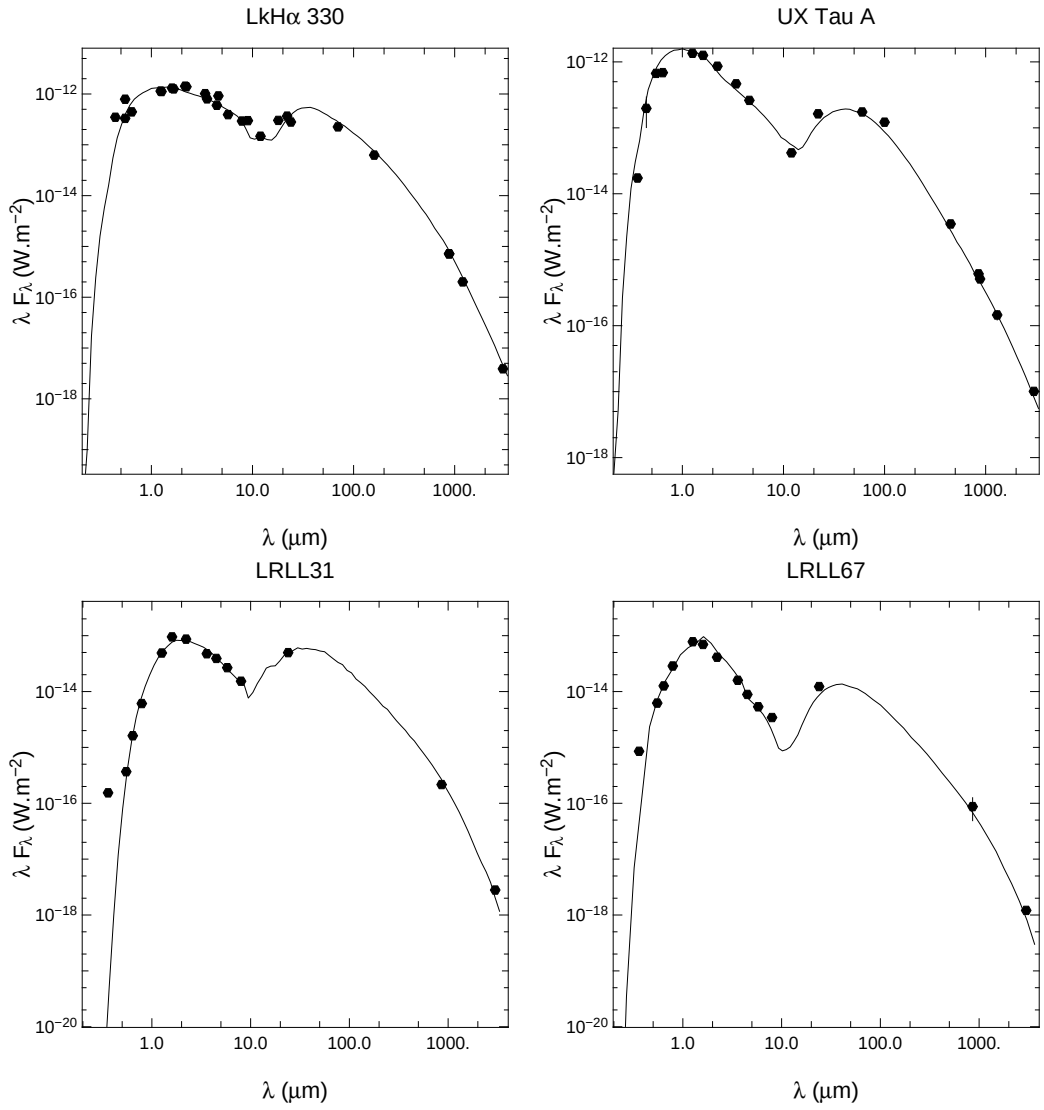

Figure 7.3: Model fits to the SEDs of LkHα 330 (*top-left panel*), UX Tau A (*top-right panel*), LRLL 31 (*bottom-left panel*) and LRLL 67 (*bottom-right panel*), including the 3 mm data reported in this chapter. The disk parameters for the best model of each target are summarized in Tables 7.4, 7.5, 7.6 and 7.7.

showed that the opacity index may change with radius (Isella et al. 2010a; Guilloteau et al. 2011; Pérez et al. 2012). For instance, Guilloteau et al. (2011) investigated a total of 23 disks in Taurus-Auriga region and foun that $\beta_{\rm mm}$ increases with radius, implying that for most of the targets, dust grains are larger in the inner disk ($\lesssim$ 100 AU) than beyond.

For our observations, LkHα 330 is the only target for which the spectral index is higher than 3, which can be wrongly interpreted as no-grain growth, if one assumes constant values of $\beta_{\rm mm}$ for the whole disk. From the SED modeling (Sect. 7.3) and previous work (e.g. Andrews et al. 2011a), LkHα 330 is the disk with the largest inner hole ($\sim$ 68 AU) of our observed targets and the clearing mechanism acting in this disk can lead to strong radial variations in the dust size distribution (see e.g. Chapter 4). The large value of $\alpha_{\rm mm}$ is also confirmed by Isella et. al. (priv. communication), who report CARMA observations at 1.3 mm of this transition disk, obtaining a spectral index of $\alpha_{0.88-1.3{\rm mm}} = 3.6 \pm 0.5$.

For the other three transition disks, the SED modeling shows that the inner holes are less radially extended (from 10 to 25 AU, Sect. 7.3), therefore the interpretation of a constant opacity all over the disk may approximately be correct. Observations at different (sub)-millimeter wavelengths with higher angular resolution are needed to make predictions of possible opacity variations in the disk.

For transition disks, different efforts have tried to explain the diversity of these objects such as: the extension of the observed inner holes from 4 AU to even more than 100 AU, relatively high accretion rates ($\sim 10^{-8}$ $M_\odot$ yr^{-1}), averaged lifetimes ($\sim$ 1-3 Myr) (see Williams & Cieza 2011, for a review). Recently, different works combined various physical models to explain such properties. For instance, Rosotti et al. (2013) combined X-ray photoevaporation models with planet disk interaction to explain the transition disks that have accretion rates comparable with classical T-Tauri stars and large inner holes. On the other hand, Pinilla et al. (2012b) studied how the dust evolves in a disk which is perturbed by the presence of a massive planet. In that work, they demonstrate that the ring-shaped emission of some transition disks can be modeled with a single planet and the radial position where the mm-sized particles are located depends on the shape of the resulting gap, which is basically determinated by the disk viscosity and the mass of the planet.

Alternative models such as a vortex generated by a dead zone (region in the disk where the viscosity drops down) may explain the asymmetries of transition disks (Regály et al. 2012), in particular the ones reported by Brown et al. (2009), including LkHα 330. Any model that considers a gas variation that leaves to a pressure bump, would be a good scenario to have a particle trapping. Dust particles drift towards the regions where the pressure has a maximum and where the gas moves with Keplerian speed, canceling the constant aerodynamical drag that grains feel due to the typical sub-Keplerian gas velocity. Under these assumptions, the opacity index is expected to vary with radius due to the strong radial variations of the grain size distribution.

The variation of the opacity index may be a general property of protoplanetary disks and still needs to be studied in more detail in transition disks.

7.5 Conclusion

We have reported the first 3 millimeter observations carried with PdBI of four transition disks: LkHα 330, UX-Tau, LRLL 31, LRLL 67. Adding this data for the SED modeling, we have derived different disk parameters summarized in Tables 7.4, 7.5, 7.6 and 7.7 for each disk respectively. Our findings are in agreement with previous SED fitting by e.g. Brown et al. (2009); Andrews et al. (2011a); Espaillat et al. (2012).

With previous observations of these targets at 880 μm, we calculate the spectral index, finding that for three of the sources the values for $\alpha_{\rm mm}$ are lower than typical values of the ISM-dust, which may imply that dust has grown to mm-sizes. For the transition disk LkHα 330, $\alpha_{\rm mm} > 3$, which is the one with the largest inner hole from the SED modeling ($\sim$ 68 AU, Sect. 7.3), but this assumes that the opacity is constant for the whole disk. Recent observations at different wavelengths have showed that opacity may radially change throughout the disk (Isella et al. 2010a; Guilloteau et al. 2011; Pérez et al. 2012). In addition, studies that combine dust evolution and planet formation for transition disks (Pinilla et al. 2012b) indicated that the dust size distribution may present strong variations in the radial direction, leading to the possibility of radial variations of the dust opacity as well. For UX-Tau, LRLL 31 and LRLL 67 the spectral index indicates grain-growth, and the assumption of constant opacity index may be a good approximation in these cases, since the SED fitting implies inner holes that are less radially extended ($\sim$ 10-25 AU, Sect. 7.3).

Observations with new telescope arrays such as EVLA, ALMA and NOEMA will provide the enough sensitivity and angular resolution to constrain in more detail the dust opacity distribution in transition disks. In addition, a statistical work that relates the spectral index of transition disks with the stellar parameters such as stellar type and accretion rate, still needs to be done and is one of the aims of this project.

Chapter 8

Summary and conclusions

Different disk structures have been revealed by observations done by e.g. Spitzer, Herschel, SMA and ALMA, which shows that the distribution of gas and dust varies in circumstellar disks. This may be related with the diversity of exoplanets found thus far by e.g. Kepler mission and the Hubble Space Telescope. This thesis explores the first steps of planet formation when micron-sized particles grow to planetesimals, linking numerical models with current millimeter-observations in cases where the physical conditions differ, directly affecting the final dust distribution in disks.

The first aim of this thesis is to explain the presence of millimeter-sized dust in the outer regions of T-Tauri disks. It is demonstrated that with pressure bumps in the gas disk, such as the zonal flows resulting from simulations of magneto-rotational turbulence or the larger scale bumps that may occur at deadzones or sublimation edges, pebbles are formed and retained in the outer regions of the disks, in contrast with the case of a smooth disk with a gas pressure profile monotonically decreasing with radius. This allows to have a good agreement between theoretical models and millimeter-observations of young disks in Orion nebula, Taurus and Ophiucus star forming regions (Chapter 2). A deeper comprehension of the origin of these disk inhomogeneities would be an important improvement to the existing theory. If magnetorotational instability causes pressure bumps in disks, simulations have shown that these pressure variations only live up to $\simeq$ 1000 years, and their amplitude and phase can change with time. Simultaneous and time-dependent modeling of gas and dust evolution are important to prove the effectiveness of dust trapping under this scenario of global pressure bumps. In addition, a more accurate study of the dust dynamics that includes for example the bouncing between particles and its effects for the current fundings needs to be investigated.

Recent ALMA and CARMA observations of disks around Brown Dwarfs have shown the existence of millimeter-sized grains in the cold regions of those low-mass disks. The physical processes of the first steps of planet formation around low mass objects differ from the ones around Sun-like stars. In particular settling to the midplane and radial drift occur more efficiently in Brown Dwarfs disks, leading to have a flatter geometry and a dust-depleted disk on shorter timescales. The explanation of current observational discoveries, revealing pebbles in these disks, needs to consider extreme conditions like strong pressure inhomogeneities (Chapter 3). Global simulations examining magnetorotational instabilities are needed to probe if those pressure bumps may exist under Brown Dwarfs disk conditions. In addition, dust evolution simulations that include the vertical structure are important to reproduce some observational features of Brown Dwarfs disks, as for example the flatter geometry of these disks compared to T-Tauri disks. Additional high-resolution observations of disks are needed to increase the statistical survey about the physical information of the nature of dust grains in disk of different mass and with a large range of stellar parameters, which may help to constrain better the theoretical models presented in this thesis.

One exciting scenario to test the dust trapping hypothesis is to explain the observed properties of transition disks. In this thesis, it was studied how the dust evolves in the case where a single massive planet interacts with a disk, which could be the clearing mechanism for the observed inner gaps of transition disks. The combination of two-dimensional hydrodynamical disk simulations with dust evolution modeling shows that millimeter-sized grains form and accumulate at the pressure maximum created at the outer edge of the gap and naturally produce the observed ring shaped at sub-millimeter emission. In addition, a large radial separation between the gas emission in the outer disk and the peak of the millimeter emission is expected, when the planet is massive enough to make the disk eccentric (Chapter 4). Although, eccentricities lead to azimuthal asymmetries in the gas, these are not pressure traps and therefore no strong dust azimuthal variations are expected in this case. Nevertheless, the gas accumulation in the outer edge of a gap formed by a massive planet, can become Rossby unstable and produce large anti-cyclonic vortices, which can be long-lived when the disk has moderate viscosity (Chapter 5). These vortices become the birthplaces of pebbles and lead to strong azimuthal variations in the sub-(millimeter) emission, such as the ones already detected and resolved with current ALMA observations, as it is the case of the transition disk IRS 48 (See Fig A.1).

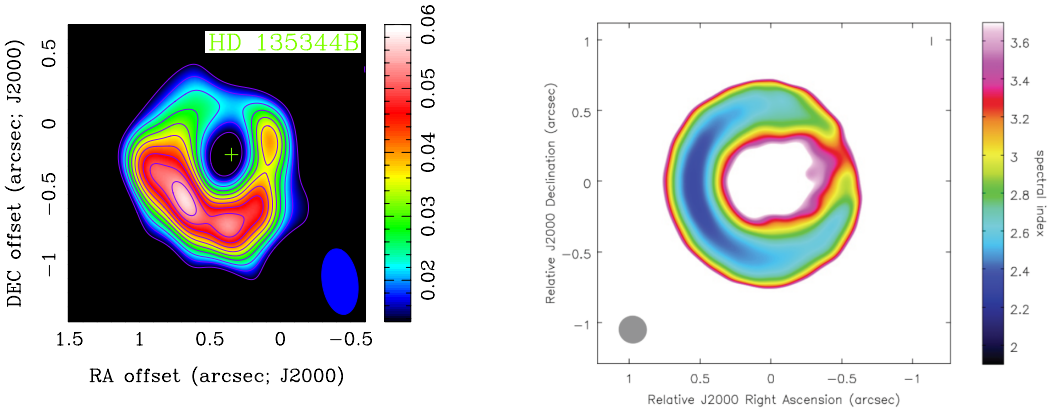

Figure 8.1: *Left*: The 340 GHz SMA map of HD135344B by Brown et al. (2009). *Right*: Simulated spectral index map considering coagulation/ fragmentation modeling and a vortex created by the presence of a dead zone (Regály et al. 2012), for the specific case of the TD HD135344B. For the spectral index is considered band 7 (340GHz) and band 9 (675GHz), the most extended configuration of ALMA-Cycle 1 for band 7, and a configuration for band 9 that provides the same angular resolution than band 7 (0.16").

Millimeter observations at different wavelengths of transition disks (as the ones presented in Chapter 7) will help to constrain the models presented in this thesis in Chapters 4, 5 and 6 and increase the statistics of the measured spectral index for transition disks. Observations at longer wavelengths are needed to resolve the structures of transition disks that may leave to radial variations of the opacity throughout the disk. For instance, the left panel of Fig. 8.1 shows the SMA map of HD135344B by Brown et al. (2009) with a clear azymuthal asymmetry, but observations with higher angular resolution of this disk with e.g. ALMA at different frequencies will help to constrain the models for this transition disk. Indeed, the right panel of Fig. 8.1 shows the corresponding simulated spectral index map considering coagulation/ fragmentation modeling and a vortex created by the presence of a dead zone (Regály et al. 2012), for this specific transition disk. It is still a matter of debate what is the clearing mechanism, is a massive planet or a multiple planet system? vortices due to dead zones? photoevaporation? or the mix of different phenomena? If the observed azimuthal variations are the result of a single massive planet interacting with the disk, our models presented in Chapter 6 show that the viscosity of the disk can be constrained, which

is important to estimate the disk lifetime. Simulations of the gas dynamics and dust growth combined with high angular resolution and sensitivity observations are needed to understand better the nature of transition disks and their properties.

This thesis presents models of gas dynamics and dust growth in different scenarios of circumstellar disks, such as T-Tauri, Brown Dwarfs an transition disks and their compatibility with millimeter-observations. We show that, under different physical conditions, one of the most critical paradigms of planet formation such as the meter-size barrier can be overcome, leading to optimal conditions for the existence of planetesimal incubators in protoplanetary disks. But new observations with e.g. ALMA or NOEMA combined with more detailed numerical models are already opening even more exciting questions in the planetary formation field such as: what is the origin of turbulence in disks and how this influences the gas and dust evolution? What are the observational signatures if planets are or not embedded in disks? What is the effect of stellar activities on the gas and dust within the disk?, etc. This leaves the doubt of how planets form far to be completely answered.

Appendix A

Additional contributions to the field

A.1 A major dust trap in a transition disk triggered by a companion

To be published in Science

Authors:
Nienke van der Marel, Ewine F. van Dishoeck, Simon Bruderer, Til Birnstiel, **Paola Pinilla**, Cornelis P. Dullemond, Tim A. van Kempen, Markus Schmalzl, Joanna M. Brown, Gregory J. Herczeg, Geoffrey S. Mathews, Vincent Geers.

Summary:
In this work is shown, for the first time, a clear observational evidence of a pressure trap in the circumstellar disk around Oph IRS48 using ALMA observations. The continuum map at 0.44 millimeter reveals a strong azimuthal asymmetry located at $\sim$ 60 AU from the central star and with a radial extension up to $\sim$80 AU. The high contrast of this asymmetry reaches values of 100, which peak emission has a signal-to-noise ratio of $\sim$ 390. In addition, these ALMA observations show that the gas disk is resolved in ^{12}CO 6-5 emission, revealing a notable gas density reduction within $\sim$ 20 AU. In combination with near infrared CRIRES data of the hot CO ν=1-0 line (Brown et al. 2012), it was concluded that this disk has a gas hole of $\sim$ 25 AU. Also, the continuum imaging at 18.7 μm shows that the micron-sized particles extend over a well-rounded ring. These fundings have two important consequences:

1. The existing gap in the transition disk around Oph IRS48 has different

radial extensions for the gas ($\sim$ 25 AU), of the optically thick ^{12}CO line, than for the millimeter grains ($\sim$ 45-80 AU), as it is predicted by the model explained in Chapter 4. This observation is in agreement with the results of this model that assumes that a planet carves a gap in a disk and in the case that the planet is massive enough, it is expected that the peak of the millimeter emission is located at distances that can be more than twice the star-planet separation. This suggests that the ring-shaped maps observed for some transition disk are indeed pressure traps induced by a massive planet.

2. This observation also shows a clear evidence of an additional pressure trap in the azimuthal direction, in which millimeter particles are trapped in one side of the ring while micron sized particles are well coupled to the gas and they move along with it. In Chapter 5 is demonstrated that a smooth but long-lived azimuthal gas density gradient can lead to strong accumulations of dust, which may explain the high azimuthal contrast of these observations. Additionally, in Chapter 6 is shown that the possible origin of these azimuthal pressure traps is due to the existence of a long-lived vortex which may produce by a massive planet interacting with a disk which viscosity is moderate. In the case of IRS 48 transition disk, we claim that the strong azimuthal asymmetry is due to a vortex which originates by the interaction of a massive planet with the disk.

Figure A.1 summarizes my main contribution to this work. To explain the radial position of the millimeter grains, we consider a $\sim$ 10 $M_{\rm Jup}$ planet interacting with a disk (with properties similar than the ones observed for IRS 48). The resulting gap produces that the pressure maxima is located at $\sim$ 42 AU, where millimeter particles are expected to be trapped, while the outer edge of the gap in the gas starts to increase at $\sim$ 25 AU. In addition, this massive planet within a disk with a viscosity of $\alpha = 10^{-4}$ produces a vortex, with a contrast of 2-3 in the gas surface density, that survives for long time scales ($\sim$ 0.1 Myr). This contrast is used to study the dust distribution in the azimuthal direction following the model introduced in Chapter 5, which leads to a similar contrast that the one detected with ALMA observations ($\sim$ 100).

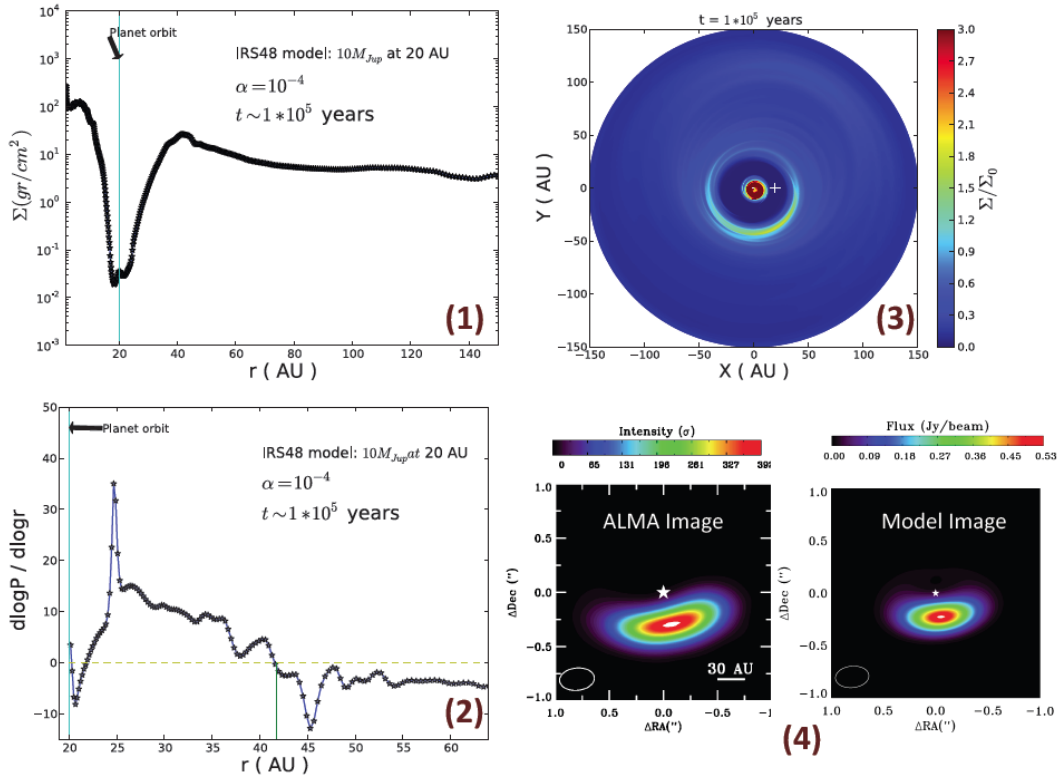

Figure A.1: Results of the hydrodynamical simulations of a gap created by a planet located in a fixed orbit at 20 AU within a disk with similar properties as the observed ones for IRS48 transition disk after $\sim$ 1120 orbits: (1) Azimuthally averaged surface density (2) Radial pressure gradient. (3) Evidence of a vortex in two-dimensional gas surface density with a contrast of $\sim$ $2-3$ after 0.1 Myr of evolution. (4) The ALMA continuum image at $\lambda = 0.44$ mm and the corresponding synthetic image using the models summarized in Chapters 5 and 6. The figures of the ALMA image and the corresponding model are taken from van der Marel et. al., to be published in Science.

A.2 Imaging diagnostics for transition discs

To be submitted to A&A

Authors:
Maria de Juan Ovelar, Michiel Min, Carsten Dominik, Christian Thalmann, **Paola Pinilla**, Myriam Benisty, Til Birnstiel.

Summary:
Based on the results of Chapter 4, we are doing radiative transfer modeling to compute the thermal and scattered emission and produce synthetic images of transition disks at different wavelengths. For each case considered in Chapter 4, i.e. $M_{\rm planet} = \{1, 9, 15\}$ $M_{\rm Jup}$, the emission at different bands is shown, as for instance: *R-band* (0.65 μm, intensity and polarization light), *H-band* (1.6 μm, intensity and polarization light), *Q-band* (20 μm) and continuum at 850 μm. In addition, realistic images are simulated for different instruments such as: SPHERE-ZIMPOL in the visible, HiCIAO in H-band, VLT-Qband and ALMA Cycle 1 at 850 μm, Fig. A.2 shows the resulting model images for each case.

The results of this work shows that trapping and filtering processes of dust particles of different sizes, that occurs when a massive planet is interacting with the disk, can lead to different observational signatures at different wavelengths. In particular for the case of $M_{\rm planet} = 1$ $M_{\rm Jup}$, small particles ($a \lesssim 1$ mm) can move trough the gap and produce a significant emission in the inner part of the disk. Contrary to the cases of more massive planets, where most of the dust grains are filtered and millimeter particles are trapped in the outer edge of the gap. The emission in the inner and in the outer edge of the gap, at different wavelengths, strongly depends on the mass of the planet (see Fig. A.2). Therefore combinations of (sub)-mm and polarimetric observations can in principle constrain the mass and the position of the planet, if this is the responsible mechanisms of the observed inner gaps in transition disks. For instance, observations in the *R-band* reveal totally different features (Fig. A.2) for each of the cases considered ($M_{\rm planet} = \{1, 9, 15\}$ $M_{\rm Jup}$).

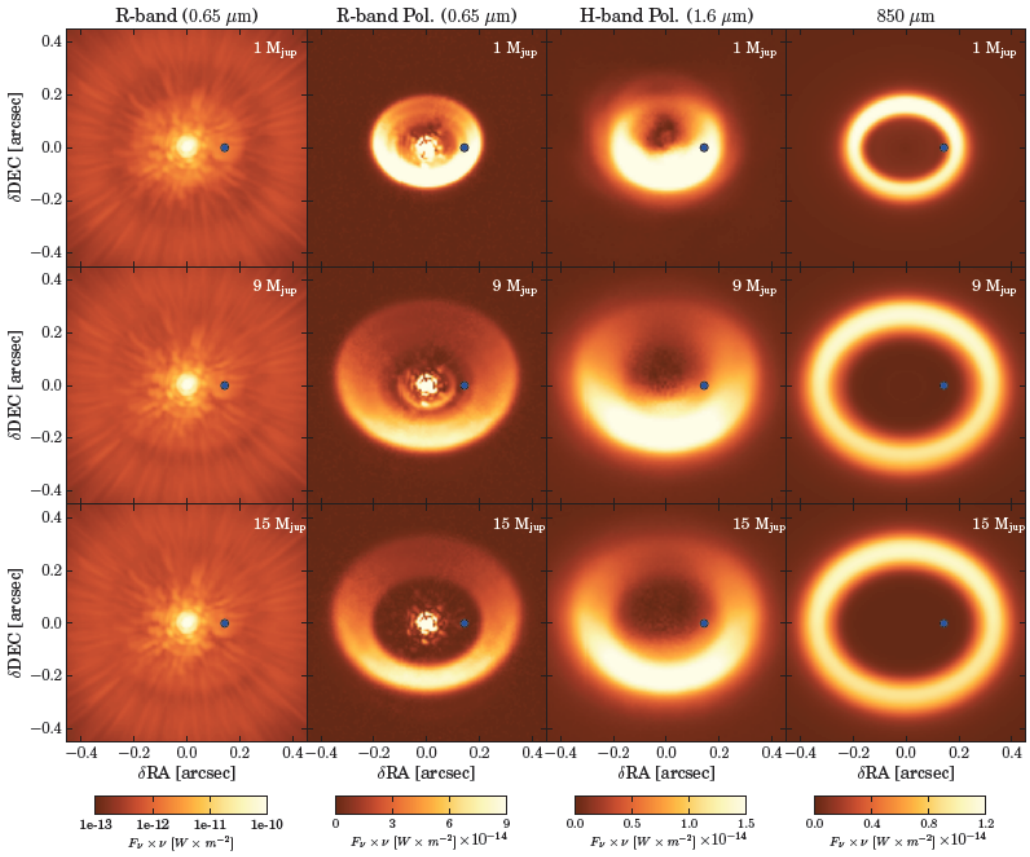

Figure A.2: Simulated images at different wavelengths considering the dust density distributions when a planet of different mass $M_{\rm planet} = \{1, 9, 15\}\ M_{\rm Jup}$ carves a gap in the disk (Chapter 4). The image is taken from de Juan Ovelar et. al (in prep).

Bibliography

Allers, K. N., Kessler-Silacci, J. E., Cieza, L. A., & Jaffe, D. T. 2006, ApJ, 644, 364

André, P., & Montmerle, T. 1994, ApJ, 420, 837

André, P., 2002, The Initial Conditions for Protostellar Collapse: Observational Constraints. EAS Publications Series, 3, pp 1-38.

Andrews, S. M., & Williams, J. P. 2005, ApJ, 631, 1134

Andrews, S. M., Wilner, D. J., Hughes, A. M., Qi, C., & Dullemond, C. P. 2010, ApJ, 723, 1241

Andrews, S. M., Rosenfeld, K. A., Wilner, D. J., & Bremer, M. 2011a, ApJ, 742, L5

Andrews, S. M., Wilner, D. J., Espaillat, C., et al. 2011b, ApJ, 732, 42

Apai, D., Pascucci, I., Bouwman, J., et al. 2005, Science, 310, 834

Armitage, P. J. 2011, ARA&A, 49, 195

Ataiee, S., Pinilla, P., Zsom, A., et al. 2013, Accepted for publication in A&A arXiv:1304.1736

Balbus, S. A., & Hawley, J. F. 1991, ApJ, 376, 214

Barge, P. & Sommeria, J. 1995, A&A, 295, L1

Batalha, N. M., Rowe, J. F., Bryson, S. T., et al. 2013, ApJS, 204, 24

Beckwith, S. V. W., Sargent, A. I., Chini, R. S., & Guesten, R. 1990, AJ, 99, 924

Beckwith, S. V. W., & Sargent, A. I. 1991, ApJ, 381, 250

Benisty, M., Tatulli, E., Ménard, F., & Swain, M. R. 2010,A&A, 511, A75

Bertout, C., Robichon, N., & Arenou, F. 1999, A&A, 352, 574

Biller, B., Lacour, S., Juhász, A., et al. 2012, ApJL, 753, L38

Birnstiel, T., Dullemond, C. P., & Brauer, F. 2010a, A&A, 513, A79

Birnstiel, T., et al. 2010b, A&A, 516, L14

Birnstiel, T., Klahr, H., & Ercolano, B. 2012a, A&A, 539, 148

Birnstiel, T., Andrews, S. M., & Ercolano, B. 2012,A&A, 544, A79

Birnstiel, T., Dullemond, C. P., & Pinilla, P. 2013, A&A 550, L8

Bjorkman, J. E., & Wood, K. 2001, ApJ, 554, 615

Blum, J., & Wurm, G. 2008, ARA&A, 46, 21

Boley, A. C. 2009, ApJL, 695, L53

Bouy, H., Huélamo, N., Pinte, C., et al. 2008, A&A, 486, 877

Brandenburg, A., Nordlund, A., Stein, R. F., & Torkelsson, U. 1995, ApJ, 446, 741

Brauer, F., Dullemond, C. P., Johansen, A., Henning, T., Klahr, H., & Natta, A. 2007, A&A, 469, 1169

Brauer, F., Dullemond, C. P., & Henning, T. 2008, A&A, 480, 859

Brown, J. M., Blake, G. A., Dullemond, C. P., et al. 2007, ApJL, 664, L107

Brown, J. M., Blake, G. A., Qi, C., Dullemond, C. P., & Wilner, D. J. 2008, ApJ, 675, L109

Brown, J. M., Blake, G. A., Qi, C., et al. 2009, ApJ, 704, 496

Brown, J. M., Rosenfeld, K. A., Andrews, S. M., Wilner, D. J., & van Dishoeck, E. F. 2012, ApJL, 758, L30

Burrows, C. J., Stapelfeldt, K. R., Watson, A. M., et al. 1996, ApJ, 473, 437

Calvet, N., D'Alessio, P., Hartmann, L., et al. 2002, Apj, 568, 1008

Calvet, N., D'Alessio, P., Watson, D. M., et al. 2005, ApJ, 630, L185

Cameron, A. G. W. 1978, Moon and Planets, 18, 5

Carpenter, J. M., Mamajek, E. E., Hillenbrand, L. A., & Meyer, M. R. 2006, ApJL, 651, L49

Casassus, S., van der Plas, G., M, S. P., et al. 2013, Nature, 7

Chandrasekhar, S. 1961, International Series of Monographs on Physics, Oxford: Clarendon, 1961,

Chiang, E. I., & Goldreich, P. 1997, ApJ, 490, 368

Cossins, P., Lodato, G., & Testi, L. 2010, MNRAS, 407, 181

Crida, A., Morbidelli, A., & Masset, F. 2006, Icarus, 181, 587

Crida, A. & Morbidelli, A. 2007, MNRAS, 377, 1324

Cuzzi, J. N. & Hogan, R. C. 2003, Icarus, 164, 127

Cuzzi, J. N., Hogan, R. C., & Shariff, K. 2008, ApJ, 687, 1432

D'Alessio, P., Canto, J., Calvet, N., & Lizano, S. 1998, ApJ, 500, 411

D'Alessio, P., Calvet, N., & Hartmann, L. 2001, ApJ, 553, 321

De Val-Borro, M., Edgar, R. G., Artymowicz, P., et al. 2006, MNRAS, 370, 529

De Val-Borro, M., Artymowicz, P., D'Angelo, G., & Peplinski, A. 2007, A&A, 471, 1043

Dodson-Robinson, S. E. & Salyk, C. 2011, Apj, 738, 131

Dorschner, J., Begemann, B., Henning, T., Jaeger, C., & Mutschke, H. 1995, A&A, 300, 503

Draine, B. T. 2006, ApJ, 636, 1114

Dullemond, C. P., Dominik, C., & Natta, A. 2001, ApJ, 560, 957

Dullemond, C. P., & Dominik, C. 2004, A&A, 421, 1075

Dullemond, C. P., & Dominik, C. 2005, A&A, 434, 971

Dullemond, C. P., Hollenbach, D., Kamp, I., & D'Alessio, P. 2007, Protostars and Planets V, 555

Dzyurkevich, N., Flock, M., Turner, N. J., Klahr, H., & Henning, T. 2010, A&A, 515, A70

Espaillat, C., Calvet, N., D'Alessio, P., et al. 2007, ApJ, 670, L135

Espaillat, C., Ingleby, L., Hernández, J., et al. 2012, ApJ, 747, 103

Espaillat, C., D'Alessio, P., Hernández, J., et al. 2010, ApJ, 717, 441

Fedele, D., van den Ancker, M. E., Henning, T., Jayawardhana, R., & Oliveira, J. M. 2010, A&A, 510, A72

Finkbeiner, D. P., Davis, M., & Schlegel, D. J. 1999, ApJ, 524, 867

Flaherty, K. M., Muzerolle, J., Rieke, G., et al. 2012, ApJ, 748, 71

Flock, M., Dzyurkevich, N., Klahr, H., Turner, N. J., & Henning, T. 2011, ApJ, 735, 122

Fromang, S. & Nelson, R. P. 2005, MNRAS, 364, L81

Fukagawa, M., Hayashi, M.,

Furlan, E., Hartmann, L., Calvet, N., et al. 2006, ApJS, 165, 568

Gammie, C. F. 1996, ApJ, 457, 355

Goldreich, P. & Ward, W. R. 1973, ApJ, 183, 1051

Gorti, U., Dullemond, C. P., & Hollenbach, D. 2009, ApJ, 705, 1237

Guieu, S., Pinte, C., Monin, J.-L., et al. 2007,A&A, 465, 855

Guilloteau, S., Dutrey, A., Piétu, V., & Boehler, Y. 2011, A&A, 529, A105

Gundlach, B., Kilias, S., Beitz, E., & Blum, J. 2011, Icarus, 214, 717

Güttler, C., Blum, J., Zsom, A., Ormel, C. W., & Dullemond, C. P. 2010, A&A, 513, A56

Haisch, K. E., Jr., Lada, E. A., & Lada, C. J. 2001, ApJL, 553, L153

Harvey, P. M., Henning, T., Liu, Y., et al. 2012b, ApJ, 755, 67

Harvey, P. M., Henning, T., Ménard, F., et al. 2012a, ApJ, 744, L1

Hawley, J. F., Gammie, C. F., & Balbus, S. A. 1995, ApJ, 440, 742

Hayashi, C. 1981, Progress of Theoretical Physics Supplement, 70, 35

Herbig, G. H. 1950, ApJ, 111, 11

Herczeg, G. J., Cruz, K. L., & Hillenbrand, L. A. 2009, ApJ, 696, 1589

Hernández, J., Hartmann, L., Megeath, T., et al. 2007, ApJ, 662, 1067

Hsieh, H.-F., & Gu, P.-G. 2012, ApJ, 760, 119

Huélamo, N., Lacour, S., Tuthill, P., et al. 2011, A&A, 528, L7

Hughes, A. M., Andrews, S. M., Espaillat, C., et al. 2009, ApJ, 698, 131

Hughes, A. M., Wilner, D. J., Andrews, S. M., Qi, C., & Hogerheijde, M. R. 2011, ApJ, 727, 85

Isella, A., Carpenter, J. M., & Sargent, A. I. 2009, ApJ, 701, 260

Isella, A., Carpenter, J. M., & Sargent, A. I. 2010a, ApJ, 714, 1746

Isella, A., Natta, A., Wilner, D., Carpenter, J. M., & Testi, L. 2010b, ApJ, 725, 1735

Isella, A., Pérez, L. M., & Carpenter, J. M. 2012, ApJ, 747, 136

Jaeger, C., Mutschke, H., Begemann, B., Dorschner, J., & Henning, T. 1994, A&A, 292, 641

Joergens, V., Pohl, A., Sicilia-Aguilar, A., & Henning, T. 2012, A&A, 543, A151

Johansen, A., & Klahr, H. 2005, ApJ, 634, 1353

Johansen, A., Oishi, J. S., Mac Low, M.-M., Klahr, H., Henning, T., & Youdin, A. 2007, Nature, 448, 1022

Johansen, A., Youdin, A., & Klahr, H. 2009, ApJ, 697, 1269

Johansen, A., Klahr, H., & Henning, T. 2011, A&A, 529, A62

Kenyon, S. J., & Hartmann, L. 1987, ApJ, 323, 714

Klahr, H. H., & Henning, T. 1997, Icarus, 128, 213

Klein, R., Apai, D., Pascucci, I., Henning, T., & Waters, L. B. F. M. 2003, ApJ, 593, L57

Kley, W. & Dirksen, G. 2006,A&A, 447, 369

Koller, J., Li, H., & Lin, D. 2003, ApJ, 596, L91

Kraus, A. L., & Ireland, M. J. 2012, ApJ, 745, 5

Krijt, S. & Dominik, C. 2011,A&A, 531, A80

Kuiper, G. P. 1951, Proceedings of the National Academy of Science, 37, 1

Lada, C. J. 1987, Star Forming Regions, 115, 1

Laughlin, G., Steinacker, A., & Adams, F. C. 2004, ApJ, 608, 489

Li, H., Finn, J., & Lovelace, R. 2000, ApJ, 533, 1023

Li, H., Colgate, S. A., Wendroff, B., & Liska, R. 2001, ApJ, 551, 874

Li, H., Li, S., Koller, J., et al. 2005, ApJ, 624, 1003

Lin, D. N. C. & Papaloizou, J. 1979, MNRAS, 186, 799

Lin, M.-K. & Papaloizou, J. C. B. 2011, MNRAS, 415, 1445

Lin, M.-K. 2012, MNRAS, 426, 3211

Liu, M. C., Najita, J., & Tokunaga, A. T. 2003, ApJ, 585, 372

Lommen, D., Maddison, S. T., Wright, C. M., van Dishoeck, E. F., Wilner, D. J., & Bourke, T. L. 2009, A&A, 495, 869

Lovelace, R. V. E., Li, H., Colgate, S. A., & Nelson, A. F. 1999, ApJ, 513, 805

Lubow, S. H. & D'Angelo, G. 2006, ApJ, 641, 526

Luhman, K. L., Adame, L., D'Alessio, P., et al. 2007, ApJ, 666, 1219

Lynden-Bell, D., & Pringle, J. E. 1974, MNRAS, 168, 603

Lyra, W., Johansen, A., Klahr, H., & Piskunov, N. 2008, A&A, 479, 883

Lyra, W., Johansen, A., Klahr, H., & Piskunov, N. 2009, A&A, 493, 1125

Lyra, W. & Mac Low, M.-M. 2012, ApJ, 756, 62

Markiewicz, W. J., Mizuno, H., & Voelk, H. J. 1991, A&A, 242, 286

Masset, F. 2000,A&AS, 141, 165

Matsuo, T., Shibai, H., Ootsubo, T., & Tamura, M. 2007, ApJ, 662, 1282

Mayama, S., Hashimoto, J., Muto, T., et al. 2012, ApJL, 760, L26

Meheut, H., Keppens, R., Casse, F., & Benz, W. 2012, A&A, 542, 9

Meheut, H., Yu, C., & Lai, D. 2012, MNRS, 422, 2399

Menten, K. M., Reid, M. J., Forbrich, J., & Brunthaler, A. 2007, A&A, 474, 515

Min, M., Dullemond, C., Kama, M., & Dominik, C. 2011, Icarus, 212, 416

Miyake, K., & Nakagawa, Y. 1993, Icarus, 106, 20

Mizuno, H., Markiewicz, W. J., & Voelk, H. J. 1988, A&A, 195, 183

Morrow, A. L., Luhman, K. L., Espaillat, C., et al. 2008, ApJL, 676, L143

Muench, A. A., Alves, J., Lada, C. J., & Lada, E. A. 2001, ApJ, 558, L51

Mulders, G. D., Dominik, C., & Min, M. 2010,A&A, 512, A11

Mulders, G. D., & Dominik, C. 2012,A&A, 539, A9

Muto, T., Grady, C. a., Hashimoto, J., et al. 2012, ApJ, 748, L22

Muzerolle, J., Flaherty, K., Balog, Z., et al. 2009, ApJL, 704, L15

Muzerolle, J., Allen, L. E., Megeath, S. T., Hernández, J., & Gutermuth, R. A. 2010, ApJ, 708, 1107

Nakagawa, Y., Nakazawa, K., & Hayashi, C. 1981, Icarus, 45, 517

Nakagawa, Y., Sekiya, M., & Hayashi, C. 1986, Icarus, 67, 375

Nakajima, T., Oppenheimer, B. R., Kulkarni, S. R., et al. 1995, Nature, 378, 463

Nakamoto, T., & Nakagawa, Y. 1994, ApJ, 421, 640

Natta, A., & Testi, L. 2004a, Star Formation in the Interstellar Medium: In Honor of David Hollenbach, 323, 279

Natta, A., Testi, L., Neri, R., Shepherd, D. S., & Wilner, D. J. 2004,A&A, 416, 179

Natta, A., Testi, L., Calvet, N., Henning, T., Waters, R., & Wilner, D. 2007, Protostars and Planets V, 767

O'dell, C. R., & Wen, Z. 1994, ApJ, 436, 194

Ogihara, M., Ida, S., & Morbidelli, A. 2007, Icarus, 188, 522

Okuzumi, S. 2009, ApJ, 698, 1122

Okuzumi, S., Tanaka, H., Takeuchi, T., & Sakagami, M.-a. 2011, ApJ, 731, 96

Okuzumi, S., Tanaka, H., Kobayashi, H., & Wada, K. 2012, ApJ, 752, 106

Olofsson, J., Benisty, M., Augereau, J.-C., et al. 2011,A&A, 528, L6

Oppenheimer, B. R., Brenner, D., Hinkley, S., et al. 2008, ApJ, 679, 1574

Ormel, C. W., & Cuzzi, J. N. 2007, A&A, 466, 413

Owen, J. E., Ercolano, B., & Clarke, C. J. 2011, MNRAS, 411, 1104

Paardekooper, S.-J., & Mellema, G. 2004, A&A, 425, L9

Paardekooper, S.-J. 2007, A&A, 462, 355

Papaloizou, J., & Lin, D. N. C. 1984, ApJ, 285, 818

Pascucci, I., Apai, D., Luhman, K., et al. 2009, ApJ, 696, 143

Pérez, L. M., Carpenter, J. M., Chandler, C. J., et al. 2012, ApJL, 760, L17

Piétu, V., Guilloteau, S., & Dutrey, A. 2005, A&A, 443, 945

Piétu, V., Dutrey, A., Guilloteau, S., Chapillon, E., & Pety, J. 2006,A&A, 460, L43

Pinilla, P., Birnstiel, T., Ricci, L., et al. 2012a,A&A, 538, A114

Pinilla, P., Benisty, M., & Birnstiel, T. 2012b,A&A, 545, A81

Pinte, C., Menard, F., Duchene, G., & Bastien, P. 2006, A&A, 459, 797

Pollack, J. B., Hubickyj, O., Bodenheimer, P., et al. 1996, Icarus, 124, 62

Pott, J.-U., Perrin, M. D., Furlan, E., et al. 2010, ApJ, 710, 265

Pringle, J. E. 1981, AR&A, 19, 137

Rameau, J., Chauvin, G., a. M. Lagrange, et al. 2012, A&A, 546, A24

Rebolo, R., Zapatero Osorio, M. R., & Martín, E. L. 1995, Nature, 377, 129

Regály, Z., Juhász, A., Sándor, Z., & Dullemond, C. P. 2012, MNRAS, 419, 1701

Riaz, B., Lodieu, N., & Gizis, J. E. 2009, ApJ, 705, 1173

Riaz, B., Honda, M., Campins, H., et al. 2012, MNRAS, 420, 2603

Ricci, L., Testi, L., Natta, A., Neri, R., Cabrit, S., & Herczeg, G. J. 2010a, A&A, 512, A15

Ricci, L., Testi, L., Natta, A., & Brooks, K. J. 2010b, A&A, 521, A66

Ricci, L., Mann, R. K., Testi, L., Williams, J. P., Isella, A., Robberto, M., Natta, A., & Brooks, K. J. 2011, A&A, 525, A81

Ricci, L., Testi, L., Natta, A., Scholz, A. & de Gregorio-Monsalvo, I., ApJ, 761, L20.

Ricci, L., Isella, A., Carpenter, J. M., & Testi, L. 2013, ApJL, 764, L27

Rice, W. K. M., Armitage, P. J., Wood, K., & Lodato, G. 2006, MNRAS, 373, 1619

Rodmann, J., Henning, T., Chandler, C. J., Mundy, L. G., & Wilner, D. J. 2006, A&A, 446, 211

Rosotti, G. P., Ercolano, B., Owen, J. E., & Armitage, P. J. 2013, MNRAS, 430, 1392

Safronov, V. S., & Zvjagina, E. V. 1969, Icarus, 10, 109

Sándor, Z., Lyra, W., & Dullemond, C. P. 2011, ApJL, 728, L9

Schäfer, C., Speith, R., & Kley, W. 2007, A&A, 470, 733

Scholz, A., Jayawardhana, R., & Wood, K. 2006, ApJ, 645, 1498

Scholz, A., Jayawardhana, R., Wood, K., et al. 2007, ApJ, 660, 1517

Strom, K. M., Strom, S. E., Edwards, S., Cabrit, S., & Skrutskie, M. F. 1989, AJ, 97, 1451

Semenov, D., Henning, T., Helling, C., Ilgner, M., & Sedlmayr, E. 2003, A&A, 410, 611

Schegerer, A. A., & Wolf, S. 2010, A&A, 517, A87

Shakura, N. I., & Sunyaev, R. A. 1973,A&A, 24, 337

Shu, F. H., Adams, F. C., & Lizano, S. 1987, ARA&A, 25, 23

Sicilia-Aguilar, A., Henning, T., & Hartmann, L. W. 2010, Apj, 710, 597

Simon, J. B., Bai, X.-N., Stone, J. M., Armitage, P. J., & Beckwith, K. 2013, ApJ, 764, 66

Smoluchowski, M. V. 1916, Zeitschrift fur Physik, 17, 557

Strom, K. M., Strom, S. E., Edwards, S., Cabrit, S., & Skrutskie, M. F. 1989, AJ, 97, 1451

Szűcs, L., Apai, D., Pascucci, I., & Dullemond, C. P. 2010, ApJ, 720, 1668

Tanaka, H., Himeno, Y., & Ida, S. 2005, Apj, 625, 414

Terebey, S., Shu, F. H., & Cassen, P. 1984, ApJ, 286, 529

Testi, L., Natta, A., Shepherd, D. S., & Wilner, D. J. 2001, ApJ, 554, 1087

Testi, L., Natta, A., Shepherd, D. S., & Wilner, D. J. 2003, A&A, 403, 323

Toomre, A. 1964, ApJ, 139, 1217

Ubach, C., Maddison, S. T., Wright, C. M., et al. 2012, MNRAS, 425, 3137

Uribe, A. L., Klahr, H., Flock, M., & Henning, T. 2011, ApJ, 736, 85

Varnière, P., & Tagger, M. 2006, A&A, 446, L13

Verhoeff, A. P., Min, M., Pantin, E., et al. 2011, A&A, 528, A91

Voelk, H. J., Jones, F. C., Morfill, G. E., & Roeser, S. 1980, A&A, 85, 316

Wada, K., Tanaka, H., Suyama, T., Kimura, H., & Yamamoto, T. 2009, ApJ, 702, 1490

Wada, K., Tanaka, H., Suyama, T., Kimura, H., & Yamamoto, T. 2011, ApJ, 737, 36

Weidenschilling, S. J. 1977, MNRAS, 180, 57

Whipple, F. L. 1972, From Plasma to Planet, 211

Wilking, B. A., Gagné, M., & Allen, L. E. 2008, Handbook of Star Forming Regions, Volume II, 351

Williams, J. P. & Cieza, L. A. 2011, ARA&A, 49, 67

Wilner, D. J., Ho, P. T. P., Kastner, J. H., & Rodríguez, L. F. 2000, ApJ, 534, L101

Wilner, D. J., D'Alessio, P., Calvet, N., Claussen, M. J., & Hartmann, L. 2005, ApJ, 626, L109

Windmark, F., Birnstiel, T., Ormel, C. W., & Dullemond, C. P. 2012b, A&A, 544, L16

Windmark, F., Birnstiel, T., Ormel, C. W., & Dullemond, C. P. 2012a, A&A, 544, L16

Woitke, P., Kamp, I., & Thi, W.-F. 2009, A&A, 501, 383

Wolf, S. & Klahr, H. 2002, ApJ, 578, L79

Yang, C.-C., & Menou, K. 2010, MNRAS, 402, 2436

Youdin, A. N., & Shu, F. H. 2002, ApJ, 580, 494

Youdin, A. N. & Goodman, J. 2005, Apj, 620, 459

Youdin, A. N., & Lithwick, Y. 2007, Icarus, 192, 588

Young, R. E. 2003, New Astronomy Reviews, 47, 1

Zhu, Z., Nelson, R. P., Hartmann, L., Espaillat, C., & Calvet, N. 2011, Apj, 729, 47

Zhu, Z., Nelson, R. P., Dong, R., Espaillat, C., & Hartmann, L. 2012, ApJ, 755, 6

Zsom, A., & Dullemond, C. P. 2008, A&A, 489, 931

Zsom, A., Ormel, C. W., Güttler, C., Blum, J., & Dullemond, C. P. 2010, A&A, 513, A57

Zsom, A., Sándor, Z., & Dullemond, C. P. 2011, A&A, 527, A10

Acknowledgments

Since I was a child, one of my dreams has been to become an Astronomer. Many people have touched my life in different ways that allow this dream to be real today. Although the words are never enough, I want to express my sincere acknowledgments to most of them:

First of all, this thesis is dedicated to my parents who taught me to always follow my dreams with courage, patience and wisdom and to give the best of myself in all aspects. I am infinitely thankful for all their love. Thanks to my brother for all his support, specially because his last visit to Europe was an awesome opportunity to get to know better each other. I am also quite thankful with Andrés G., for all his support and because he did not allow me to give up my dreams; without his love and patience during the first two years of my Ph.D., this thesis would not be possible. I want to thanks to my uncle Arturo who with his great spirit has always been a good model in my life. Knowing that I count with my family no matter what, helps me to bravely keep walking in life.

Special thanks to my supervisor *Kees Dullemond*, no only for giving me the opportunity to do my Ph.D. with him, but also because all his support, collaboration and advices have helped me to develop myself as an Astronomer. To Myriam Benisty, because her special enthusiasm and knowledge always inspired me to do my best and her support was crucial during my Ph.D. Her friendship is at the same time one of the most invaluable treasures that I found in Heidelberg. To my collaborator and amazing colleague, Til Birnstiel, for being always willing to answer my questions and collaborate with me. To the members of the planet formation group, in particular to: Fredrik W., Joanna D., Laszlo S., Jon R., Volker G., Sareh A., Sebastian S. and Helen M., for the very fruitful discussions, help and nice conversations (sometimes with delicious cakes and cookies) during these years. To scientific collaborators from whom I have learned a lot: Luca Ricci, Antonella Natta, Leonardo Testi, Carsten Dominik, Attila Juhasz, Ewine van Dishoeck,

Nienke van der Marel and María de Juan Ovelar.

Many thanks to whom for the first time encouraged me to become a scientist, my high-school teacher Edilberto P., thanks also for this amazing friendship that grows everyday despite of the time-space distance that has always been between us. Also, thanks to: my beautiful best friend, who is like my sister: Liz María, I love to walk my life-path next to her. To Susana A., for being my friend and growing up with me for almost 20 years. To all my colombian friends around the world who are all the time in my heart, specially to: L. Aníbal G., Diego C., Nohora G., Carlos U., Pamela R., Juliana G., Edwin H...One of the best things about having studied Physics was to meet all these good people.

The three years in Heidelberg are unforgettable because of many sensational people, thanks to: AnaLu because her friendship was indispensable for starting my new life in Germany. To Camila & Julio for being my 'adoptive' family, specially when I felt home-sick. To Héctor for his particular wisdom and support. To Pamela, for showing me the magnificent beauty and peace of the Alps. To Ronald, for the crickets, airplanes, seashells, drinks together, but specially because his friendship gave me a lot of hope. To Somayeh for having always a charming smile for me. To Nataschita, for being my partner in so funny adventures. To Sarita for all her time listening me and for her advices. To Max, for all his positive energy. To my officemates and friends: Faviola and Gustavo, with all our complaints about life, we laughed a lot in hard working days. And finally, to the person who reminded me that I am very lucky in my life: Artur, with his love and company, my life in Heidelberg turned to be a fantasy! I am looking forward for living with him all the challenges that the future has for us.

And last but most important, **thanks God for all Your love**, for giving me such wonderful life and for being surrounded by so incredible people during my 27 years of life.